



# Quantifying Methane Emissions Using Satellite Observations

## Citation

Wecht, Kevin James. 2014. Quantifying Methane Emissions Using Satellite Observations. Doctoral dissertation, Harvard University.

## Permanent link

<http://nrs.harvard.edu/urn-3:HUL.InstRepos:11744460>

## Terms of Use

This article was downloaded from Harvard University's DASH repository, and is made available under the terms and conditions applicable to Other Posted Material, as set forth at <http://nrs.harvard.edu/urn-3:HUL.InstRepos:dash.current.terms-of-use#LAA>

## Share Your Story

The Harvard community has made this article openly available.  
Please share how this access benefits you. [Submit a story](#).

[Accessibility](#)

# **Quantifying Methane Emissions Using Satellite Observations**

A dissertation presented

by

Kevin James Wecht

to

The Department of Earth and Planetary Sciences

in partial fulfillment of the requirements

for the degree of

Doctor of Philosophy

in the subject of

Earth and Planetary Sciences

Harvard University

Cambridge, Massachusetts

December 2013

© 2013 Kevin James Wecht

All rights reserved.

## **Quantifying Methane Emissions Using Satellite Observations**

### **Abstract**

Methane is the second most influential anthropogenic greenhouse gas. There are large uncertainties in the magnitudes and trends of methane emissions from different source types and source regions. Satellite observations of methane offer dense spatial coverage unachievable by suborbital observations. This thesis evaluates the capabilities of using satellite observations of atmospheric methane to provide high-resolution constraints on continental scale methane emissions. In doing so, I seek to evaluate the supporting role of suborbital observations, to inform the emission inventories on which policy decisions are based, and to enable inverse modeling of the next generation of satellite observations.

Errors were characterized in the standard TES methane data product using observations from the HIPPO aircraft campaign. An observation system simulation experiment (OSSE) using synthetic TES-like observations showed that TES can constrain emissions on global to continental scales. An experimental TES methane data product containing two pieces of information in the vertical has smaller errors than the standard product, and is therefore of promising value for constraining methane emissions.

Methane emissions in the United States (US) are quantified during summer 2004 using observations from SCIAMACHY, which has dense spatial coverage and sensitivity throughout the troposphere. Aircraft data from the INTEx-A campaign serve to characterize errors in the SCIAMACHY data and to evaluate inversion results. An inversion at  $\sim 100 \times 100 \text{ km}^2$  horizontal resolution provides the optimal estimate of US



emissions. Optimized emissions are larger than estimated by the US Environmental Protection Agency (EPA), particularly from livestock sources.

Methane emissions from California are quantified using a dense set of aircraft observations from the CalNex campaign (May-June 2010) are found to be nearly a factor of two higher than estimated by the California Air Resources Board. Satellite observations from TES constrain free tropospheric background methane while GOSAT observations identify the spatial pattern of error observed by CalNex but are too sparse to quantify statewide emissions. OSSEs show that the future TROPOMI satellite instrument may constrain California emissions at a detail comparable to the CalNex observations. Geostationary observations offer even greater for constraining future emissions.

## Table of Contents

Abstract	iii
Table of contents	v
List of Figures	viii
List of Tables	x
Acknowledgements	xi

## Chapter 1: Overview

1.1	Methane emissions and their uncertainties	1
1.2	Satellite observations of methane	2
1.3	Research objectives and approach	3
1.4	Summary of results	4
	References	6

## Chapter 2: Validation of TES methane with HIPPO aircraft observations: implications for inverse modeling of methane sources

	Abstract	9
2.1	Introduction	10
2.2	Data	13
	2.2.1 TES	13
	2.2.1 HIPPO and application of the TES operator	15
2.3	TES Validation	17
	2.3.1 Approach	17
	2.3.2 V004 Validation	19

2.3.3	V005 Validation	22
2.4	Utility of TES V004 data for inverse modeling of methane sources	25
	References	30

### **Chapter 3: Mapping of North American methane emissions with high spatial resolution by inversion of SCIAMACHY satellite data**

	Abstract	35
3.1	Introduction	36
3.2	Observations	39
3.3	Optimization of methane emissions	43
3.3.1	GEOS-Chem model and a priori emissions	43
3.3.2	Inversion Method	47
3.3.3	Clustering	51
3.3.4	Evaluation with SCIAMACHY and INTEx-A data	55
3.4	Optimized methane emissions	57
3.5	Comparison to previous studies	59
3.6	Conclusions	62
	References	66

### **Chapter 4: Spatially resolving methane emissions in California: constraints from the CalNex aircraft campaign and from present (GOSAT, TES) and future (TROPOMI, geostationary) satellite observations**

	Abstract	73
4.1	Introduction	74
4.2	GEOS-Chem inverse modeling system for methane emissions	77
4.2.1	Forward model and optimization procedure	78

4.2.2	A priori emissions for the inversion	80
4.3	Inversion of CalNex observations	82
4.3.1	Observations and error characterization	82
4.3.2	Inversion Results	86
4.3.3	Attribution to source types	88
4.4	Utility of current satellites (GOSAT, TES) for constraining California emissions	91
4.5	Potential of future satellites (TROPOMI, geostationary)	94
4.6	Conclusions	96
	References	100

## List of Figures

<b>Figure 2.1:</b> Typical averaging kernel matrices for TES methane retrievals over the tropical ocean: V004 (left) and V005 (right)	14
<b>Figure 2.2:</b> Flight paths of HIPPO missions I and II during January and October–November 2009 respectively (left). Center and right panels show methane concentrations as a function of latitude and pressure measured during southbound and northbound flight paths of HIPPO I and II	16
<b>Figure 2.3:</b> Error statistics for TES V004 methane plotted as a function of the size of the coincidence window for the HIPPO I and II vertical profiles	18
<b>Figure 2.4:</b> Latitudinal profile of the difference $\Delta y_R$ between TES V004 and HIPPO methane concentrations (RTVMRs) during HIPPO I & II in January and October–November 2009	19
<b>Figure 2.5:</b> Vertical profiles of V004 (top) and V005 (bottom) observed and theoretical relative errors	21
<b>Figure 2.6:</b> Latitudinal profiles of the differences $\Delta y$ between TES V005 and HIPPO methane concentrations during HIPPO I and II	23-24
<b>Figure 2.7:</b> Methane emissions [Mg per grid square per month] in the GEOS-Chem CTM for July–August 2008 at $4^\circ \times 5^\circ$ horizontal resolution	26
<b>Figure 2.8:</b> Relative (left) and absolute (right) error of a priori (top) and optimized (bottom) methane emissions	27
<b>Figure 2.9:</b> Scatterplot of optimized vs. “true” methane emissions for individual $4^\circ \times 5^\circ$ grid squares	29
<b>Figure 3.1:</b> Methane over North America during the INTEx-A aircraft campaign (1 July – 14 August 2004): SCIAMACHY mean column mixing ratios (left) and INTEx-A mixing ratios below 850 hPa (right)	41
<b>Figure 3.2:</b> Validation of the SCIAMACHY IMAP v5.5 retrieval of methane column mixing ratio ( $X_{CH_4}$ ) with coincident INTEx-A aircraft vertical profiles	42
<b>Figure 3.3:</b> North American methane emissions used as a priori for the inversion: total emissions (top left panel) and contributions from the major source types	45
<b>Figure 3.4:</b> Methane concentrations in surface air averaged over the inversion period (22 June – 14 August 2004). The GEOS-Chem simulation with a priori sources (background) is compared to NOAA GMD observations (circles)	47

<b>Figure 3.5:</b> Emission scale factors relative to the a priori (top left panel of Figure 3) from inversions optimizing emissions on the $1/2^\circ \times 2/3^\circ$ native resolution of GEOS-Chem (left) and for 1000 clustered regions (right)	51
<b>Figure 3.6:</b> Sensitivity of inversion results to the resolution with which North American methane emissions are optimized from the SCIAMACHY data for 1 July – 14 August 2004	54
<b>Figure 3.7:</b> Optimized North American methane emissions from the 1000-cluster inversion	56
<b>Figure 3.8:</b> Independent evaluation of the SCIAMACHY inversion of methane emissions using INTEx-A aircraft data	57
<b>Figure 4.1:</b> EDGAR v4.2 methane emissions used as a priori for our inversion. Panels show total emissions and contributions from the three major source types	83
<b>Figure 4.2:</b> Mean methane concentrations below 2 km altitude from CalNex aircraft observations (left) and GEOS-Chem simulation (center). Left panel shows optimized correction factors from the inversion	84
<b>Figure 4.3:</b> Optimized methane emissions from our inversion using CalNex observations	87
<b>Figure 4.4:</b> Degrees of freedom in each grid square from our inversions using CalNex (top, left) and GOSAT (top, right) observations and from our OSSEs using TROPOMI (bottom, left) and geostationary (bottom, right) synthetic observations	89
<b>Figure 4.5:</b> Mean methane mixing ratios measured by GOSAT (left) and TES (center) for the CalNex period of 1 May – 22 June 2010, and optimized correction factors (right) to the a priori EDGAR v4.2 methane emissions from the GOSAT inversion	93

## List of Tables

<b>Table 2.1:</b> TES V004 and V005 methane validation statistics	18
<b>Table 3.1:</b> US anthropogenic sources of methane in 2004 [ $\text{Tg a}^{-1}$ ]	46
<b>Table 4.1:</b> Satellite observations of methane	76
<b>Table 4.2:</b> Methane emissions in California	81

## Acknowledgements

I am grateful to my dissertation advisor, Daniel Jacob, for the opportunity to pursue this research and for his guidance during the past six years. His enthusiasm for atmospheric chemistry inspired me to enter the field and continues to motivate my research. His breadth of knowledge and his acute scientific insight constantly challenge me to become a better scientist. I thank him for the years he has spent contributing to my education and strengthening this thesis.

Many other scientists have provided valuable assistance in enabling my research. I am particularly grateful to Daven Henze and Monika Kopacz, who patiently taught me about adjoint modeling, and to John Worden who introduced me to the science behind satellite observations. I am also thankful to Dylan Jones, Steve Wofsy, Eric Kort, Greg Santoni, and Vivienne Payne for their insight and expertise. Outside of the atmospheric chemistry community, conversations with Eli Tziperman, Zhiming Kuang, and Mauricio Santillana have helped to clarify my personal and scientific goals.

I am truly fortunate to have pursued my Ph.D. in the Atmospheric Chemistry Modeling Group. The group is a remarkable collection of intelligent and kind scientists who maintain a collaborative environment that makes research highly enjoyable. Special thanks go to my office mates Bess Sturges-Corbitt, Lee Murray, Chris Miller, Eloïse Marais, Katie Travis, and Hannah Horowitz. Thanks also go to past and present group members including: Peter Zoogman, Easan Drury, Justin Parella, Claire Carouge, Chris Holmes, Eric Leibensperger, Brenda Mathieu, Bob Yantosca, Melissa Sulprizio, Patrick Kim, Helen Amos, Shannon Koplitz, and Alex Turner.

I am indebted to the Harvard University Department of Earth and Planetary Sciences for being my home away from home for the past 10 years. Within its walls, I have nurtured my scientific curiosity and forged lasting friendships. For encouraging such a generous and vibrant community, I thank all the professors, staff, and students, especially Chenoweth Moffat, Sarah Colgan, and Maryorie Grande.

I am grateful to the GEOS-Chem, GEOS-Chem adjoint, TES, and HIPPO science teams for their time and assistance. Thanks also to the NASA Earth and Space Science Fellowship for funding my research.

Thank you to my friends and family who have provided love and support throughout these six years. Thank you to my roommates Jason Munster, David Toniatti, Rita Parai, and Phoebe Robinson. Thank you to Mom, Dad, and Emily for your endless encouragement and belief. Finally, thank you to Eileen; you have been there for me at every turn.



## Chapter 1. Overview

Methane is the second most powerful anthropogenic greenhouse gas after carbon dioxide (Myhre et al. 2013). Present day methane concentrations are  $\sim 2.5$  times higher than those of the pre-industrial atmosphere (Etheridge et al., 1998). The magnitude of global methane emissions is constrained within  $\pm 15\%$  by knowledge of the dominant global sink, chemical reaction with the OH radical. However, the magnitudes and trends of emissions from different source types and source regions are far more uncertain (Myhre et al. 2013, Hartmann et al. 2013). Satellite observations of atmospheric methane offer dense spatial coverage, and through inverse modeling, provide a powerful means of reducing these uncertainties.

### 1.1 Methane emissions and their uncertainties

Present day methane emissions are estimated to be  $\sim 550 \text{ Tg a}^{-1}$ , 50-65% of which are anthropogenic (Ciais et al. 2013). Major anthropogenic sources include natural gas and petroleum extraction, natural gas distribution, coal mining, landfills, livestock, rice cultivation, wastewater, and biofuel use. Wetlands are the largest natural source, followed by open fires, termites, and geological sources. Methane has an atmospheric lifetime of  $9.1 \pm 0.9$  years (Prather et al. 2012). Reaction with OH accounts for 90% of methane loss, with minor contributions from oxidation in the stratosphere, soil absorption, and reaction with tropospheric chlorine.

Global total emissions are constrained within  $\pm 15\%$  by knowledge of OH concentrations, derived from observations of methyl chloroform (Prinn et al. 2005, Montzka et al. 2011). The magnitudes of emissions from different source types and

source regions are far more uncertain. Reducing methane emissions has been identified as a low-cost priority in greenhouse gas emissions reduction strategies (IEA World Energy Outlook 2013, van Vuuren et al. 2006, Weyant et al. 2006). Efficacious emission reduction policies require better quantification of emissions on scales relevant to regulatory agencies (national, state).

## **1.2 Satellite observations of methane**

Satellite observations of atmospheric methane provide a resource for constraining emissions through inverse modeling, as first demonstrated by Bergamaschi et al. (2007). Satellites deliver dense spatial and temporal coverage unachievable by surface networks or aircraft campaigns. Methane has been retrieved from nadir satellite measurements of solar backscatter in the short-wave infrared (SWIR) and terrestrial radiation in the thermal infrared (TIR). SWIR retrievals are available from SCIAMACHY (2003-2012; Frankenberg et al. 2011) and GOSAT (2009-present; Parker et al. 2011; Schepers et al. 2012). TIR retrievals are available from AIRS (2002-present; Xiong et al., 2008), TES (2004-2011; Worden et al. 2012), and IASI (2007-present; Xiong et al. 2013; Crevoisier et al. 2013). SWIR retrievals provide total atmospheric columns. TIR retrievals provide vertical profiles but with low sensitivity to the lower troposphere due to lack of thermal contrast, and this limits their value for detecting regional sources (Wecht et al., 2012). The TROPOMI instrument to be launched in 2015 will provide SWIR methane data with global daily coverage and  $7 \times 7 \text{ km}^2$  nadir resolution (Veefkind et al., 2012). There are also several current proposals for geostationary SWIR observation of methane over North America, drawing on plans for the NASA GEO-CAPE mission (Fishman et al., 2012).

### **1.3 Research objectives and approach**

This thesis evaluates the capabilities of using satellite observations of atmospheric methane to provide high-resolution constraints on continental scale methane emissions. In doing so, I seek to evaluate the supporting role of suborbital observations, to inform the emission inventories on which policy decisions are based, and to enable inverse modeling of the next generation of satellite observations.

To pursue the goals stated above, I perform inverse modeling using the GEOS-Chem chemical transport model (CTM) to relate methane emissions to satellite observations. The inverse modeling consists of minimizing a Bayesian cost function that weighs the constraints on emissions from the satellite observations against a priori estimates of emissions (Rodgers, 2000).

Minimization of the cost function is performed using the GEOS-Chem CTM, its adjoint, and a quasi-Newton optimization method. The GEOS-Chem adjoint was described by Henze et al. (2007) with application to CO by Kopacz et al. (2009). Application to methane follows that for CO but includes only methane chemistry and methane emissions. The computational cost of the adjoint method is only weakly sensitive to both the number of observations and to the number of geographical regions from which emissions are estimated. This enables the use of dense satellite observations to constrain methane emissions at a spatial scale limited only by the CTM. Throughout this thesis, suborbital observations from aircraft or surface stations are used to support inverse modeling through characterization of errors in satellite observations and evaluation of inversion results.

## 1.4 Summary of Results

Chapter 2 evaluates the utility of TES methane version 4 (V004) for constraining surface emissions globally. Errors in the TES methane product are characterized by comparison to aircraft vertical profiles over the Pacific Ocean from the HIAPER Pole-to-Pole Observation (HIPPO) program, described by Wofsy et al. (2012). An Observation System Simulation Experiment (OSSE) is then conducted as follows. Using GEOS-Chem, synthetic TES data with error characteristics equivalent to those of V004 are generated from a “true” distribution of methane emissions. A priori methane emissions are then perturbed, and the synthetic data are assimilated in the GEOS-Chem inverse modeling framework in an attempt to recover the “true” methane distribution. OSSE results show that V004 data can constrain emissions on global to continental scales. An experimental TES data product with two pieces of information in the vertical (V005) has less random error than V004, and may provide better constraints on surface emissions.

Chapter 3 quantifies methane emissions from the United States (US) using observations from SCIAMACHY during the summer of 2004. Data from the INTEx-A aircraft campaign over the eastern US are used to identify and correct a water vapor dependent bias in the SCIAMACHY data. An inversion is conducted at the native resolution of GEOS-Chem ( $\sim 50 \times 50 \text{ km}^2$ ). GEOS-Chem grid cells are then grouped using a hierarchical clustering algorithm to extract maximum information from the SCIAMACHY observations. An inversion for emissions from 1000 clustered grid squares ( $\sim 100 \times 100 \text{ km}^2$ ) provides a better fit to SCIAMACHY observations. Improvement in the inversion is evaluated using boundary layer INTEx-A observations.

Optimized US emissions are  $32.0 \pm 1.3 \text{ Tg a}^{-1}$ , compared to  $28.3 \text{ Tg a}^{-1}$  in EPA emission inventory (EPA, 2013). US livestock emissions are underestimated by 60% by the EPA and are twice the natural gas and oil emissions, in contrast to the EPA inventory, in which these two sources are of comparable magnitude.

Chapter 4 demonstrates the capabilities of aircraft, current satellites, and future satellites for constraining emissions from California. Inversion of observations from the CalNex aircraft campaign (May-June 2010) at the native resolution of GEOS-Chem yield total California methane emissions of  $2.86 \pm 0.21 \text{ Tg a}^{-1}$ , compared with  $1.51 \text{ Tg a}^{-1}$  in the California Air Resources Board (CARB) inventory used for state regulations of greenhouse gas emissions. Current satellite observations from GOSAT can constrain methane emissions in the Los Angeles Basin but are too sparse to constrain emissions quantitatively elsewhere. An OSSE for the future TROPOMI satellite instrument (launch 2015) shows that it can constrain California methane emissions at a detail comparable to the CalNex aircraft campaign. Geostationary satellite observations offer even greater potential for constraining methane emissions in the future.

## References

- Bergamaschi, P., Frankenberg, C., Meirink, J. F., Krol, M., Dentener, F., Wagner, T., Platt, U., Kaplan, J. O., Körner, S., Heimann, M., Dlugokencky, E. J. and Goede A.: Satellite cartography of atmospheric methane from SCIAMACHY on board ENVISAT: 2. Evaluation based on inverse model simulations, *J. Geophys. Res.*, 112, D02304, doi:10.1029/2006JD007268, 2007.
- Ciais, P., Sabine, C., Bala, G., Bopp, L., Brovkin, V., Canadell, J., Chhabra, A., DeFries, R., Galloway, J., Heimann, M., Jones, C., Le Quere, C., Myneni, R., Piao, S., Thornton, P., *Climate Change 2013: The Physical Science Basis. Working Group I Contribution to the IPCC Fifth Assessment Report (AR5), Final Draft, chap. Carbon and Other Biogeochemical Cycles*, , <http://www.ipcc.ch/report/aar5/wg1/>, 2013.
- Crevoisier, C., Nobileau, D., Armante, R., Crépeau, L., Machida, T., Sawa, Y., Matsueda, H., Schuck, T., Thonat, T., Pernin, J., Scott, N. A., and Chédin, A.: The 2007–2011 evolution of tropical methane in the mid-troposphere as seen from space by MetOp-A/IASI, *Atmos. Chem. Phys.*, 13, 4279–4289, doi:10.5194/acp-13-4279-2013, 2013.
- Etheridge, D., Steele, L., Francey, R. and Langenfelds, R.: Atmospheric methane between 1000 AD and present: Evidence of anthropogenic emissions and climatic variability, *J Geophys Res-Atmos*, 103(D13), 15979–15993, 1998.
- Fishman, J., Iraci, L.T., Al-Saadi, J., Chance, K., Chavez, F., Chin, M., Coble, P., Davis, C., DiGiacomo, P.M., Edwards, D., Eldering, A., Goes, J., Herman, J., Hu, C., Jacob, D.J., Jordan, C., Kawa, S.R., Key, R., Liu, X., Lohrenz, S., Mannino, A., Natraj, V., Neil, D., Neu, J., Newchurch, M., Pickering, K., Salisbury, J., Sosik, H., Subramaniam, A., Tzortziou, M., Wang, J., and Wang, M., The United States' next generation of atmospheric composition and coastal ecosystem measurements: NASA's geostationary coastal and air pollution events (GEO-CAPE) mission. *Bulletin of the American Meteorological Society* 93, 1547-1566.
- Frankenberg, C., Aben, I., Bergamaschi, P., Dlugokencky, E. J., van Hees, R., Houweling, S., van der Meer, P., Snel, R. and Tol, P.: Global column-averaged methane mixing ratios from 2003 to 2009 as derived from SCIAMACHY: Trends and variability, *J. Geophys. Res.*, 116, D02304, doi:10.1029/2010JD014849, 2011.
- Hartmann, D.L., Klein Tank, A.M.G., Rusticucci, M., Alexander, L., Broennimann, S., Charabi, Y.A.-R., Dentener, F., Dlugokencky, E., Easterling, D., Kaplan, A., Soden, B., Thorne, P., Wild, M., and Zhai, P., *Climate Change 2013: The Physical Science Basis, Working Group I Contribution to the IPCC Fifth Assessment Report (AR5), Final Draft, chap. Observations: Atmosphere and Surface*, <http://www.ipcc.ch/report/aar5/wg1/>, 2013.
- Henze, D. K., Hakami, A., and Seinfeld, J. H.: Development of the adjoint of GEOS-Chem, *Atmos Chem Phys*, 7, 2413-2433, 2007.
- Kopacz, M., Jacob, D. J., Henze, D. K., Heald, C. L., Streets, D. G., Zhang, Q.: Comparison of adjoint and analytical Bayesian inversion methods for constraining Asian

sources of carbon monoxide using satellite (MOPITT) measurements of CO columns, . Geophys. Res., 114, D04305, doi:10.1029/2007JD009264, 2009.

Montzka, S.A., Krol, M., Dlugokencky, E., Hall, B., Jockel, P., and Lelieveld, J., Small interannual variability of global atmospheric hydroxyl, Science, 331, 67, doi:10.1126/science.1197640, 2011.

Myhre, G., Shindell, D., Breon, F.-M., Collins, B., Fuglestad, J., Huang, J., Koch, D., Lamarque, J.-F., Lee, D., Mendoza, B., Nakajima, T., Robock, A., Stephens, Graeme, Takemura, T., and Zhang, H., Climate Change 2013: The Physical Science Basis. Working Group I Contribution to the IPCC Fifth Assessment Report (AR5), Final Draft, chap. Anthropogenic and Natural Radiative Forcing, <http://www.ipcc.ch/report/ar5/wg1/>, 2013.

Parker, R., Boesch, H., Cogan, A., Fraser, A., Feng, L., Palmer, P. I., Messerschmidt, J., Deutscher, N., Griffith, D. W., Notholt, J., Wennberg, P. O., and Wunch, D.: Methane observations from the Greenhouse Gases Observing SATellite: Comparison to ground-based TCCON data and model calculations, Geophys. Res. Lett., 38, L15807, doi:10.1029/2011GL047871, 2011.

Prather, M. J., Holmes, C. D., and Hsu, J.: Reactive greenhouse gas scenarios: Systematic exploration of uncertainties and the role of atmospheric chemistry, Geophys. Res. Lett., 39, L09803, doi:10.1029/2012GL051440, 2012.

Prinn, R.G., Huang, J., Weiss, R.F., Cunnold, D.M., Fraser, P.J., Simmonds, P.G., McCulloch, A., Harth, C., Reimann, S., Salameh, P., O'Doherty, S., Wang, R.H.J., Porter, L.W., Miller, B.R., and Krummel, P.B., Evidence for variability of atmospheric hydroxyl radicals over the past quarter century, Geophys. Res. Lett., 32, L07809, doi:10.1029/2004GL022228, 2005.

Rodgers, C.D.: Inverse Methods for Atmospheric Sounding, World Scientific Publishing Co. Pte. Ltd, Tokyo 2000.

Schepers, D., Guerlet, S., Butz, A., Landgraf, J., Frankenberg, C., Hasekamp, O., Blavier, J.-F., Deutscher, N.M., Griffith, D.W.T., Hase, F., Kyro, E., Morino, I., Sherlock, V., Sussmann, R., and Aben, I., Methane retrievals from Greenhouse Gases Observing Satellite (GOSAT) shortwave infrared measurements: Performance comparison of proxy and physics retrieval algorithms, J. Geophys. Res., 117, D10307, doi:10.1029/2012JD017549, 2012.

van Vuuren, D.P., Stehfest, E., den Elzen, M.G.J., van Vliet, J., and Isaac, M., Exploring IMAGE model scenarios that keep greenhouse gas radiative forcing below 3 W/m<sup>2</sup> in 2100, Energy Economics 32, 1105-1120, 2010.

Veefkind, J.P., Aben, I., McMullan, K., Forster, H., de Vries, J., Otter, G., Claas, J., Eskes, H.J., de Haan, J.F., Kleipool, Q., van Weele, M., Hasekamp, O., Hoogeveen, R., Landgraf, J., Snel, R., Tol, P., Ingmann, P., Voors, R., Kruizinga, B., Vink, R., Visser, H., and Levelt, P.F., TROPOMI on the ESA Sentinel-5 Precursor: A GMES mission for

global observations of the atmospheric composition for climate, air quality and ozone layer applications, *Remote Sensing of Environment* 120, 70-83, 2012.

Wecht, K.J., Jacob, D.J., Wofsy, S.C., Kort, E.A., Worden, J.R., Kulawik, S.S., Henze, D.K., Kopacz, M., and Payne, V.H., Validation of TES methane with HIPPO aircraft observations: implications for inverse modeling of methane sources, *Atmos. Chem. Phys.*, 12, 1823–1832, 2012.

Weyant, J.P., de la Chesnaye, F.C., and Blanford, G.J., Overview of EMF-21: Multigas Mitigation Climate Policy, *The Energy Journal*, Multi-Greenhouse Gas Mitigation and Climate Policy Special Issue, 2006.

Wofsy, S. C., the HIPPO Science Team and Cooperating Modelers and Satellite Teams: HIAPER Pole-to-Pole Observations (HIPPO): fine-grained, global-scale measurements of climatically important atmospheric gases and aerosols, *Philosophical Transactions of the Royal Society A: Mathematical, Physical and Engineering Sciences*, 369(1943), 2073–2086, doi:10.1098/rsta.2010.0313, 2011.

Worden, J., Kulawik, S., Frankenberg, C., Bowman, K., Payne, V., Cady-Peirara, K., Wecht, K., Lee, J-E., Noone, D., Risi, C.: Profiles of CH<sub>4</sub>, HDO, H<sub>2</sub>O, and N<sub>2</sub>O with improved lower tropospheric vertical resolution from Aura TES radiances, *Atmos. Meas. Tech. Discuss.*, 4, 6679-6721, 2012.

World Energy Outlook, International Energy Agency, 2013.

Xiong, X., Barnet, C., Maddy, E., Sweeney, C., Liu, X., Zhou, L., and Goldberg, M.: Characterization and validation of methane products from the Atmospheric Infrared Sounder (AIRS), *J. Geophys. Res.*, 113, G00A01, doi:10.1029/2007JD000500, 2008.

Xiong, X., Barnet, C., Maddy, E.S., Gambacorta, A., King, T.S., and Wofsy, S.C., Mid-upper tropospheric methane retrieval from IASI and its validation, *Atmos. Meas. Tech.*, 6, 2255-2265, 2013.



## **Chapter 2. Validation of TES methane with HIPPO aircraft observations: implications for inverse modeling of methane sources**

[Wecht, K.J., Jacob, D.J., Wofsy, S.C., Kort, E.A., Worden, J.R., Kulawik, S.S., Henze, D.K., Kopacz, M., and Payne, V.H., 2012. Validation of TES methane with HIPPO aircraft observations: implications for inverse modeling of methane sources. *Atmospheric Chemistry and Physics*, 12, 1823-1832. Copyright 2012 Atmospheric Chemistry and Physics]

### **Abstract**

We validate satellite methane observations from the Tropospheric Emission Spectrometer (TES) with 151 aircraft vertical profiles over the Pacific from the HIAPER Pole-to-Pole Observation (HIPPO) program. We find that a collocation window of  $\pm 750$  km and  $\pm 24$  h does not introduce significant error in comparing TES and aircraft profiles. We validate both the TES standard product (V004) and an experimental product with two pieces of information in the vertical (V005). We determine a V004 mean bias of 65.8 ppb and random instrument error of 43.3 ppb. For V005 we determine a mean bias of 42.3 ppb and random instrument error of 26.5 ppb in the upper troposphere, and mean biases (random instrument errors) in the lower troposphere of 28.8 (28.7) and 16.9 (28.9) ppb at high and low latitudes respectively. Even when V005 cannot retrieve two pieces of information it still performs better than V004. An observation system simulation

experiment (OSSE) with the GEOS-Chem chemical transport model (CTM) and its adjoint shows that TES V004 has only limited value for constraining methane sources. Our successful validation of V005 encourages its production as a standard retrieval to replace V004.

## **2.1 Introduction**

Methane is the second most powerful anthropogenic greenhouse gas after carbon dioxide (Forster et al. 2007). Present day methane concentrations are  $\sim 2.5$  times higher than those of the pre-industrial atmosphere (Etheridge et al., 1998). This change is presumably driven by increasing emissions, but may also reflect changes in the chemical sink (reaction with the OH radical) (Forster et al. 2007). The magnitude of global methane emissions is constrained within  $\pm 15\%$  by knowledge of the global sink, but the magnitudes and trends of emissions from different source types and source regions are far more uncertain (Forster et al. 2007, Denman et al. 2007). Inverse modeling of atmospheric observations has emerged over the past decade as a powerful tool to reduce these uncertainties. Most inverse studies so far have relied on surface observations (Bergamaschi et al., 2005; 2010; Bousquet et al., 2006; Chen and Prinn, 2006; Fletcher et al., 2004; Hein et al., 1997; Houweling et al., 1999; Meirink et al., 2008b) but the sparsity of the network limits the ability to resolve sources (Villani et al., 2010). A few studies have used observations from the SCIAMACHY satellite instrument over land (Bergamaschi et al., 2007; 2009; Meirink et al., 2008a). Satellite observations of atmospheric methane provide dense spatial coverage but must be carefully validated to enable inverse modeling. We use here extensive vertical profiles of methane measured

from aircraft by the HIAPER Pole-to-Pole Observation (HIPPO) program over the Pacific (Wofsy et al., 2011) to characterize errors in methane retrievals from the Tropospheric Emission Spectrometer (TES) aboard the NASA Aura satellite. We show that the standard product currently available from TES is of limited utility for inverse modeling, but also validate a new TES product with increased vertical information and more promise.

Tropospheric methane is well-mixed, with a lifetime of about 9 years (Denman et al. 2007). Space-borne observations of column methane require precision of 1-2% and accuracy of at least 1% for inverse modeling of methane sources (Meirink et al., 2006). Methane can be retrieved from nadir measurements of solar backscatter in the near infrared (NIR) or terrestrial radiation in the thermal infrared (TIR). NIR retrievals are sensitive to the entire tropospheric column, but their dependence on reflected sunlight precludes observations at night, over most ocean surfaces, and over most cloudy targets. NIR retrievals are available from the Scanning Imaging Absorption SpectroMeter for Atmospheric CHartographY (SCIAMACHY) for 2003-2009 (Frankenberg et al., 2011) and from the Greenhouse gases Observing SATellite (GOSAT) for 2009-present (Yokota et al., 2009).

TIR methane retrievals have limited sensitivity to the lower troposphere due to lack of thermal contrast, but they can be performed day and night, over land and ocean, and for partly cloudy scenes. Uncertainties in atmospheric temperature, surface emissivity, and spectroscopic parameters of methane and interfering gases including water vapor,  $\text{N}_2\text{O}$ , and HDO limit the precision of TIR methane retrievals (Worden et al., 2004; Xiong et al., 2008). The Interferometric Monitor of Greenhouse gases (IMG)

aboard the ADEOS satellite was the first space-borne instrument used to retrieve tropospheric methane from the TIR (Clerbaux et al., 2003; Kobayashi et al., 1999). It was operational only from August 1996 to June 1997. The Atmospheric Infrared Sounder (AIRS) and the Infrared Atmospheric Sounding Interferometer (IASI) have provided TIR methane retrievals from 2002-present and 2007-present respectively (Crevoisier et al., 2009; Razavi et al., 2009; Xiong et al., 2008). The Tropospheric Emission Spectrometer (TES) aboard the Aura satellite was launched in July 2004 and remains operational, providing so far seven years of nearly continuous global methane retrievals. The current standard methane data product is version 4 (V004), but no validation has been published so far. A new TES methane product (V005) has recently been developed and is in the prototype stage (Worden et al., 2012). The V005 retrieval offers sensitivity lower in the atmosphere by expanding the spectral range used in the retrieval, thus increasing the value of TES methane for identifying methane sources.

Before satellite retrievals can be used for inverse modeling of methane sources, their systematic and random errors must be characterized. Previous validations of SCIAMACHY and GOSAT have used coincident observations from a limited number of ground based Fourier transform spectrometers (FTS), most of which are located in Europe and eastern North America (Dils et al., 2006; Morino et al., 2011; Sussmann et al., 2005). AIRS methane has been validated with NOAA/GMD aircraft profiles from 22 locations (Xiong et al., 2008), though mainly in a small latitudinal range over North America and not extending above 400 hPa. HIPPO provides a unique resource for satellite validation with near-continuous curtains of methane vertical profiles from near-surface to 330-180 hPa over a wide latitudinal range (67S – 85N).

## 2.2 Data

### 2.2.1 TES

TES is in a sun-synchronous polar orbit with an equator overpass local time of ~13:45. It makes nadir observations with a spatial resolution of 5.3 by 8.3 km<sup>2</sup>. Observations are made every 182 km along the orbit track. Successive orbit tracks are separated by about 22° longitude. The most recent publicly available TES methane product is V004 (available at <http://eosweb.larc.nasa.gov/>), using spectral windows of 1292.02 – 1305.76 cm<sup>-1</sup> (7.658 - 7.740 μm) and 1307.02 – 1307.8 cm<sup>-1</sup> (7.646 – 7.651 μm). Vertical methane profiles are retrieved using the Rodgers (2000) optimal estimation technique:

$$\ln \hat{\mathbf{z}} = \ln \mathbf{z}_a + \mathbf{A}(\ln \mathbf{z} - \ln \mathbf{z}_a) \quad (2.1)$$

where  $\hat{\mathbf{z}}$  is the retrieved vertical profile vector consisting of mixing ratios on a fixed pressure grid,  $\mathbf{A}$  is the averaging kernel matrix that represents the sensitivity of the retrieved profile to the true profile  $\mathbf{z}$ , and  $\mathbf{z}_a$  is the a priori specified from the MOZART chemical transport model (CTM). The retrieval method and error characterization are described by Bowman et al. (2006). A previous version of the methane retrieval (V003) is described by Payne et al. (2009).

Figure 2.1 (left panel) shows a typical TES V004 averaging kernel matrix in the tropics. The sensitivity peaks in the mid-upper troposphere at 200-400 hPa. The degrees of freedom for signal (DOFS) is defined as the trace of the averaging kernel matrix and estimates the number of pieces of information in the vertical profile. TES V004 methane

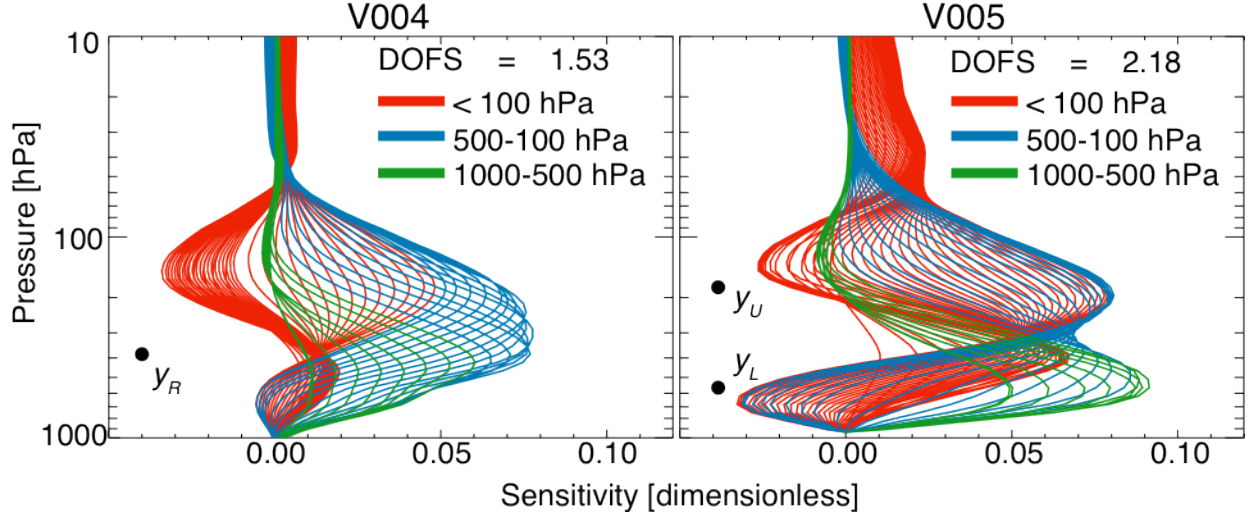


**Figure 2.1:** Typical averaging kernel matrices for TES methane retrievals over the tropical ocean: V004 (left) and V005 (right). Data are from the same target on 7 November 2009 at 1.1° S and 166.9° W. Lines are the individual rows of the averaging kernel matrix and represent the sensitivities of retrieved methane at given pressure levels to methane concentrations throughout the atmospheric column. Black circles indicate the pressure levels used for comparison to the HIPPO aircraft observations.

retrievals have 0.6-1.6 DOFS, highest over warm surfaces. In view of this limited resolution we reduce each TES vertical profile to a single representative tropospheric volume mixing ratio (RTVMR) as recommended by the TES Level 2 Data User's Guide ([http://tes.jpl.nasa.gov/uploadedfiles/TESDataUsersGuideV4\\_0.pdf](http://tes.jpl.nasa.gov/uploadedfiles/TESDataUsersGuideV4_0.pdf)) and described by Payne et al. (2009). The RTVMR is a tropospheric column average mixing ratio weighted by vertical sensitivity. The RTVMR approach maps the retrieved methane profile from the standard 67-level pressure grid to a four-level grid uniquely defined for each TES retrieval and consisting of points at 1) the Earth's surface, 2) the altitude of maximum sensitivity, 3) the tropopause, and 4) the top of the atmosphere:

$$\hat{\mathbf{z}}_c = \mathbf{M}^* \hat{\mathbf{z}} \quad (2.2)$$

Here  $\hat{\mathbf{z}}_c$  is the TES profile on the four-level RTVMR grid,  $\hat{\mathbf{z}}$  is the TES profile on the 67-level pressure grid, and  $\mathbf{M}^*$  is the triangular interpolation matrix that maps the fine grid

onto the coarse grid. Values of  $\hat{z}_c$  at the second lowest elevation define the RTVMR, termed  $y_R$ , and represent most of the TES information. The black circle in Figure 2.1 marks the pressure level associated with  $y_R$  for that particular profile.

V005 methane offers sensitivity lower in the atmosphere by expanding the spectral range of the retrieval (Worden et al., 2012), and lower systematic biases by normalizing the methane columns using simultaneously retrieved  $N_2O$  columns. For this study, V005 retrievals were performed on an experimental basis along the HIPPO I and II flight paths. Figure 2.1 (right panel) shows the V005 averaging kernel matrix from the same target as previously shown for V004. V005 DOFS are on average 0.5 greater than for V004. Vertical sensitivities for V005 targets with DOFS  $> 1.6$  have two tropospheric maxima in the upper and mid troposphere, near 200 and 550 hPa respectively. In order to capture these two pieces of vertical information, we modify the RTVMR approach for scenes with DOFS  $> 1.6$  by defining a five-level pressure grid onto which we map the 67-level TES retrieval. The five pressure levels are uniquely defined for each TES retrieval and are located at 1) the Earth's surface, 2) the lower tropospheric level of maximum sensitivity, 3) the upper tropospheric level of maximum sensitivity, 4) the tropopause, and 5) the top of the atmosphere. The second and third pressure levels define lower and upper tropospheric VMRs, termed  $y_L$  and  $y_U$  respectively. The black circles in Figure 2.1 mark the levels associated with  $y_L$  and  $y_U$ . For TES V005 scenes with DOFS  $\leq 1.6$ , we follow the original RTVMR approach and validate a single piece of information,  $y_R$ .

### 2.2.2 HIPPO and Application of the TES Operator

Figure 2.2 shows the flight paths of NSF's Gulfstream V (GV) during the first

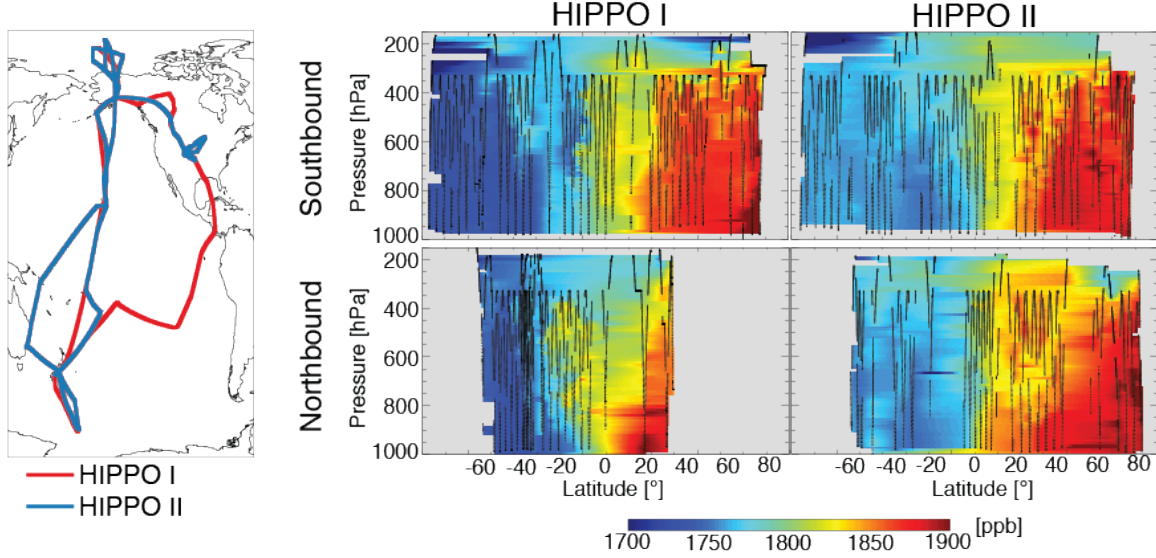


**Figure 2.2:** The left panel shows flight paths of HIPPO missions I and II during January and October–November 2009 respectively. Center and right panels show methane concentrations as a function of latitude and pressure measured during southbound and northbound flight paths of HIPPO I and II. Black lines show the aircraft profiles with methane data. Solid contours are interpolated.

two HIPPO missions in January and October–November 2009 (HIPPO I and II respectively). The GV transected the Pacific Ocean from 85N to 67S, performing in-progress vertical profiles every ~220 km or 20 minutes (Wofsy et al., 2011). Methane was measured with a Quantum Cascade Laser Spectrometer (QCLS) at 1 Hz frequency with accuracy of 1.0 ppb and precision of 0.5 ppb (Kort et al., 2011). HIPPO methane data are reported on the NOAA04 calibration scale. Latitudinal curtains of the data are shown in Figure 2.2. For direct comparison to TES methane we isolate each vertical profile performed by the GV, map the data on the 67 levels of the TES pressure grid, and extrapolate above the GV ceiling using the shape of the TES a priori profile. We then apply the TES observation operator to the resulting HIPPO profile,  $\mathbf{z}_H$ :

$$\ln \hat{\mathbf{z}}_H = \ln \mathbf{z}_a + \mathbf{A}(\ln \mathbf{z}_H - \ln \mathbf{z}_a) \quad (2.3)$$



Here  $\hat{\mathbf{z}}_{\text{H}}$  represents the profile that would have been retrieved had TES sampled the same air as HIPPO, according to the averaging kernel matrix and in the absence of other errors. We calculate  $y_R$ ,  $y_L$ , and  $y_U$  from  $\hat{\mathbf{z}}_{\text{H}}$  as described earlier.

## 2.3 TES Validation

### 2.3.1 Approach

TES and HIPPO profiles are not perfectly coincident in time and space. To compare the data sets, we must define an appropriate spatio-temporal coincidence window. Previous TES validation studies for tropospheric ozone with ozonesondes used coincidence criteria from  $\pm 9$  h to  $\pm 48$  h and 300 km to 600 km (Worden et al., 2007; Nassar et al., 2008). The high density of the HIPPO data allows an objective analysis of the collocation error and its effect on the validation constraints.

For each HIPPO vertical profile (covering  $\sim 220$  km in  $\sim 20$  minutes), we calculate a mean location and time. We then find all TES observations coincident with the HIPPO profile in a specified (space, time) coincidence window. Where a single TES observation is coincident with multiple HIPPO profiles, we match it to the nearest HIPPO profile in time and space, weighting time and space equally within the coincidence window. We calculate  $y_R$ ,  $y_L$ , and  $y_U$  from the TES and HIPPO profiles. From the statistics of the TES-HIPPO differences,  $\Delta y_R$ ,  $\Delta y_L$ , and  $\Delta y_U$ , we calculate a mean TES bias (mean value of  $\Delta y$ ) and residual standard deviation (standard deviation of  $\Delta y$ ).

Figure 2.3 shows the TES V004 mean bias and residual standard deviation as a function of the size of the coincidence window. If collocation error were significant, we

would expect the residual standard deviation to increase with the size of the coincidence window. This is not the case, implying that collocation error is not significant on scales up to 750 km and 24 h. This may reflect the lack of fine-scale variability in the HIPPO data (Figure 2.2) due to the remoteness from methane sources. We will use coincidence requirements of 750 km and 24 h in what follows, matching 151 HIPPO profiles to 398 V004 TES observations. Validation statistics are reported in Table 2.1 and discussed below.

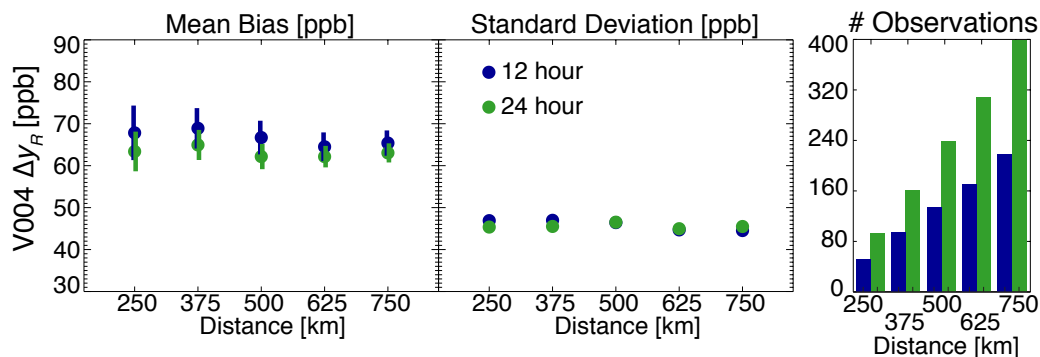


**Figure 2.3:** Error statistics for TES V004 methane plotted as a function of the size of the coincidence window for the HIPPO I and II vertical profiles. Green and blue symbols represent coincident time windows of  $\pm 24$  h and  $\pm 12$  h respectively. Values shown are the mean value (mean bias) and residual standard deviation of the difference  $\Delta y_R$  between TES and HIPPO representative tropospheric volume mixing ratios (RTVMRs). The numbers of observations in the statistics are shown in the right panel. Error bars in the left panel represent standard errors on our estimates of the mean bias.

**Table 2.1:** TES V004 and V005 Methane Validation Statistics<sup>a</sup>.

Observations	Mean Bias (ppb)	Residual standard deviation (ppb)	# TES
V004 $y_R$	69.5	43.0	396
V005 $y_L$	19.9	32.3	253
$y_U$	50.9	31.0	253
$y_R$	29.0	37.7	128

<sup>a</sup> Mean biases and residual standard deviations from TES-HIPPO difference statistics ( $\Delta y$ ). Units are ppb. For the V005 product and scenes when the degrees of freedom for signal (DOFS) exceeds 1.6, the validation is given for two pieces of information in the vertical,  $y_L$  (lower troposphere) and  $y_U$  (upper troposphere).

### 2.3.2 V004 Validation

Figure 2.4 shows the TES-HIPPO differences  $\Delta y_R$  as a function of latitude. We combine HIPPO I and II data because validation statistics are similar. We find a mean bias of 65.8 ppb (3.7 %) with a residual standard deviation of 43.8 ppb (2.4%). The residual standard deviation contains contributions from random instrument error in the TES retrievals and error induced by extrapolating above the observed HIPPO profiles. We estimate the extrapolation error from the variability in upper troposphere lower stratosphere (UTLS) methane concentrations observed during HIPPO, the Airborne

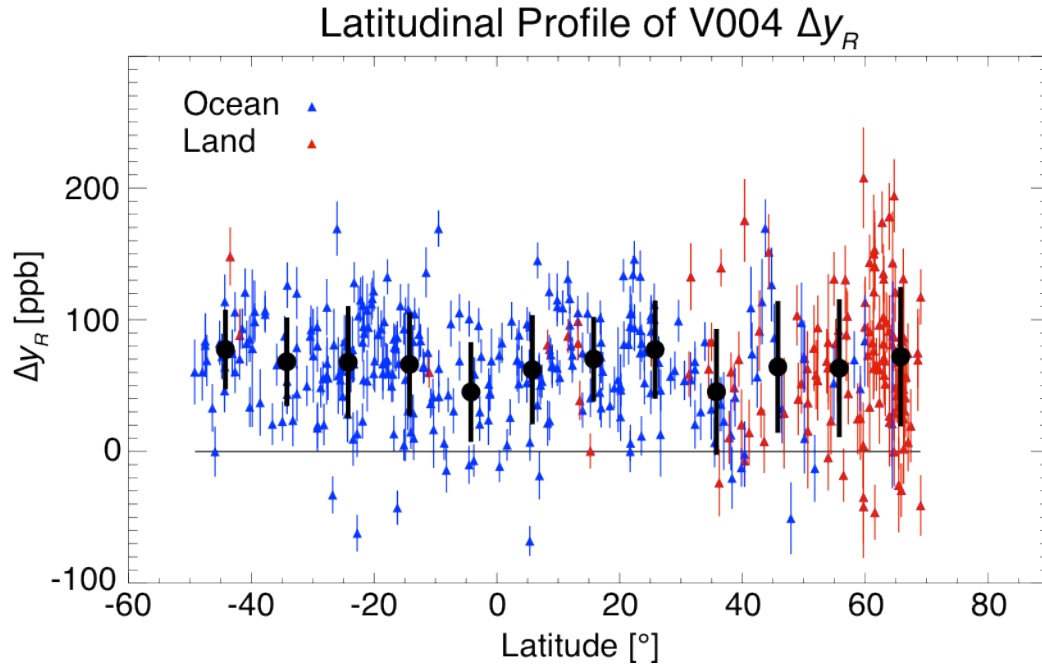


**Figure 2.4:** Latitudinal profile of the difference  $\Delta y_R$  between TES V004 and HIPPO methane concentrations (RTVMRs) during HIPPO I & II in January and October–November 2009. Symbols represent individual HIPPO vertical profiles, and associated vertical bars are the theoretical error standard deviations reported in the TES retrievals. Black circles and vertical bars are the means and standard deviations of  $y_R$  binned by 10° latitude.

Southern Hemisphere Ozone Experiment (ASHOE), the Stratospheric Tracers of Atmospheric Transport (STRAT), and the Photochemistry of Ozone Loss in the Arctic Region in Summer (POLARIS) (Elkins et al., 1996; Hurst et al., 1999). From these data sets we infer negligible error in extrapolation up to the local tropopause or 200 hPa, whichever is higher, and an error standard deviation of 6% above. Using local tropopause data from the GEOS-5 assimilation by the NASA Global Modeling and Assimilation Office (GMAO). We estimate an extrapolation error standard deviation of 6.7 ppb, Assuming that instrument and extrapolation errors add in quadrature, we conclude that the TES instrument error is 43.3 ppb (2.4 %).

This TES instrument error quantified by comparison with HIPPO observations is larger than the TES V004 theoretical error of 1.1%. Theoretical errors are the square roots of the diagonals of the TES self-reported error covariance matrices described by Boxe et al. (2010). Figure 2.5 shows the vertical structure of V004 theoretical and observed errors, the latter defined as the standard deviations of TES-HIPPO residual profiles ( $\hat{\mathbf{z}} - \hat{\mathbf{z}}_{\text{H}}$ ). Observed errors are consistently higher than theoretical errors.

There is no apparent trend in  $\Delta y_R$  bias as a function of latitude. An analysis of variance (ANOVA) fails to find statistically significant differences between the mean biases in 10-degree latitude bins (Figure 2.4), with a p-value of 0.80. The standard deviation of  $\Delta y_R$  increases north of 40° N. This trend is driven by larger  $\Delta y_R$  values over land (residual standard deviation of 52.0 ppb) than over ocean (39.6 ppb). The mean biases of land and ocean observations are 68.4 ppb (3.8 %) and 64.6 ppb (3.6 %), respectively. The biases are not statistically significantly different, with a two-sided p-value of 0.43.

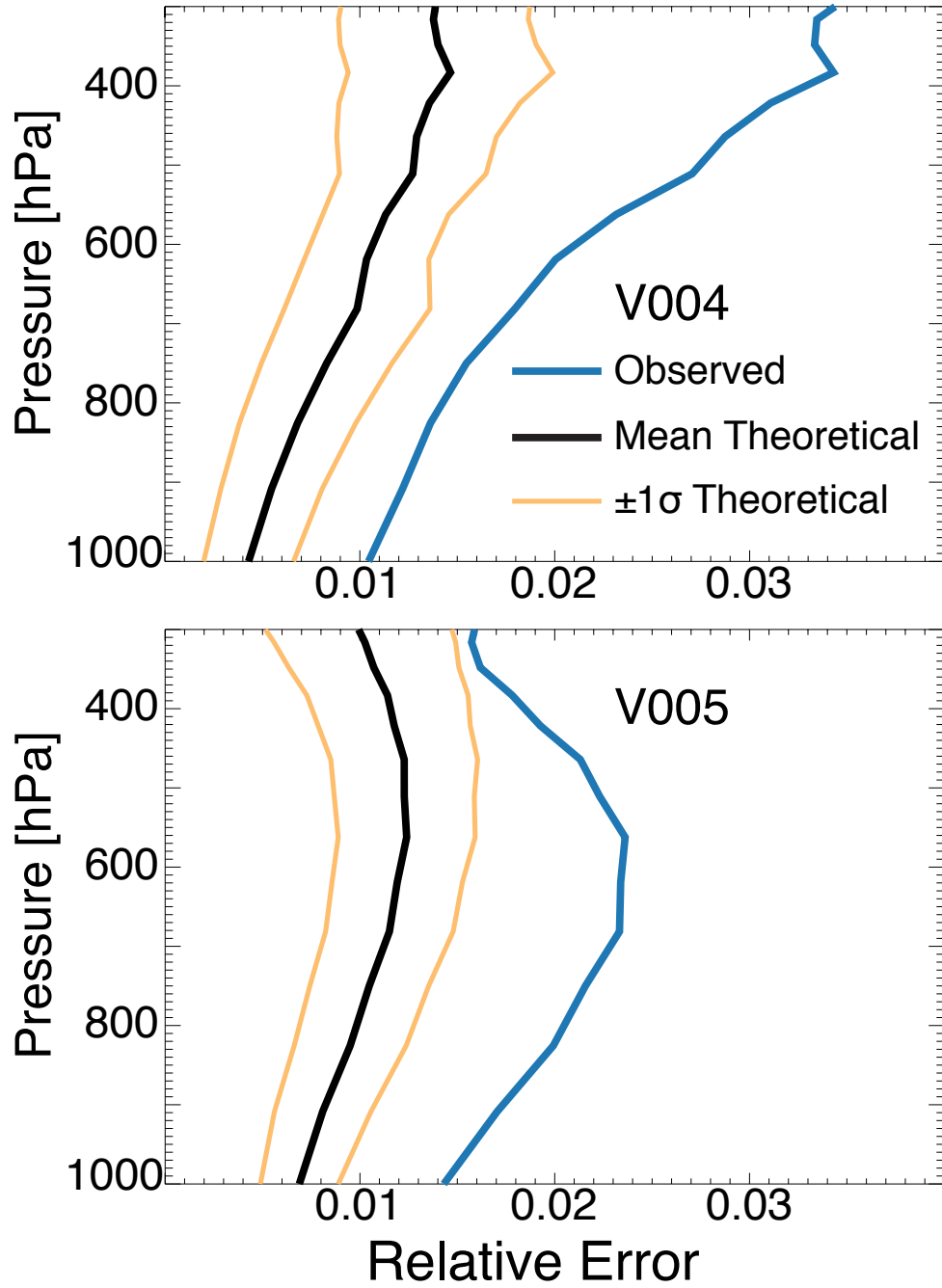


**Figure 2.5:** Vertical profiles of V004 (top) and V005 (bottom) observed and theoretical relative errors. Blue lines represent the relative standard deviation of  $\hat{\mathbf{z}} - \hat{\mathbf{z}}_{\text{H}}$ . Black and yellow lines represent the mean and standard deviation of the diagonals of the TES observation error covariance matrices.

### 2.3.3 V005 Validation

Figure 2.6 shows the latitudinal distribution of V005-HIPPO residuals for all observations within coincidence requirements determined previously ( $\pm 750$  km,  $\pm 24$  h). The bottom panel depicts  $\Delta y_R$  comparisons for scenes with  $\text{DOFS} \leq 1.6$ . These show V005  $y_R$  to be more accurate and precise than V004  $y_R$ , with a mean bias of 28.7 ppb (1.6 %) and residual standard deviation of 30.0 ppb (1.7 %). We subtract extrapolation error in the same way as before and calculate a V005  $\Delta y_R$  instrument error of 24.7 ppb (1.4 %). This error is larger than the V005 self-reported  $y_R$  error of 0.8%. There is no significant trend in error over the limited latitudinal range of the data.

Figure 2.6 top and middle panels show the latitudinal distributions of  $\Delta y_U$  and  $\Delta y_L$  for scenes with  $\text{DOFS} > 1.6$ . There is no significant trend in  $\Delta y_U$  bias or residual standard deviation as a function of latitude. We therefore calculate a single mean bias of 42.3 ppb (2.4 %) with a residual standard deviation of 30.9 ppb (1.7 %). Removing the extrapolation error implies a TES instrument error of 26.5 ppb (1.5 %). There is no significant trend in  $\Delta y_L$  residual standard deviation as a function of latitude, but an ANOVA reveals that  $\Delta y_L$  mean biases in 10-degree latitude bins are marginally significantly different, with a p-value of 0.06. We therefore report separate validation statistics for  $\Delta y_L$  at low latitudes (20°S - 20°N) and at high latitudes. Mean biases for low and high latitude  $\Delta y_L$  are 16.9 ppb (0.9 %) and 28.8 ppb (1.6 %), respectively. Residual standard deviations of low and high latitude  $\Delta y_L$  are 29.2 ppb (1.6 %) and 29.8 ppb (1.7 %), respectively. Removing extrapolation error implies low and high latitude  $\Delta y_L$  TES

**Figure 2.6:** Latitudinal profiles of the differences  $\Delta y$  between TES V005 and HIPPO methane concentrations during HIPPO I and II in January and October–November 2009. The top two panels show results for the lower and upper tropospheric TES data ( $\Delta y_L$  and  $\Delta y_U$ , respectively) in scenes where the degrees of freedom for signal (DOFS) exceeds 1.6. The bottom panel shows results for the RTVMR ( $\Delta y_R$ ) in scenes where the DOFS is lower than 1.6. Blue vertical bars are the theoretical error standard deviations reported in the TES retrievals. Black circles and vertical bars are the means and standard deviations binned by  $10^\circ$  latitude.

# Latitudinal Profiles of V005 $\Delta y_L$ , $\Delta y_U$ , $\Delta y_R$

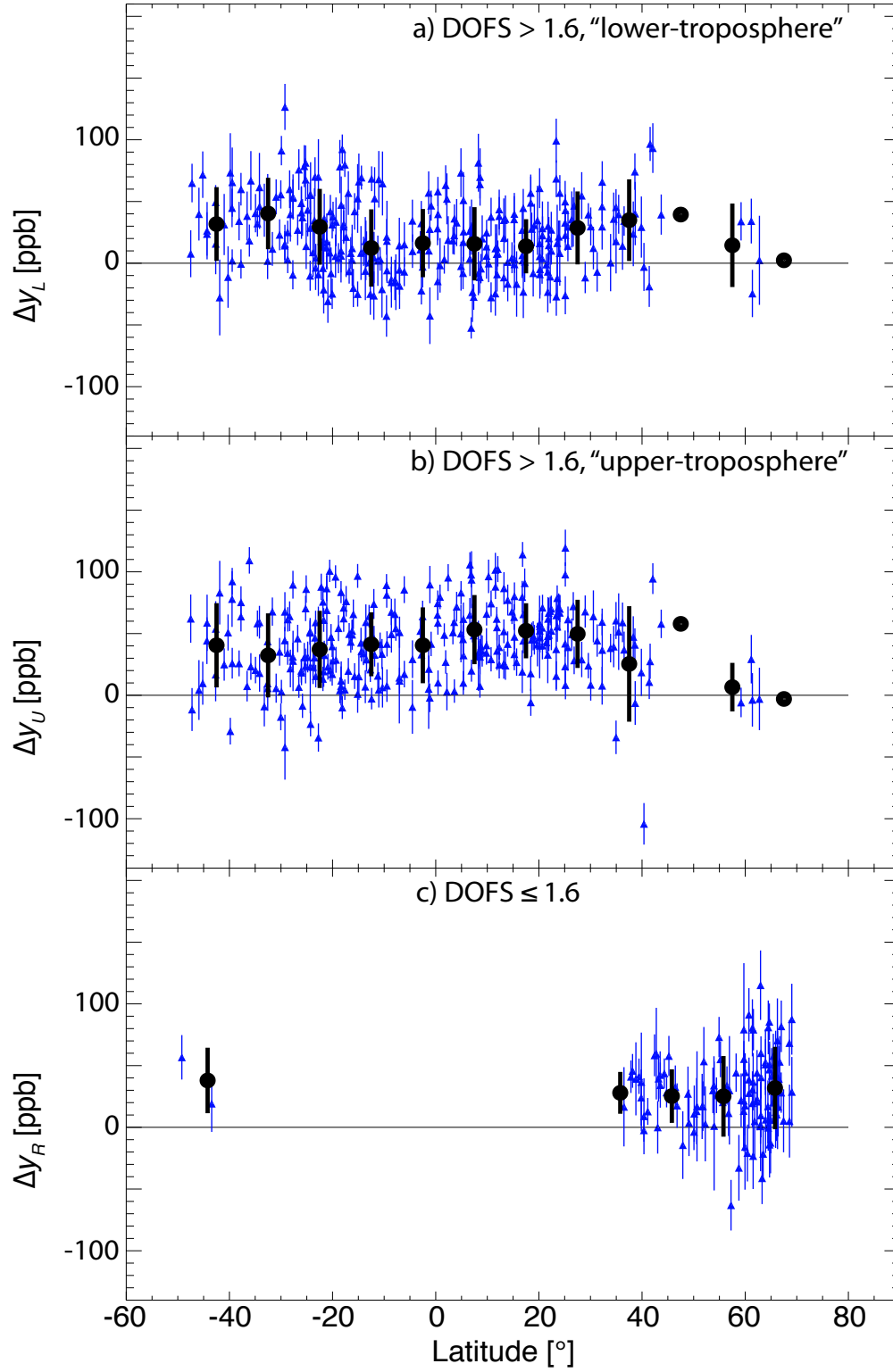


Figure 2.6 (Continued)



instrument errors of 28.9 ppb (1.6 %) and 28.7 ppb (1.6 %), respectively.

V005 observed errors are larger than self-reported errors for  $y_U$  and  $y_L$  of 1.0 % and 0.9 % respectively. Errors for individual retrievals are typically larger than the theoretical error, as indicated by the error bars in Figure 2.6. Figure 2.5 shows the vertical structure of V005 theoretical and empirical errors. Observed errors match the vertical shape of theoretical errors but are larger. This suggests that a uniform scaling of the observation error covariance matrix is needed for successful use of the V005 product for inverse modeling.

## **2.4 Utility of TES V004 Data for Inverse Modeling of Methane Sources**

We conduct here a simple observation system simulation experiment (OSSE) to evaluate the utility of the TES V004 standard methane product for constraining methane sources through inverse analysis. For this purpose we generate “true” atmospheric methane concentrations in the GEOS-Chem CTM (Pickett-Heaps et al., 2011) with  $4^\circ \times 5^\circ$  horizontal resolution using a “true” emission distribution as shown in Figure 2.7. We sample the “true” concentrations at the times and locations of TES observations, apply the TES observation operator, calculate  $y_R$ , and add random Gaussian noise with standard deviation of 40 ppb, as per our validation results in Table 2.1. We then perturb the “true” emission distribution to produce a deliberately incorrect a priori, and assimilate the synthetic observations to generate an “optimized” emissions estimate. Comparison of the “true” and “optimized” emissions provides a measure of the utility of TES for constraining methane emissions.

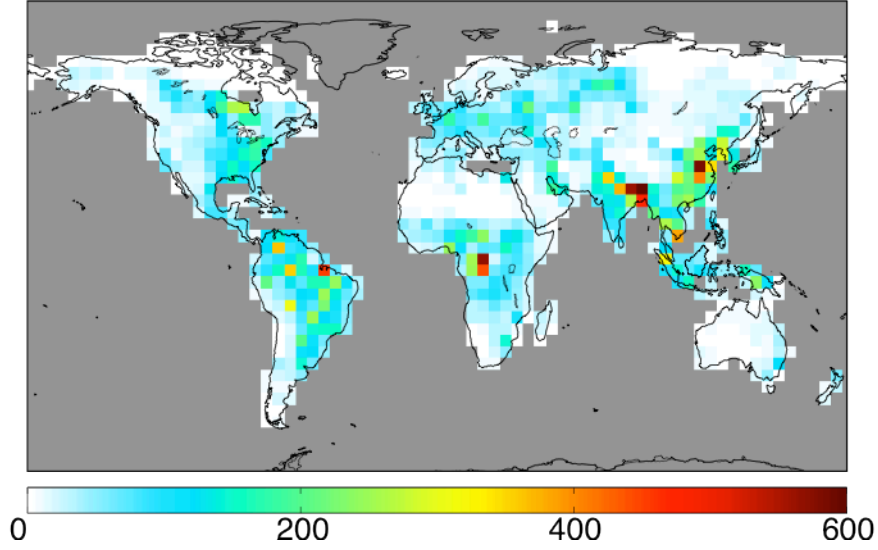


**Figure 2.7:** Methane emissions [Mg per grid square per month] in the GEOS-Chem CTM for July–August 2008 at  $4^\circ \times 5^\circ$  horizontal resolution. These are taken as the “true” emissions for the OSSE inversion of methane sources. Gray represents regions covered by ocean or ice.

We perform the OSSE for July–August 2008. There are 40,600 TES observations during this period. The ensemble of synthetic observations sampling the “true” atmosphere constitutes a vector  $\mathbf{y}_O$  of RTVMR values. The GEOS-Chem simulation with perturbed emissions generates a corresponding model vector  $\mathbf{y}_M$ . The “true” emissions on the  $4^\circ \times 5^\circ$  grid (land only) define a state vector  $\mathbf{x}$ . The perturbed emission values represent the a priori  $\mathbf{x}_a$  and are increased or decreased by 50% relative to  $\mathbf{x}$  in large blocks as depicted in figure 2.8. We perform Bayesian optimization by minimizing the least squares scalar cost function,  $J(\mathbf{x})$ :

$$J(\mathbf{x}) = (\mathbf{y}_M - \mathbf{y}_O)^T \mathbf{S}_e^{-1} (\mathbf{y}_M - \mathbf{y}_O) + (\mathbf{x} - \mathbf{x}_a)^T \mathbf{S}_a^{-1} (\mathbf{x} - \mathbf{x}_a) \quad (2.4)$$

Here  $\mathbf{S}_e$  and  $\mathbf{S}_a$  are the observational and a priori error covariance matrices, respectively.  $\mathbf{S}_e$  contains contributions from instrument, model, and representation errors. We estimate the total observational error by applying the Relative Residual Error (RRE) method to actual TES data and corresponding GEOS-Chem  $y_R$  (Heald et al., 2004). This method

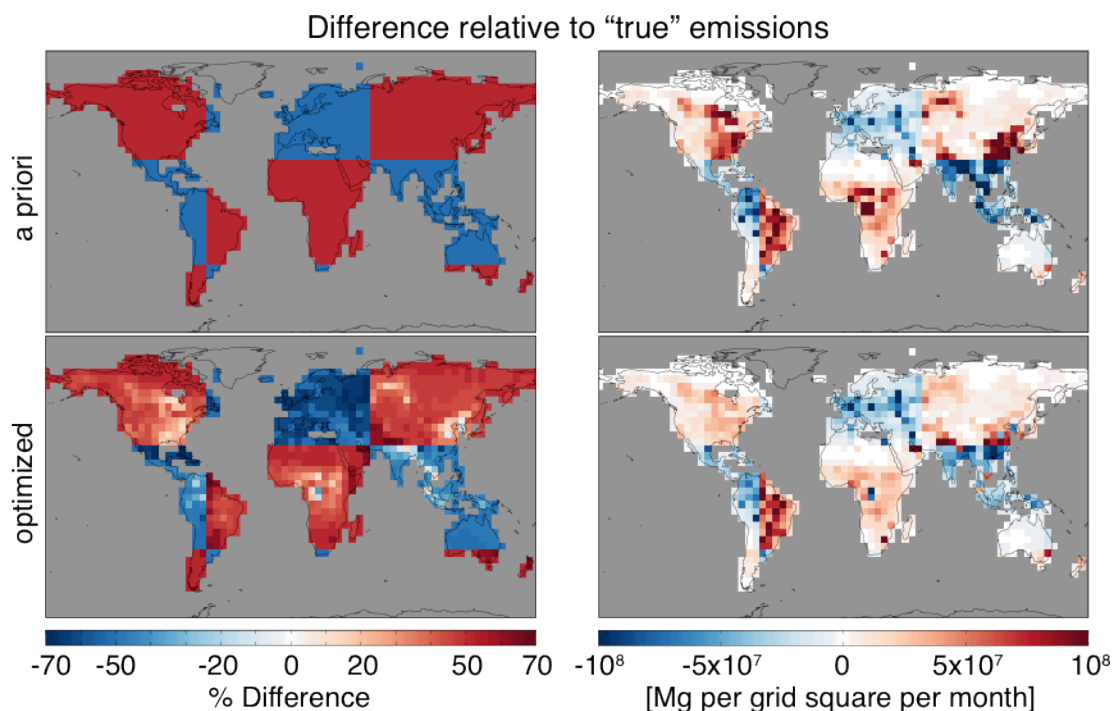


**Figure 2.8:** Relative (left) and absolute (right) error of a priori (top) and optimized (bottom) methane emissions. Red and blue represent over and underestimates respectively. Gray represents regions covered by ocean or ice.

attributes the temporal mean of model-observation differences for a given grid square to an error in methane emissions, and the residual to observational error. We calculate a mean 44.6 ppb RRE for the ensemble of TES observations used in the V004 validation and use this value to populate the diagonal of  $S_e$ . From the residual difference between HIPPO and GEOS-Chem RTVMR, we estimate a combined model and representation error of 16.3 ppb, indicating that the observational error is principally contributed by the instrument error.

Error correlations between observations can be neglected at  $4^\circ \times 5^\circ$  resolution (Heald et al., 2004), so  $S_e$  is diagonal.  $S_a$  is also diagonal and assigns 50% error to emissions, commensurate with the perturbation made to the “true” emissions. Although

the a priori errors in figure 2.8 are highly spatially correlated through the use of homogeneous perturbations in large blocks, this correlation is mainly for ease of interpretation and we would not expect such correlation in actual a priori errors. We therefore do not include error covariance terms in  $\mathbf{S}_a$ .

We use GEOS-Chem and its adjoint to iteratively solve  $\nabla_{\mathbf{x}}J(\mathbf{x}) = 0$ . The GEOS-Chem adjoint was developed by Henze et al. (2007) with application to CO source optimization by Kopacz et al. (2009). Our application to methane follows that for CO. The GEOS-Chem adjoint methane simulation calculates  $\nabla_{\mathbf{x}}J(\mathbf{x})$ , and in combination with a steepest descent algorithm, iterates to find  $\nabla_{\mathbf{x}}J(\mathbf{x}) = 0$ .

Figures 2.8 and 2.9 show the extent to which the optimization can correct the initially wrong a priori. TES has success for some individual  $4^\circ \times 5^\circ$  grid squares with particularly large emissions and therefore large  $\nabla_{\mathbf{x}}J(\mathbf{x})$ . In general, however, it corrects less than half of the a priori error. We conclude that V004 is only of limited value for constraining methane emissions. Considering that most of the observational error is due to instrument error, reducing that error would improve the inversion. The TES V005 data with smaller errors and higher DOFS therefore hold promise but quantitative testing must await availability of a global database of averaging kernels.

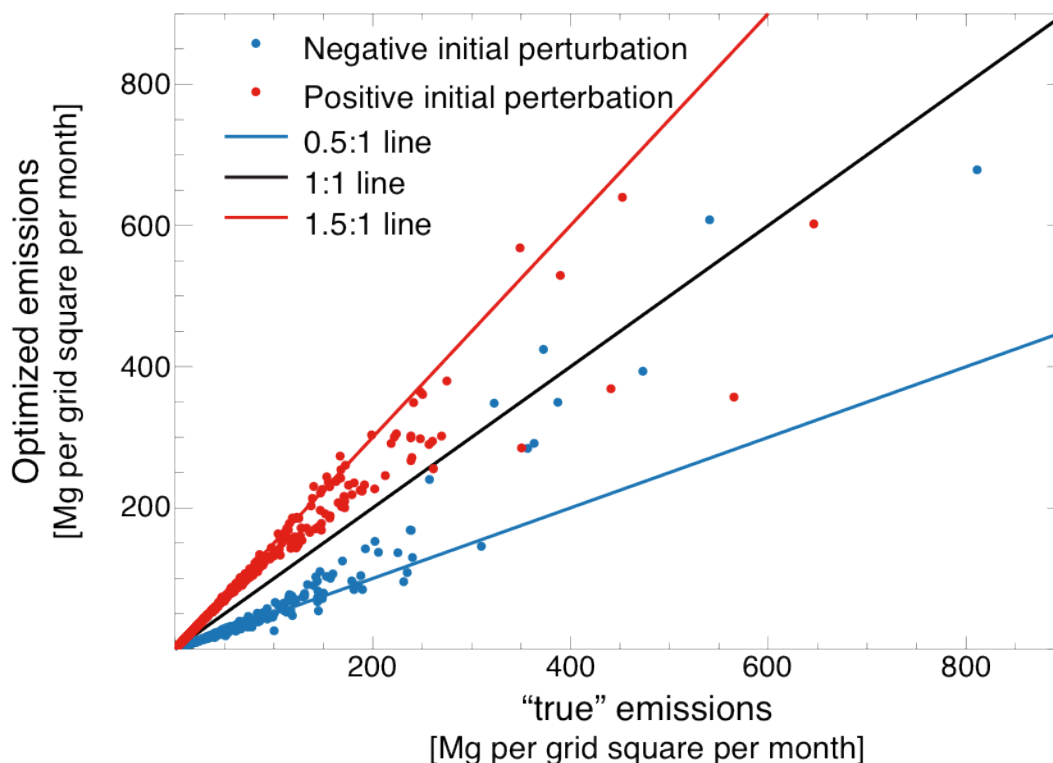


**Figure 2.9:** Scatterplot of optimized vs. “true” methane emissions for individual  $4^{\circ}\times 5^{\circ}$  grid squares. Blue and red points show emissions with negative and positive a priori perturbations, respectively. The a priori perturbations correspond to the blue and red lines.

## Acknowledgements

This work was supported by the US National Science Foundation under the HIPPO Program, by the NASA Atmospheric Composition Modeling and Analysis Program, and by a NASA Earth System Science Fellowship to KJW.

## References

- Bergamaschi, P., Krol, M., Dentener, F., Vermeulen, A., Meinhardt, F., Graul, R., Ramonet, M., Peters, W. and Dlugokencky, E.: Inverse modelling of national and European CH<sub>4</sub> emissions using the atmospheric zoom model TM5, *Atmos Chem Phys*, 5, 2431–2460, 2005.
- Bergamaschi, P., Frankenberg, C., Meirink, J. F., Krol, M., Dentener, F., Wagner, T., Platt, U., Kaplan, J. O., Korner, S., Heimann, M., Dlugokencky, E. J. and Goede A.: Satellite cartography of atmospheric methane from SCIAMACHY on board ENVISAT: 2. Evaluation based on inverse model simulations, *J. Geophys. Res.*, 112, D02304, doi:10.1029/2006JD007268, 2007.
- Bergamaschi, P., Frankenberg, C., Meirink, J. F., Krol, M., Villani, M. G., Houweling, S., Dentener, F., Dlugokencky, E. J., Miller, J. B., Gatti, L. V., Engel, A. and Levin I.: Inverse modeling of global and regional CH<sub>4</sub> emissions using SCIAMACHY satellite retrievals, *J. Geophys. Res.*, 114(D22), D22301, doi:10.1029/2009JD012287, 2009.
- Bergamaschi, P., Krol, M., Meirink, J. F., Dentener, F., Segers, A., Van Aardenne, J., Monni, S., Vermeulen, A. T., Schmidt, M., Ramonet, M., Yver, C. Meinhardt, F., Nisbet, E. G., Fisher, R. E., O'Doherty, S. and Dlugokencky, E. J.: Inverse modeling of European CH<sub>4</sub> emissions 2001–2006, *J. Geophys. Res.*, 115(D22), D22309, doi:10.1029/2010JD014180, 2010.
- Bowman, K., Rodgers, C., Kulawik, S., Worden, J., Sarkissian, E., Osterman, G., Steck, T., Lou, M., Eldering, A., Shephard, M., Worden, H., Lampel, M., Clough, S., Brown, P., Rinsland, C., Gunson, M., and Beer, R.: Tropospheric emission spectrometer: Retrieval method and error analysis, *Ieee T Geosci Remote*, 44(5), 1297–1307, doi:10.1109/TGRS.2006871234, 2006.
- Bousquet, P., Ciais, P., Miller, J. B., Dlugokencky, E. J., Hauglustaine, D. A., Prigent, C., Van der Werf, G. R., Peylin, P., Brunke, E. G., Carouge, C., Langenfelds, R. L., Lathière, J., Papa, F., Ramonet, M., Schmidt, M., Steele, L. P., Tyler, S. C. and White, J.: Contribution of anthropogenic and natural sources to atmospheric methane variability, *Nature*, 443(7110), 439–443, doi:10.1038/nature05132, 2006.
- Boxe, C.S., Worden, J. R., Bowman, K. W., Kulawik, S. S., Neu, J. L., Ford, W. C., Osterman, G. B., Herman, R. L., Eldering, A., Tarasick, D. W., Thompson, A. M., Doughty, D. C., Hoffmann, M. R., and Oltmans, S. J.: Validation of northern latitude Tropospheric Emission Spectrometer stare ozone profiles with ARC-IONS sondes during ARCTAS: sensitivity, bias and error analysis, *Atmos Chem Phys*, 10, 9901–9914, 2010.
- Chen, Y.-H. and Prinn, R. G.: Estimation of atmospheric methane emissions between 1996 and 2001 using a three-dimensional global chemical transport model, *J Geophys Res-Atmos*, 111(D10), D10307, doi:10.1029/2005JD006058, 2006.
- Clerbaux, C., Hadji-Lazaro, J., Turquety, S., Megie, G. and Coheur, P.: Trace gas measurements from infrared satellite for chemistry and climate applications, *Atmos*

Chem Phys, 3, 1495–1508, 2003.

Crevoisier, C., Nobileau, D., Fiore, A. M., Armante, R., Chedin, A. and Scott, N. A.: Tropospheric methane in the tropics - first year from IASI hyperspectral infrared observations, *Atmos Chem Phys*, 9(17), 6337–6350, 2009.

Denman, K. L., Brasseur, G., Chidthaisong, A., Ciais, P., Cox, P. M., Dickinson, R. E., Hauglustaine, D., Heinze, C., Holland, E., Jacob, D., Lohmann, U., Ramachandran, S., da Silva Dias, P. L., Wofsy, S. C., and Zhang, X.: *Climate Change 2007: The Physical Science Basis. Contribution of working group 1 to the fourth assessment report of the Intergovernmental Panel on Climate Change*, chap. Changes in Atmospheric Constituents and in Radiative Forcing, Cambridge University Press, Cambridge and New York, 499–587, 2007.

Dils, B., De Maziere, M., Muller, J., Blumenstock, T., Buchwitz, M., de Beek, R., Demoulin, P., Duchatelet, P., Fast, H., Frankenberg, C., Gloudemans, A., et al.: Comparisons between SCIAMACHY and ground-based FTIR data for total columns of CO, CH<sub>4</sub>, CO<sub>2</sub> and N<sub>2</sub>O, *Atmos Chem Phys*, 6, 1953–1976, 2006.

Elkins, J. W., Fahey, D. W., Gilligan, J. M., Dutton, G. S., Baring, T. J., Volk, C. M., Dunn, R. E., Myers, R. C., Montzka, S. A., Wamsley, P. R., Hayden, A. H., Butler, J. H., Thompson, T. M., Swanson, T. H., Dlugokencky, E. J., Novelli, P. C., Hurst, D. F., Lobert, J. M., Ciciora, S. J., McLaughlin, R. J., Thompson, T. L., Winkler, R. H., Fraser, P. J., Steele, L. P., and Lucarelli, M. P.: Airborne gas chromatograph for in situ measurements of long-lived species in the upper troposphere and lower stratosphere, *Geophys Res Lett*, 23(4), 347–350, 1996.

Etheridge, D., Steele, L., Francey, R. and Langenfelds, R.: Atmospheric methane between 1000 AD and present: Evidence of anthropogenic emissions and climatic variability, *J Geophys Res-Atmos*, 103(D13), 15979–15993, 1998.

Fletcher, S., Tans, P., Bruhwiler, L., Miller, J. and Heimann, M.: CH<sub>4</sub> sources estimated from atmospheric observations of CH<sub>4</sub> and its C-13/C-12 isotopic ratios: 1. Inverse modeling of source processes, *Global Biogeochem Cy*, 18(4), GB4004, doi:10.1029/2004GB002223, 2004.

Forster, P., Ramaswamy, V., Artaxo, P., Bernsten, T., Betts, R., Fahey, D. W., Haywood, J., Lean, J., Lowe, D. C., Myhre, G., Nganga, J., Prinn, R., Raga, G., Schultz, M., and Van Dorland, R.: Changes in Atmospheric Constituents and in Radiative Forcing, in: *Climate Change 2007: The Physical Science Basis. Contribution of Working Group I to the Fourth Assessment Report of the Intergovernmental Panel on Climate Change*, edited by: Solomon, S., Qin, D., Manning, M., Chen, Z., Marquis, M., Averyt, K. B., Tignor, M. and Miller, H. L., Cambridge University Press, Cambridge, United Kingdom and New York, NY, USA, 2007.

Frankenberg, C., Aben, I., Bergamaschi, P., Dlugokencky, E. J., van Hees, R., Houweling, S., van der Meer, P., Snel, R. and Tol, P.: Global column-averaged methane

mixing ratios from 2003 to 2009 as derived from SCIAMACHY: Trends and variability, *J. Geophys. Res.*, 116(D4), D02304, doi:10.1029/2010JD014849, 2011.

Heald, C., Jacob, D., Jones, D., Palmer, P., Logan, J., Streets, D., Sachse, G., Gille, J., Hoffman, R. and Nehrkorn, T.: Comparative inverse analysis of satellite (MOPITT) and aircraft (TRACE-P) observations to estimate Asian sources of carbon monoxide, *J Geophys Res-Atmos*, 109(D23), D23306, doi:10.1029/2004JD005185, 2004.

Hein, R., Crutzen, P. and Heimann, M.: An inverse modeling approach to investigate the global atmospheric methane cycle, *Global Biogeochem Cy*, 11(1), 43–76, 1997.

Henze, D. K., Hakami, A., and Seinfeld, J. H.: Development of the adjoint of GEOS-Chem, *Atmos Chem Phys*, 7, 2413-2433, 2007.

Houweling, S., Kaminski, T., Dentener, F., Lelieveld, J. and Heimann, M.: Inverse modeling of methane sources and sinks using the adjoint of a global transport model, *J Geophys Res-Atmos*, 104(D21), 26137–26160, 1999.

Hurst, D. F., Dutton, G. S., Romashkin, P. A., Wamsley, P. R., Moore, F. L., Elkins, J. W., Hintsa, E. J., Weinstock, E. M., Herman, R. L., Moyer, E. J., Scott, D. C., May, R. D., and Webster, C. R.: Closure of the total hydrogen budget of the northern extratropical lower stratosphere, *J Geophys Res-Atmos*, 104(D7), 8191-8200, 1999.

Kobayashi, H., Shimota, A., Kondo, K., Okumura, E., Kameda, Y., Shimoda, H. and Ogawa, T.: Development and evaluation of the interferometric monitor for greenhouse gases: a high-throughput Fourier-transform infrared radiometer for nadir Earth observation, *Appl Optics*, 38(33), 6801–6807, 1999.

Kopacz, M., Jacob, D. J., Henze, D. K., Heald, C. L., Streets, D. G., Zhang, Q.: Copmarison of adjoint and analytical Bayesian inversion methods for constraining Asian sources of carbon monoxide using satellite (MOPITT) measurements of CO columns, *J. Geophys. Res.*, 114, D04305, doi:10.1029/2007JD009264, 2009.

Kort, E. A., Patra, P. K., Ishijima, K., Daube, B. C., Jiménez, R., Elkins, J., Hurst, D., Moore, F. L., Sweeney, C. and Wofsy, S. C.: Tropospheric distribution and variability of N<sub>2</sub>O: Evidence for strong tropical emissions, *Geophys Res Lett*, 38(15), L15806, doi:10.1029/2011GL047612, 2011.

Meirink, J., Eskes, H. and Goede, A.: Sensitivity analysis of methane emissions derived from SCIAMACHY observations through inverse modelling, *Atmos Chem Phys*, 6, 1275–1292, 2006.

Meirink, J. F., Bergamaschi, P., Frankenberg, C., D'amelio, M. T. S., Dlugokencky, E. J., Gatti, L. V., Houweling, S., Miller, J. B., Röckmann, T., Villani, M. G. and Krol, M. C.: Four-dimensional variational data assimilation for inverse modeling of atmospheric methane emissions: Analysis of SCIAMACHY observations, *J. Geophys. Res.*, 113(D17), D17301, doi:10.1029/2007JD009740, 2008a.



Meirink, J. F., Bergamaschi, P. and Krol, M. C.: Four-dimensional variational data assimilation for inverse modelling of atmospheric methane emissions: method and comparison with synthesis inversion, *Atmos Chem Phys*, 8(21), 6341–6353, 2008b.

Morino, I., Uchino, O., Inoue, M., Yoshida, Y., Yokota, T., Wennberg, P. O., Toon, G. C., Wunch, D., Roehl, C. M., Notholt, J., Warneke, T., et al.: Preliminary validation of column-averaged volume mixing ratios of carbon dioxide and methane retrieved from GOSAT short-wavelength infrared spectra, *Atmos. Meas. Tech.*, 4(6), 1061–1076, doi:10.5194/amt-4-1061-2011, 2011.

Nassar, R., Logan, J. A., Worden, H. M., Megretskaya, I. A., Bowman, K. W., Osterman, G. B., Thompson, A. M., Tarasick, D. W., Austin, S., Claude, H., Dubey, M. K., Hocking, W. K., Johnson, B. J., Joseph, E., Merrill, J., Morris, G. A., Newchurch, M., Oltmans, S. J., Ponsy, F., Schmidlin, F. J., Vömel, H., Whiteman, D. N. and Witte, J. C.: Validation of Tropospheric Emission Spectrometer (TES) nadir ozone profiles using ozonesonde measurements, *J Geophys Res-Atmos*, 113(D15), D15S17, doi:10.1029/2007JD008819, 2008.

Payne, V. H., Clough, S. A., Shephard, M. W., Nassar, R. and Logan, J. A.: Information-centered representation of retrievals with limited degrees of freedom for signal: Application to methane from the Tropospheric Emission Spectrometer, *J. Geophys. Res.*, 114(D10), D10307, doi:10.1029/2008JD010155, 2009.

Pickett-Heaps, C. A., Jacob, D. J., Wecht, K. J., Kort, E. A., Wofsy, S. C., Diskin, G. S., Worthy, D. E. J., Kaplan, J. O., Bey, I. and Drevet, J.: Magnitude of seasonality of wetland methane emissions from the Hudson Bay Lowlands (Canada), *Atmos Chem Phys*, 11(8), 3773–3779, 2011.

Razavi, A., Clerbaux, C., Wespes, C., Clarisse, L., Hurtmans, D., Payan, S., Camy-Peyret, C. and Coheur, P. F.: Characterization of methane retrievals from the IASI spaceborne sounder, *Atmos Chem Phys*, 9(20), 7889–7899, 2009.

Rodgers, C.D.: *Inverse Methods for Atmospheric Sounding*, World Scientific Publishing Co. Pte. Ltd, Tokyo 2000.

Sussmann, R., Stremme, W., Buchwitz, M. and de Beek, R.: Validation of ENVISAT/SCIAMACHY columnar methane by solar FTIR spectrometry at the ground-truthing station zugspitze, *Atmos Chem Phys*, 5, 2419–2429, 2005.

Villani, M. G., Bergamaschi, P., Krol, M., Meirink, J. F. and Dentener, F.: Inverse modeling of European CH<sub>4</sub> emissions: sensitivity to the observational network, *Atmos Chem Phys*, 10(3), 1249–1267, 2010.

Wofsy, S. C. the HIPPO Science Team and Cooperating Modellers and Satellite Teams: HIAPER Pole-to-Pole Observations (HIPPO): fine-grained, global-scale measurements of climatically important atmospheric gases and aerosols, *Philosophical Transactions of the Royal Society A: Mathematical, Physical and Engineering Sciences*, 369(1943), 2073–2086, doi:10.1098/rsta.2010.0313, 2011.

- Worden, H. M., Logan, J. A., Worden, J. R., Beer, R., Bowman, K., Clough, S. A., Eldering, A., Fisher, B. M., Gunson, M. R., Herman, R. L., Kulawik, S. S., et al.: Comparisons of Tropospheric Emission Spectrometer (TES) ozone profiles to ozonesondes: Methods and initial results, *J. Geophys. Res.*, 112(D3), D03309, doi:10.1029/2006JD007258, 2007.
- Worden, J., Kulawik, S., Shephard, M., Clough, S., Worden, H., Bowman, K. and Goldman, A.: Predicted errors of tropospheric emission spectrometer nadir retrievals from spectral window selection, *J Geophys Res-Atmos*, 109(D9), D09308, doi:10.1029/2004JD004522, 2004.
- Worden, J., Kulawik, S., Frankenberg, C., Bowman, K., Payne, V., Cady-Peirara, K., Wecht, K., Lee, J-E., Noone, D., Risi, C.: Profiles of CH<sub>4</sub>, HDO, H<sub>2</sub>O, and N<sub>2</sub>O with improved lower tropospheric vertical resolution from Aura TES radiances, *Atmos. Meas. Tech. Discuss.*, 4, 6679-6721, 2012.
- Xiong, X., Barnett, C., Maddy, E., Sweeney, C., Liu, X., Zhou, L. and Goldberg, M.: Characterization and validation of methane products from the Atmospheric Infrared Sounder (AIRS), *J. Geophys. Res.*, 113(null), G00A01, doi:10.1029/2007JG000500, 2008.
- Yokota, T., Yoshida, Y., Eguchi, N., Ota, Y., Tanaka, T., Watanabe, H. and Maksyutov, S.: Global Concentrations of CO<sub>2</sub> and CH<sub>4</sub> Retrieved from GOSAT: First Preliminary Results, *Sola*, 5, 160–163, doi:10.2151/sola.2009-041, 2009.

# **Chapter 3. Mapping of North American methane emissions with high spatial resolution by inversion of SCIAMACHY satellite data**

[Wecht, K.J., Jacob, D.J., Frankenberg, C., Blake, D.R., and Jiang, Z., in preparation for submission]

## **Abstract**

We estimate methane emissions from North America with high spatial resolution by inversion of SCIAMACHY satellite observations using the GEOS-Chem chemical transport model and its adjoint. The inversion focuses on summer 2004 when data from the INTEx-A aircraft campaign over the eastern US are available to validate the SCIAMACHY retrievals and evaluate the inversion. From the INTEx-A data we identify and correct a water vapor-dependent bias in the SCIAMACHY data. We conduct an initial inversion of emissions on the horizontal grid of GEOS-Chem ( $1/2^\circ \times 2/3^\circ$ ) to identify correction tendencies relative to the EDGAR v4.2 emission inventory used as a priori. We then cluster these grid cells with a hierarchical algorithm to extract the maximum information from the SCIAMACHY observations. A 1000-cluster ensemble can be adequately constrained, providing  $\sim 100$  km resolution across North America. Analysis of results indicates that the Canadian wetlands source is lower than the a priori but consistent with other recent estimates. Anthropogenic US emissions are  $32.0 \pm 1.3 \text{ Tg a}^{-1}$ , compared to  $25.8 \text{ Tg a}^{-1}$  and  $28.3 \text{ Tg a}^{-1}$  in the EDGAR v4.2 and EPA inventories

respectively. We find that US livestock emissions are underestimated by 60-70% in these two inventories. No such discrepancy is apparent for overall US gas/oil emissions, although this may reflect some compensation between overestimate of emissions from storage/distribution and underestimate from production. We find that US livestock emissions are twice the gas/oil emissions, in contrast to the EDGAR v4.2 and EPA inventories where these two sources are of comparable magnitude.

### **3.1 Introduction**

Methane is the second most powerful anthropogenic greenhouse gas after carbon dioxide (Myhre et al. 2013). Major anthropogenic sources include natural gas extraction and use, coal mining, landfills, livestock, rice cultivation, and biomass burning. Wetlands are the largest natural source. The magnitude of global methane emissions is constrained within  $\pm 15\%$  by knowledge of the global sink from oxidation by OH, but the magnitudes and trends of emissions from different source types and source regions are highly uncertain (Myhre et al. 2013, Hartmann et al. 2013). Reducing methane emissions has been identified as a low-cost priority in greenhouse gas emissions reduction strategies (IEA World Energy Outlook 2013, van Vuuren et al. 2006, Weyant et al. 2006) but this requires that the sources be quantified. The United States (US) Environmental Protection Agency (EPA) provides national emission inventories for methane (EPA, 2013). However, a number of studies using atmospheric observations from surface and aircraft suggest that these inventories may be too low by a factor of two or more (Katzenstein et al. 2002; Xiao et al. 2008; Kort et al. 2008; Petron et al. 2012; Santoni et al. submitted; Miller et al. 2013a; Karion et al. 2013).

Satellite observations of atmospheric methane provide a resource for constraining emissions, as first demonstrated by Bergamaschi et al. (2007). Satellites deliver dense spatial coverage unachievable by surface networks or aircraft campaigns. Methane has been retrieved from nadir satellite measurements of solar backscatter in the short-wave infrared (SWIR) and terrestrial radiation in the thermal infrared (TIR). SWIR retrievals are available from SCIAMACHY (2003-2012; Frankenberg et al. 2011) and GOSAT (2009-present; Parker et al. 2011; Schepers et al. 2012). TIR retrievals are available from AIRS (2002-present; Xiong et al., 2008), TES (2004-2011; Worden et al. 2012), and IASI (2007-present; Xiong et al. 2013; Crevoisier et al. 2013). SWIR retrievals provide total atmospheric columns. TIR retrievals provide vertical profiles but with low sensitivity to the lower troposphere due to lack of thermal contrast, and this limits their value for detecting regional sources (Wecht et al., 2012). SCIAMACHY had full global coverage with a six-day return time. Current coverage by GOSAT is much sparser. Instrument degradation limited the value of the SCIAMACHY data after 2005 (Frankenberg et al. 2011). The TROPOMI instrument to be launched in 2015 will provide SWIR methane data with global daily coverage and  $7\times 7\text{ km}^2$  nadir resolution (Veefkind et al., 2012).

Here we use SCIAMACHY observations for July-August 2004 in an inversion of methane sources in North America with the adjoint of the GEOS-Chem chemical transport model (CTM) at  $1/2^\circ\times 2/3^\circ$  ( $\sim 50\times 50\text{ km}^2$ ) resolution. This time window takes advantage of concurrent methane observations from the NASA INTEx-A aircraft mission over the eastern US (Singh et al., 2006) that offer extensive vertical profile information (for satellite validation) and boundary layer mapping (for complementary source characterization). The EPA (2013) emission inventory shows no significant

change from 2005 to 2011, implying that constraints on 2004 emissions should be relevant to present-day.

A number of previous studies have used SCIAMACHY data for global inverse modeling of methane sources (Bergamaschi et al. 2007; Meirink et al. 2008; Bergamaschi et al., 2009; Bergamaschi et al. 2013; Monteil et al. 2013; Cressot et al. 2013; Houweling et al. 2013). All have recognized the need for correcting bias in the SCIAMACHY data that otherwise propagates to the inverse solution. An early validation of SCIAMACHY using ground based Fourier transform spectrometers (Dils et al. 2006) failed to identify retrieval error related to inaccuracies in water vapor spectroscopic parameters (Frankenberg et al. 2008). More recently, Houweling et al. (2013) show that bias in SCIAMACHY is correlated with tropospheric water vapor concentrations. As we show below, a water vapor correction enables successful validation of the SCIAMACHY data with the INTEx-A vertical profiles.

Our work goes beyond the above studies in using SCIAMACHY for a continental-scale optimization of methane sources with high resolution, including validation and verification with independent aircraft data. The adjoint-based approach allows us to exploit the density of the satellite observations to optimize emissions at the  $1/2^\circ \times 2/3^\circ$  native resolution of GEOS-Chem, but we show that too fine a resolution can inhibit successful inversion by diluting the information from the observations. Previous studies have proposed methods for coarsening the discretization of model emissions in a way that optimizes the inversion (Bocquet 2005; Bocquet 2009; Bocquet et al. 2011; Wu et al. 2011). These methods require laborious construction of the Jacobian of the CTM, which is precisely what we seek to avoid by using the adjoint method. Here we introduce

a hierarchical clustering algorithm to optimize the discretization of emissions in the context of adjoint-based inverse modeling.

### 3.2 Observations

SCIAMACHY is in a sun-synchronous polar orbit with an equator overpass local time of  $\sim 10:00$ . It retrieves methane from nadir SWIR spectra at  $1.66\text{-}1.67\ \mu\text{m}$  with a nadir footprint of  $30 \times 60\ \text{km}^2$  and cross-track scanning. It achieves complete global coverage every 6 days. Observations are limited to daytime and land. We use the Iterative Maximum A Posteriori (IMAP) v5.5 retrieval from Frankenberg et al. (2011). The retrieval first calculates the methane vertical column density  $\Omega_{CH_4}$  [molecules  $\text{cm}^{-2}$ ]:

$$\Omega_{CH_4} = \Omega_a + \mathbf{a}^T(\boldsymbol{\omega} - \boldsymbol{\omega}_A) \quad (3.1)$$

where  $\boldsymbol{\omega}$  is the true vertical profile of methane, consisting of 20 partial columns on a vertical grid,  $\boldsymbol{\omega}_A$  is the a priori profile provided by the TM5-4DVAR CTM (Meirink et al. 2008),  $\Omega_A$  is the corresponding a priori column concentration, and  $\mathbf{a}$  is an averaging kernel vector that describes the sensitivity of the retrieved column to each partial column in  $\boldsymbol{\omega}$ . The sensitivity measured by  $\mathbf{a}$  is nearly uniform throughout the troposphere and decreases with altitude in the stratosphere. To account for the impact of aerosols and partial cloud cover on the observed light path,  $\Omega_{CH_4}$  is normalized and converted to a column mixing ratio  $X_{CH_4}$  [v/v] using the  $\text{CO}_2$  proxy method described in detail by Frankenberg et al. (2006):

$$X_{CH_4} = (\Omega_{CH_4} / \Omega_{CO_2}) X_{CO_2} \quad (3.2)$$

where  $\Omega_{CO_2}$  is the vertical column density of  $\text{CO}_2$  also retrieved by SCIAMACHY, and  $X_{CO_2}$  is a modeled column mixing ratio of  $\text{CO}_2$ .  $\text{CO}_2$  is used for normalization because it

is retrieved in a spectrally neighboring fitting window and its mixing ratio is known with much higher precision than methane.

The IMAP v5.5 product was previously validated by Houweling et al. (2013), who used coincident observations from the Total Carbon Column Observing Network (TCCON) to identify a seasonally-dependent bias that they attributed to water vapor. Here we use in situ vertical profiles from the INTEx-A aircraft during summer 2004. The aircraft flew over the eastern US with extensive boundary layer legs (Figure 3.1, right panel) and vertical profiles extending up to 12 km. Methane was measured using gas chromatography from whole air flask samples collected every 4 minutes with accuracy of 1.0 ppb and precision of 0.1 ppb (Colman et al. 2001; <http://www-air.larc.nasa.gov/cgi-bin/arcstat>). For SCIAMACHY validation we require vertical profiles that span from at least 900 to 400 hPa and coincide with SCIAMACHY overpasses within  $\pm 150$  km and  $\pm 6$  h. We find 9 profiles satisfying these criteria, each corresponding to 7 to 29 satellite observations. We map the aircraft profiles on the 12 levels of the SCIAMACHY retrieval pressure grid, extrapolate above the DC-8 ceiling using the SCIAMACHY a priori profile, and apply equation (3.1) to simulate the SCIAMACHY retrieval. From there we derive  $X_{CH_4}$  by dividing by the local air column density. We average the coincident SCIAMACHY observations and compute the SCIAMACHY-INTEx difference  $\Delta X_{CH_4}$ . Results indicate a mean bias  $\Delta X_{CH_4} = -14.2$  ppb (0.8%) and a residual standard deviation of 29.2 ppb (1.6%) for individual SCIAMACHY observations.

Previous studies have demonstrated the need for a latitudinally dependent SCIAMACHY bias correction (Bergamaschi et al 2007; Meirink et al. 2008;



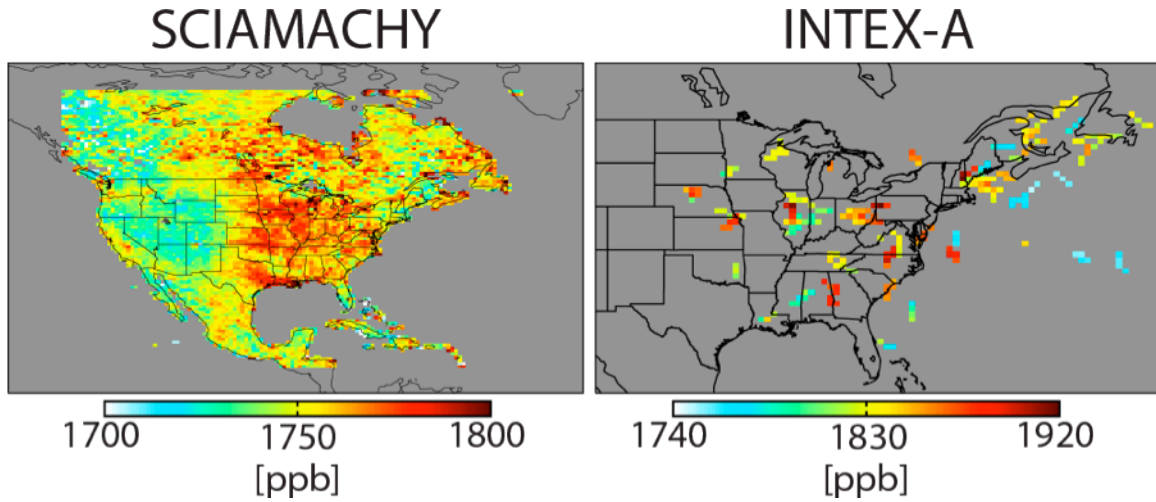


**Figure 3.1:** Methane over North America during the INTEX-A aircraft campaign (1 July – 14 August 2004): SCIAMACHY mean column mixing ratios (left) and INTEX-A mixing ratios below 850 hPa (right). Observations are averaged spatially on the  $1/2^\circ \times 2/3^\circ$  GEOS-Chem grid and temporally over the INTEX-A campaign duration. Note the difference in scales between the two panels.

Bergamaschi et al. 2009; Bergamaschi et al. 2013; Cressot et al. 2013). Some have documented the interference of water vapor as the cause of the bias (Frankenberg et al. 2008; Houweling et al. 2013) and we seek such a relationship here. Figure 3.2 (left panel) shows the relationship of  $\Delta X_{CH_4}$  with the average pressure-weighted specific humidity in the 900-400 hPa column measured by the INTEX-A aircraft. There is a linear relationship (weighted  $R^2 = 0.69$ ) that implies a negative bias under dry conditions and a positive dependence of the bias on humidity. We use this relationship to calculate a linear bias correction factor and apply it to the original IMAP v5.5 retrieval. After the correction we find an insignificant mean bias  $\Delta X_{CH_4} = 2.5$  ppb (0.1 %) and residual standard deviation of 28.2 ppb (1.6 %) for individual SCIAMACHY observations (Figure 3.2, right panel). The residual standard deviation (which we take to represent SCIAMACHY random measurement error) is consistent with the average IMAP v5.5 theoretical error of 30.9

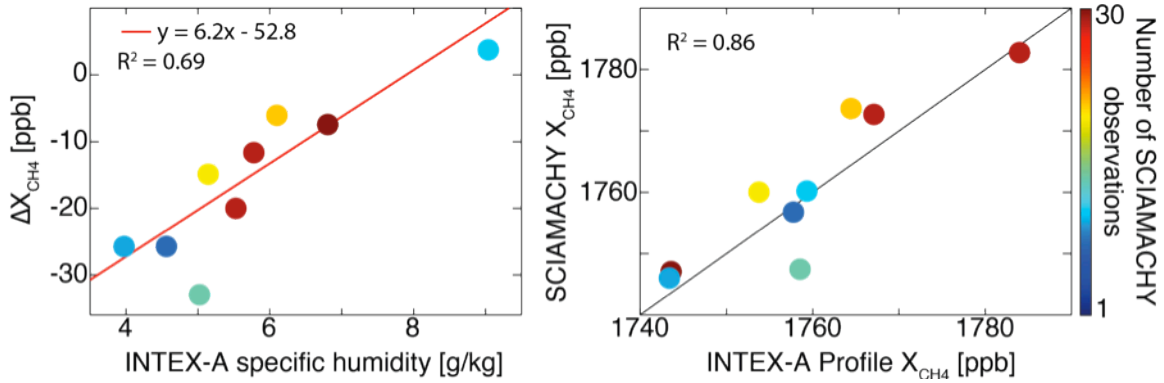


**Figure 3.2:** Validation of the SCIAMACHY IMAP v5.5 retrieval of methane column mixing ratio ( $X_{CH_4}$ ) with coincident INTEX-A aircraft vertical profiles (see text). Left: difference  $\Delta X_{CH_4}$  between SCIAMACHY and INTEX-A plotted as a function of the mean pressure-weighted specific humidity in the 900–400 hPa column measured by the INTEX-A aircraft. The red line shows a linear regression weighted by the number of SCIAMACHY observations. Regression parameters and weighted  $R^2$  are shown inset. Right: comparison of SCIAMACHY and INTEX-A  $X_{CH_4}$  after applying the water vapor correction from the linear regression. Weighted  $R^2$  is shown inset and the 1:1 line is also shown. Colors represent the number of SCIAMACHY observations averaged around each INTEX-A profile.

ppb (1.7 %) reported by Frankenberg et al. (2011). All SCIAMACHY data shown here include the specific humidity correction applied with the local GEOS-5 meteorological data used to drive GEOS-Chem.

Figure 3.1 (left) shows mean SCIAMACHY methane column mixing ratios during the INTEX-A period. Values are highest over the central US where there are large sources from livestock and from natural gas and oil (gas/oil) production. Values are also high over the Canadian wetlands in northern Ontario. The low values in the West reflect elevated terrain so that the stratosphere (where methane is depleted) makes a relatively large contribution to the column mixing ratio. Also shown in Figure 3.1 are the individual INTEX-A observations in the boundary layer (below 850 hPa). These show areas of high

concentrations in the Midwest and East but with fine-scale structure that must reflect in part day-to-day variability in meteorology. We do not use the INTEX-A data for the inversion but use them instead for validation (as described above) and as independent evaluation of the inversion results obtained from SCIAMACHY.

### **3.3 Optimization of methane emissions**

#### **3.3.1 GEOS-Chem model and a priori emissions**

We use the GEOS-Chem CTM v9-01-02 (<http://acmg.seas.harvard.edu/geos/index.html>) as the forward model for the inversion. GEOS-Chem is driven by GEOS-5 meteorological data from the NASA Global Modeling and Assimilation Office (GMAO). The GEOS-5 data have  $1/2^\circ$  latitude x  $2/3^\circ$  longitude horizontal resolution and 6-h temporal resolution (3-h for surface variables and mixing depths). Here we use the native  $1/2^\circ \times 2/3^\circ$  resolution for GEOS-Chem over North America and adjacent oceans ( $10\text{--}70^\circ\text{N}$ ,  $40\text{--}140^\circ\text{W}$ ), with 3-h dynamic boundary conditions from a global simulation with  $4^\circ \times 5^\circ$  resolution. This nested North American functionality of GEOS-Chem has been used previously in a number of air quality studies including extensive evaluation with observations (Park et al., 2004, 2006; L. Zhang et al., 2011, 2012; Y. Zhang et al. 2011; van Donkelaar et al. 2012). These show a good simulation of regional transport with no apparent biases.

The GEOS-Chem methane simulation was originally described by Wang et al. (2004) and updated by Pickett-Heaps et al. (2011). The main methane sink is tropospheric oxidation by OH, computed using a 3-D archive of monthly average OH

concentrations from a GEOS-Chem simulation of tropospheric chemistry (Park et al. 2004). The mean mass-weighted tropospheric OH concentration is  $10.8 \times 10^5$  molecules  $\text{cm}^{-3}$ . Additional minor sinks for methane are soil absorption (from Fung et al. 1991) and oxidation in the stratosphere. We use stratospheric methane loss frequencies archived from the NASA Global Modeling Initiative (GMI) model (Considine et al. 2008; Allen et al. 2010) as described by Murray et al. (2012). The resulting global mean atmospheric lifetime of methane is 8.9 years and the lifetime against oxidation by tropospheric OH is 9.9 years. Model intercomparisons in the literature give corresponding values of  $8.6 \pm 1.2$  years and  $9.8 \pm 1.6$  years (Voulgarakis et al., 2013). Prather et al. (2012) estimate corresponding values of  $9.1 \pm 0.9$  years and  $11.2 \pm 1.3$  years from observational constraints.

For the a priori emissions we use the 2004 anthropogenic inventory from EDGAR v4.2 with  $0.1^\circ \times 0.1^\circ$  resolution and no seasonality (EC-JRC/PBL 2009). Natural sources include temperature-dependent emissions from wetlands (Kaplan et al. 2002; Pickett-Heaps et al. 2011), termites (Fung et al. 1991), and daily GFED3 open fire emissions (van der Werf et al. 2010; Mu et al. 2010). Figure 3.3 shows total methane emissions for North America and the contributions from the five largest source types.

Table 3.1 lists US anthropogenic emission totals by source type in the EDGAR v4.2 and EPA inventories (the EPA inventory is available only as a national total). Total US anthropogenic emissions from EDGAR v4.2 and EPA are  $25.8$  and  $28.3 \text{ Tg a}^{-1}$ , respectively. EDGAR v4.2 and EPA give similar estimates for emissions by source type,

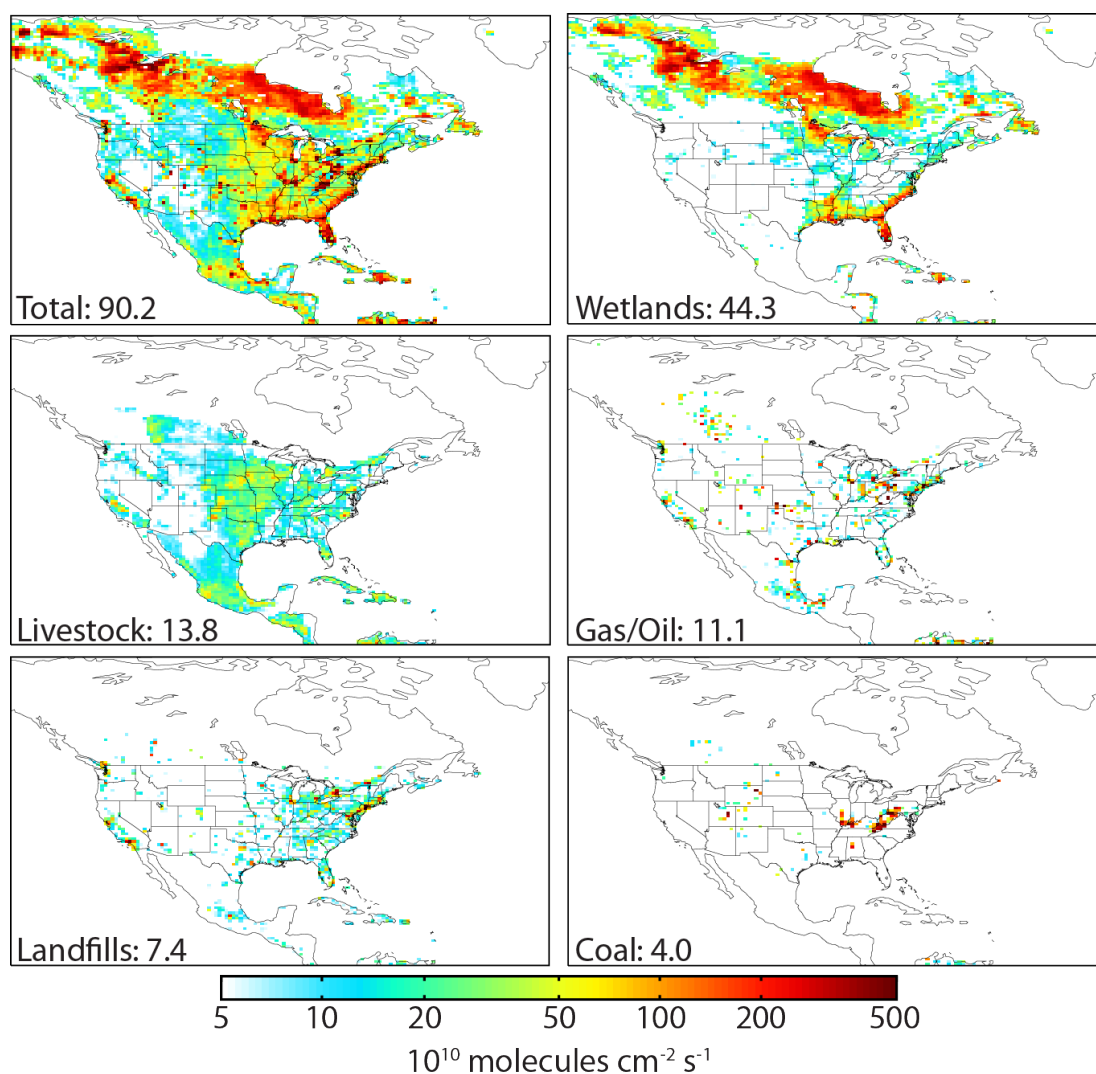


**Figure 3.3:** North American methane emissions used as a priori for the inversion: total emissions (top left panel) and contributions from the major source types. Inventories are from Kaplan et al. (2002) and Pickett-Heaps et al. (2011) for wetlands and from GEIA v 4.2 for all other (anthropogenic) sources. Values are averages for 22 June – 15 August 2004. Annual emission rates for 2004 ( $\text{Tg a}^{-1}$ ) are shown inset for the North America domain as encompassed by the figure.

**Table 3.1:** US anthropogenic sources of methane in 2004 [ $\text{Tg a}^{-1}$ ].

Source type	EPA (2013) <sup>a</sup>	EDGAR v4.2 <sup>b</sup>	This Work <sup>c</sup>
Total	28.3 (24.6, 32.3)	25.8	32.0 $\pm$ 1.3
Livestock	8.8 (7.7, 10.4)	8.5	14.1 $\pm$ 1.3
Natural Gas and Oil	9.0 (7.2, 13.4)	6.3	7.2 $\pm$ 0.6
Landfills	5.4 (2.5, 7.9)	5.3	5.8 $\pm$ 0.3
Coal Mining	2.7 (2.3, 3.2)	3.9	2.4 $\pm$ 0.3
Other <sup>d</sup>	2.4 (1.4, 4.2)	1.9	2.5 $\pm$ 0.2

<sup>a</sup> Values in parentheses represent lower and upper ends of 95% uncertainty ranges.

<sup>b</sup> Used as a priori for the inversion.

<sup>c</sup> Uncertainties on emissions from individual source types assume that the a priori source type distributions are correct (see text).

<sup>d</sup> Including waste water treatment, rice cultivation, biofuel use, and other small sources. According to EPA (2013), none of these sources account for more than 3% of total US anthropogenic emissions.

except for gas/oil and coal mining. EDGAR reports gas/oil emissions of  $6.3 \text{ Tg a}^{-1}$ , 30% lower than the EPA (2013) estimate of  $9.0 \text{ Tg a}^{-1}$ . It reports US coal mining emissions of  $3.9 \text{ Tg a}^{-1}$ , 40% higher than the EPA (2013) estimate of  $2.7 \text{ Tg a}^{-1}$ .

Figure 3.4 shows surface air methane concentrations from the global and nested GEOS-Chem simulations with a priori emissions as described above, compared to observations from the NOAA Global Monitoring Division (GMD) network (<http://www.esrl.noaa.gov/gmd/>). Boundary concentrations for the nested grid are archived at the edge of the North America domain. Comparison of GEOS-Chem with the NOAA data over the oceans show that the model simulates realistic latitudinal gradients. This conclusion is supported by comparison of GEOS-Chem to observations from the HIPPO campaign (Wofsy et al. 2012), which shows that GEOS-Chem simulates northern hemispheric latitudinal gradients without significant error (Turner et al. 2013).

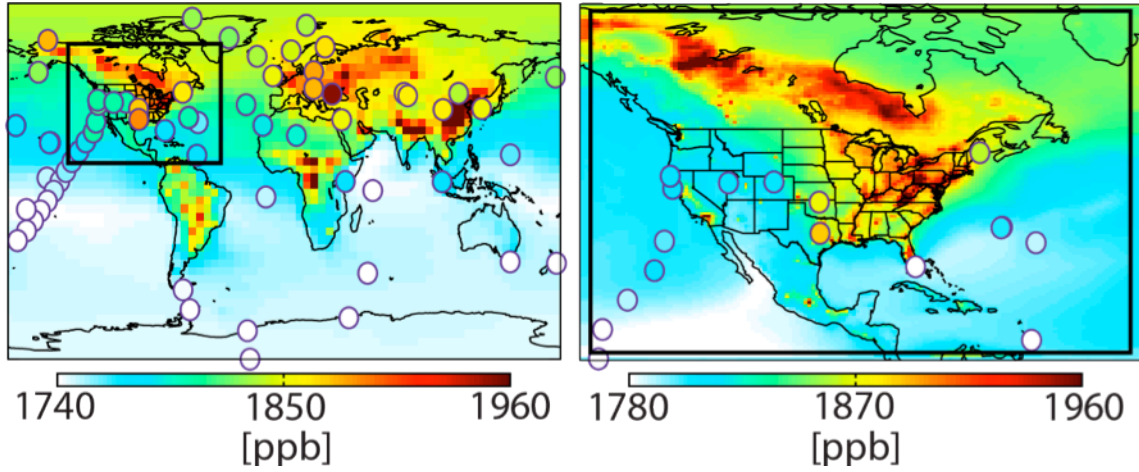


**Figure 3.4:** Methane concentrations in surface air averaged over the inversion period (22 June – 14 August 2004). The GEOS-Chem simulation with a priori sources (background) is compared to NOAA GMD observations (circles). Left: global simulation at  $4^\circ \times 5^\circ$  resolution used to archive a priori boundary concentrations for the nested simulation. Right: nested simulation at  $1/2^\circ \times 2/3^\circ$  resolution for the North America domain. Note difference in scale between panels. The NOAA GMD data were obtained from <http://www.esrl.noaa.gov/gmd/>.

### 3.3.2 Inversion Method

We seek to use the SCIAMACHY observations over North America during the INTEX-A period to optimize methane emissions on the  $1/2^\circ \times 2/3^\circ$  GEOS-Chem grid. Consider the ensemble of SCIAMACHY observations (column mean methane mixing ratios) assembled into an observation vector  $\mathbf{y}$ . Simulation of these observations over the North American domain of GEOS-Chem depends on the gridded emissions within the domain as well as on the boundary conditions (methane background concentrations) at the edges of the domain. We assemble the gridded emissions and the gridded boundary conditions into a state vector  $\mathbf{x}$ . Let  $F$  represent the GEOS-Chem model serving as forward model for the inversion. We have

$$\mathbf{y} = F(\mathbf{x}) + \boldsymbol{\varepsilon} \quad (3.3)$$

where  $\boldsymbol{\varepsilon}$  is the observational error and includes contributions from forward model error, representation error (sampling mismatch between observations and the model), and measurement error. Error statistics are represented by the observational error covariance matrix  $\mathbf{S}_O = E[\boldsymbol{\varepsilon}\boldsymbol{\varepsilon}^T]$  where  $E[\ ]$  is the expected value operator.

Bayesian optimization weighs the constraints on  $\mathbf{x}$  from the SCIAMACHY observations with the a priori estimates  $\mathbf{x}_A$  (error covariance matrix  $\mathbf{S}_A$ ). Applying Bayes' theorem and assuming Gaussian errors leads to an optimized estimate for  $\mathbf{x}$  by minimizing the cost function  $J(\mathbf{x})$  (Rodgers 2000):

$$J(\mathbf{x}) = (\mathbf{F}(\mathbf{x}) - \mathbf{y})^T \mathbf{S}_O^{-1} (\mathbf{F}(\mathbf{x}) - \mathbf{y}) + (\mathbf{x} - \mathbf{x}_A)^T \mathbf{S}_A^{-1} (\mathbf{x} - \mathbf{x}_A) \quad (3.4)$$

Minimization of  $J(\mathbf{x})$  is done with the GEOS-Chem adjoint model, developed by Henze et al. (2007) with application to methane source optimization by Wecht et al. (2012). The adjoint calculates  $\nabla_{\mathbf{x}}J(\mathbf{x}_A)$ , passes it to a steepest-descent algorithm that returns an improved estimate of  $\mathbf{x}$ , calculates  $\nabla_{\mathbf{x}}J(\mathbf{x})$ , and iterates until convergence to find  $\nabla_{\mathbf{x}}J(\mathbf{x}) = 0$ . We describe below in more detail the different components of the inversion.

The ability of the inversion to constrain methane emissions over North America is contingent on the model variability being driven by these emissions. Starting from initial conditions, we find that it takes about a week for variability of methane columns over North America in the nested model to be driven by fresh emissions and boundary conditions (as opposed to the initial conditions). We therefore initialize our simulation on 22 June, 9 days prior to assimilating the first observations on 1 July. The lifetime of methane against oxidation by OH is sufficiently long to play no significant role in the variability of methane concentrations over the North America domain.

We initially attempted to optimize North American emissions and boundary



conditions as a single state vector in the inversion. This was not successful because boundary conditions have a much larger impact in determining methane concentrations, even if they are less important for determining variability. We therefore iteratively minimize two separate cost functions,  $J(\mathbf{x}_b)$  and  $J(\mathbf{x}_e)$ , to optimize boundary concentrations and emissions, respectively:

$$J(\mathbf{x}_B) = (\mathbf{F}(\mathbf{x}_B) - \mathbf{y})^T \mathbf{S}_O^{-1} (\mathbf{F}(\mathbf{x}_B) - \mathbf{y}) + (\mathbf{x}_B - \mathbf{x}_{B,A})^T \mathbf{S}_{B,A}^{-1} (\mathbf{x}_B - \mathbf{x}_{B,A}) \quad (3.5)$$

$$J(\mathbf{x}_E) = (\mathbf{F}(\mathbf{x}_E) - \mathbf{y})^T \mathbf{S}_O^{-1} (\mathbf{F}(\mathbf{x}_E) - \mathbf{y}) + (\mathbf{x}_E - \mathbf{x}_{E,A})^T \mathbf{S}_{E,A}^{-1} (\mathbf{x}_E - \mathbf{x}_{E,A}) \quad (3.6)$$

Here the state vectors are  $\mathbf{x}_B$ , scale factors of boundary concentrations at the edge of the domain relative to the a priori, and  $\mathbf{x}_E$ , logarithms of scale factors of methane emissions relative to the a priori within the North America domain. We optimize the logarithms of the emission scale factors to ensure positivity in the optimized emissions. A priori values for  $\mathbf{x}_B$  and  $\mathbf{x}_E$  are labeled  $\mathbf{x}_{B,A}$  and  $\mathbf{x}_{E,A}$ , respectively, and the corresponding a priori error covariance matrices are  $\mathbf{S}_{B,A}$  and  $\mathbf{S}_{E,A}$ .

Each element of  $\mathbf{x}_B$  represents a temporally averaged scale factor applied to a  $4^\circ \times 5^\circ$  grid cell on the North American boundary (47 vertical levels) for a total of 3290 elements. A priori boundary concentrations are specified from the global GEOS-Chem simulation with a priori emissions (shown in figure 3.4). The a priori error covariance matrix  $\mathbf{S}_{B,A}$  is constructed using error statistics from HIPPO-GEOS-Chem comparisons over the central Pacific presented by Turner et al. (2013). The diagonal is populated with a model error standard deviation of 16 ppb (0.9%), and off-diagonal terms are parameterized with exponential error correlation length scales of 275 km in the horizontal and 78 hPa in the vertical (Wecht et al. 2012). We assume that the above error statistics apply to all four boundaries.

Each element  $x_{E,ij}$  of  $\mathbf{x}_E$  represents a temporal average applied to each  $1/2^\circ \times 2/3^\circ$  emitting grid cell  $(i,j)$  in North America for a total of 7906 elements. It is expressed as follows:

$$x_{E,ij} = \ln( E_{ij} / E_{A,ij} ) \quad (3.7)$$

where  $E_{ij}$  is the true emission flux and  $E_{A,ij}$  is the a priori described above.

The emissions a priori error covariance matrix,  $\mathbf{S}_{E,A}$  is constructed by assuming a uniform relative error standard deviation of 30% for emissions from each model grid cell and no a priori error correlations so that  $\mathbf{S}_{E,A}$  is diagonal. The sensitivity of the optimized solution to the specification of a priori error will be discussed later by considering an inversion without a priori constraints.

The observational error covariance matrix  $\mathbf{S}_O$  includes contributions from representation error, measurement error, and GEOS-Chem model error (Heald et al. 2004). Representation error is assumed to be negligible because SCIAMACHY  $X_{CH4}$  observations have horizontal footprints (30 km x 60-120 km) comparable to the size of GEOS-Chem grid cells. We use reported IMAP v5.5 values for the measurement error (standard deviation 30.2 ppb or 1.7%) since these are consistent with our INTEx-A validation (section 3.2). GEOS-Chem comparison to HIPPO vertical profiles across the Pacific indicates a model error standard deviation of 16 ppb for methane column mixing ratios and we assume that this holds for North America too. All errors are assumed to be Gaussian and are added in quadrature to calculate the observational error for each observation. We do not include error correlation between observations since the overall observational error variance is dominated by the measurement error for which no correlation is expected.

The iterative optimization works as follows. First, we perform five adjoint iterations to reduce  $J(\mathbf{x}_B)$ . We then use the updated values of  $\mathbf{x}_B$  to calculate  $J(\mathbf{x}_E)$  and perform five iterations to reduce  $J(\mathbf{x}_E)$ . We use the updated values of  $\mathbf{x}_E$  to recalculate  $J(\mathbf{x}_B)$  and repeat. When the reduction of the cost function at each iteration becomes small, after 40 iterations, we hold  $\mathbf{x}_B$  constant, and iteratively solve  $\nabla_{\mathbf{x}_E} J(\mathbf{x}_E) = 0$ . Optimization of  $\mathbf{x}_B$  corrects background methane for the inversion and is of peripheral interest here. We focus our discussion on the optimization of emissions in North America.

### 3.3.3 Clustering

Figure 3.5 shows the results from the inversion described above, with optimized correction factors of methane emissions at the  $1/2^\circ \times 2/3^\circ$  horizontal resolution of the model over North America. Optimized emissions in 93% of grid cells have inversion corrections of less than 30%, as compared to 68% of grid cells that would be expected from the a priori error. This is because the observations have insufficient information to constrain emissions at the native GEOS-Chem resolution.

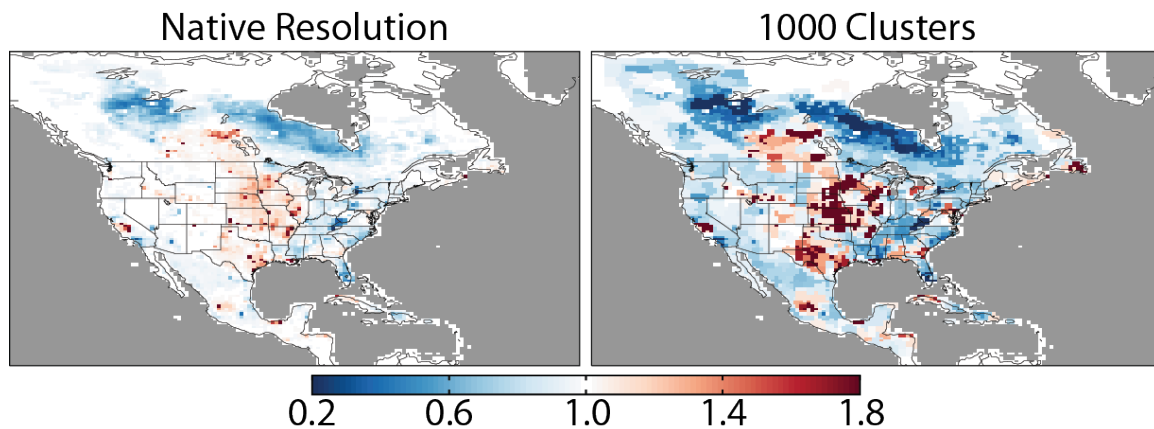


**Figure 3.5:** Emission scale factors relative to the a priori (top left panel of Figure 3.3) from inversions optimizing emissions on the  $1/2^\circ \times 2/3^\circ$  native resolution of GEOS-Chem (left) and for 1000 clustered regions (right). Gray areas (ocean/ice) are not included in the state vector for the inversion.

As the discretization of emissions becomes finer, the observations become less sensitive to emissions from each grid cell. The inversion therefore has less ability to pull emissions in each grid cell away from their a priori value, and the optimal solution will be more tightly constrained by the a priori. This can be seen quantitatively from the minimization of (3.6):

$$\nabla_{\mathbf{x}_E} J(\mathbf{x}_E) = 2(\nabla_{\mathbf{x}_E} \mathbf{F})^T \mathbf{S}_O^{-1} (\mathbf{F}(\mathbf{x}_E) - \mathbf{y}) + 2\mathbf{S}_{E,A}^{-1} (\mathbf{x}_E - \mathbf{x}_{E,A}) = 0 \quad (3.8)$$

where  $\nabla_{\mathbf{x}_E} \mathbf{F}$  is the Jacobian matrix of the forward model. As the dimension of  $\mathbf{x}_E$  increases, the Jacobian matrix values become smaller and thus the individual terms of  $(\nabla_{\mathbf{x}_E} \mathbf{F})^T \mathbf{S}_O^{-1} (\mathbf{F}(\mathbf{x}_E) - \mathbf{y})$  decrease in magnitude as  $(\nabla_{\mathbf{x}_E} \mathbf{F})^T$  distributes  $\mathbf{S}_O^{-1} (\mathbf{F}(\mathbf{x}_E) - \mathbf{y})$  over a larger number of state vector elements. By contrast, the magnitude of individual terms of  $\mathbf{S}_{E,A}^{-1} (\mathbf{x}_E - \mathbf{x}_{E,A})$  does not change. Thus the a priori increases in importance relative to the observations.

The problem could be mitigated by accurately specifying error correlations in the a priori or by imposing them in the solution, as is done in geostatistical inversions (Michalak et al., 2004). But there is little confidence to be had in the specification of error correlations for methane sources.

We opted therefore to reduce the dimension of our emission state vector by clustering of grid cells, taking advantage of the results from the native-resolution inversion (Figure 3.5) to group together neighboring grid cells with similar emission scale factors and thus minimize the aggregation error associated with clustering. We tried successively smaller numbers of clusters and repeated the inversion in the same manner described above for the native-resolution inversion, seeking to find the best number of clusters for the inversion as measured by the fit to observations. As we initially decrease

the number of clusters starting from the native resolution, , we can expect an improved fit of the inversion results to the observations for the reasons discussed above. However, as the spatial resolution of the state vector becomes too coarse (too few clusters), the fit to observations degrades because of aggregation error.

We use a hierarchical clustering algorithm (Johnson 1967) as a data-driven aggregation technique to optimally define clusters from the native resolution emissions grid. The algorithm initially assigns each  $1/2^\circ \times 2/3^\circ$  grid cell to its own region, calculates the “distance” to all other regions, and joins the two most similar. Distance is calculated as follows. We define the location for a region  $l$  by the vector  $\mathbf{v}_l = (\mathbf{p}, 0.05*s)^T$  where  $\mathbf{p}$  is the location of the region centroid on a sphere and  $s$  is the mean value of the optimized scale factor from the native resolution inversion presented in Figure 3.5. All variables are normalized to unit variance and zero mean. The factor 0.05 was selected to adjust the weight of scale factors relative to geographic distance. The distance between two regions  $l$  and  $m$  is calculated as the norm  $\|\mathbf{v}_l - \mathbf{v}_m\|$ . The process of joining the two most similar regions proceeds iteratively, reducing the number of regions by one during each step. The algorithm can be stopped at any stage so that any number of clusters can be constructed.

Figure 3.6 (black) shows the contribution of the model-observation term,  $(F(\hat{\mathbf{x}}_E) - \mathbf{y})^T \mathbf{S}_o^{-1} (F(\hat{\mathbf{x}}_E) - \mathbf{y})$ , to the optimized cost function for inversions performed using different numbers of clustered regions. Here  $\hat{\mathbf{x}}_E$  is the optimal estimate from the inversion. We do not include the a priori term since it depends on the number of clusters used. The best results are achieved for 300-1000 clusters. As the number of clusters decreases from 7906 (native resolution) to 1000, the observations become more sensitive to elements in the state vector, producing a better model fit. As the number of clusters

decreases below 300, aggregation error degrades the model fit. The range in the cost function for the different inversions is relatively small because the measurement error dominates for any individual data point. We see from Figure 3.6 that our optimal estimate for total US anthropogenic emissions is only weakly sensitive to the number of clusters used. We will use the inversion with 1000 clusters as our best estimate in terms of optimization and spatial detail.

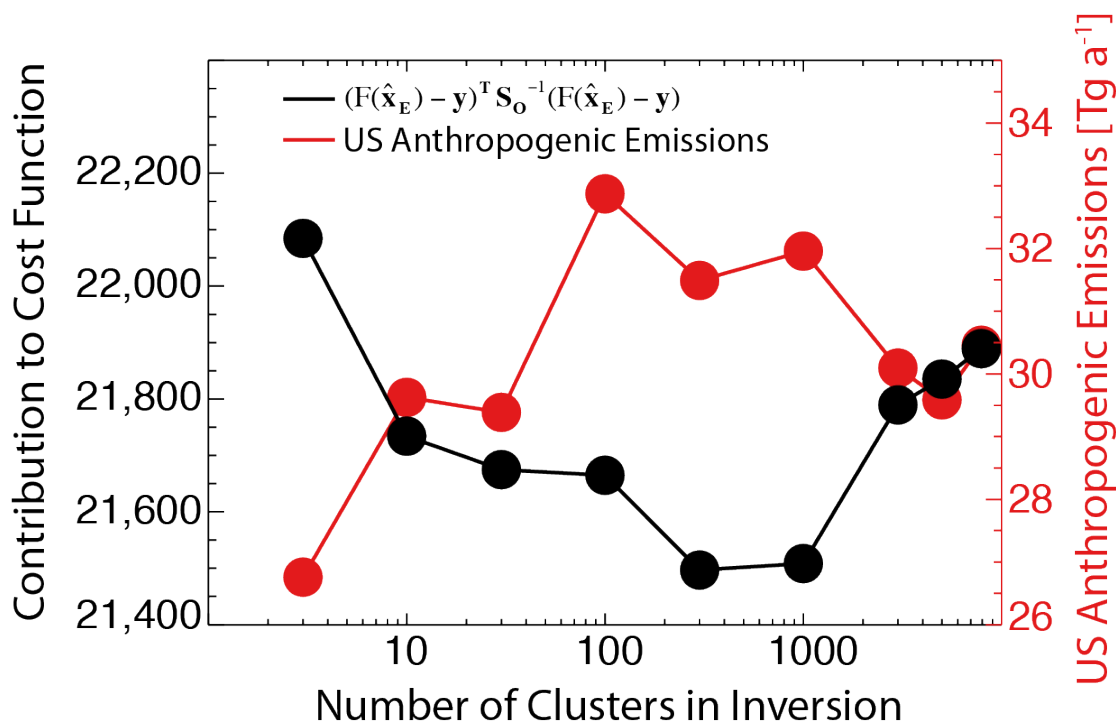


**Figure 3.6:** Sensitivity of inversion results to the resolution with which North American methane emissions are optimized from the SCIAMACHY data for 1 July – 14 August 2004. Resolution is expressed as the number of spatial clusters used in the inversion. The maximum of 7906 clusters represents the native  $1/2^\circ \times 2/3^\circ$  grid of GEOS-Chem. Optimal aggregation of grid cells based on proximity and emission correction tendencies yields successively smaller numbers of clusters. Black points show the model-observation term of the cost function  $(F(\hat{\mathbf{x}}_E) - \mathbf{y})^T \mathbf{S}_O^{-1} (F(\hat{\mathbf{x}}_E) - \mathbf{y})$  describing the ability of the cost function to fit the SCIAMACHY observations. Red points show optimized US anthropogenic emissions for each inversion.

### 3.3.4 Evaluation with SCIAMACHY and INTEx-A data

The right panel of Figure 3.5 shows the correction factors to the a priori methane emissions from the 1000-cluster inversion. Figure 3.7 shows optimized emissions, calculated as the product of optimized correction factors and prior emissions in each grid cell. We checked for improvement of the model fit to the SCIAMACHY data by comparing GEOS-Chem simulations with optimized and a priori emissions and boundary conditions. For this we calculated the GEOS-Chem – SCIAMACHY root-mean-square difference (RMSD) and correlation coefficient (R) for the ensemble of  $1/2^\circ \times 2/3^\circ$  grid cells with SCIAMACHY data, averaged over the July 1 – August 14, 2004 period and weighted by the number of SCIAMACHY observations in each grid cell. We find that the inversion reduces the model-observation RMSD from 11.6 to 9.7 ppb, while R increases from 0.65 to 0.76. This demonstrates improvement, limited by the random noise in the SCIAMACHY measurements.

We further used the boundary layer observations from INTEx-A (Figure 3.1) to provide independent verification of the inversion results. The model-observation RMSD for individual observations decreases from 33.5 to 28.5 ppb, while R increases from 0.73 to 0.74. Here the improvement appears to be limited by small-scale model and representation error for individual observations.

Averaging of the data allows us to reduce that error and is a more useful comparison. Figure 3.8 shows boundary layer ( $>850$  hPa) GEOS-Chem – INTEx-A differences averaged on an  $8^\circ \times 10^\circ$  horizontal grid and for the INTEx-A period. The resulting model-observation RMSD weighted by the number of INTEx-A observations in each  $8^\circ \times 10^\circ$  grid cell decreases 23.2 to 12.3 ppb when using optimized instead of a priori

## Optimized Emissions

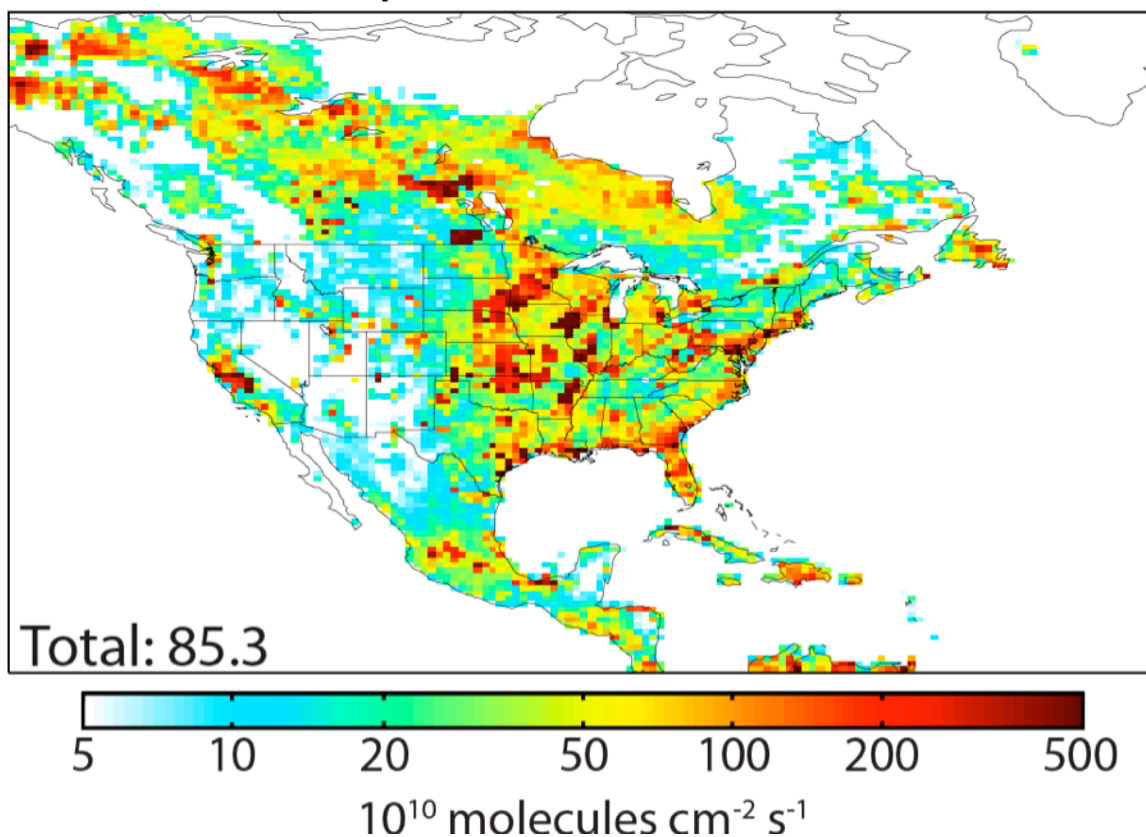


**Figure 3.7:** Optimized North American methane emissions from the 1000-cluster inversion. The annual emission rate for 2004 ( $\text{Tg a}^{-1}$ ) is shown inset for the North America domain as encompassed by the figure.

emissions. The correlation coefficient  $R$  increases from 0.69 to 0.88.

We performed sensitivity inversions to investigate the effects of a priori constraints on emissions and model bias. A native-resolution inversion without a priori constraints on emissions shows similar signs and patterns of emission corrections to the inversion with a priori constraints, but the magnitudes of corrections are larger.

Evaluation using INTEX-A data averaged into  $8^\circ \times 10^\circ$  regions as above does not show as good a fit to observations, with an RMSD of 14.5 ppb and  $R$  of 0.77. This indicates that



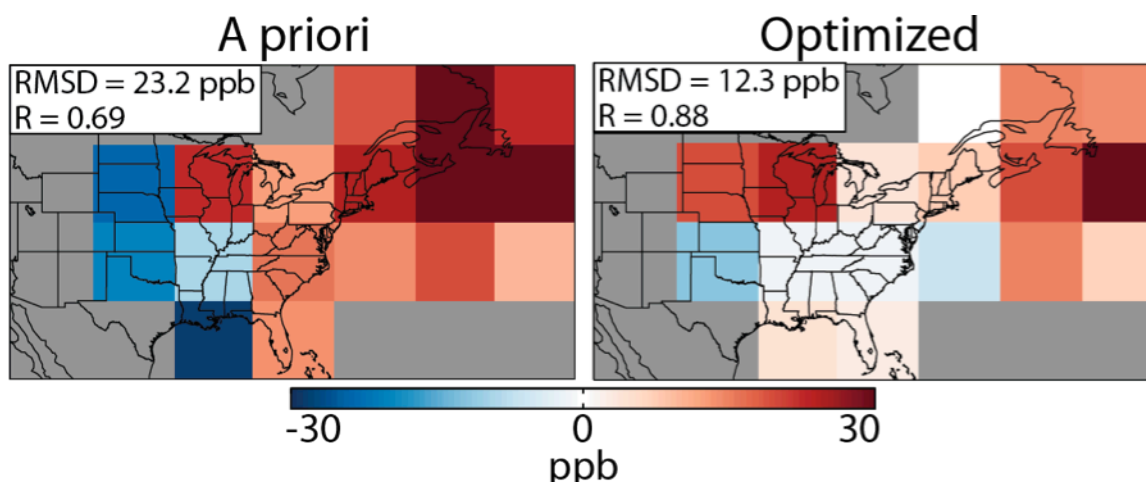


**Figure 3.8:** Independent evaluation of the SCIAMACHY inversion of methane emissions using INTEx-A aircraft data. The panels show the mean differences between GEOS-Chem and INTEx-A observations below 850 hPa and for  $8^\circ \times 10^\circ$  grid squares in the simulation with a priori emissions (left) and with optimized emissions from the 1000-cluster inversion (right). A priori and optimized emission maps are shown in Figures 3.2 and 3.7. The model-observation root mean square difference (RMSD) and weighted correlation coefficient (R) are inset.

the a priori inventory contributes useful information. A sensitivity inversion including a uniform positive bias correction of 15 ppb in GEOS-Chem on the basis of INTEx-A free tropospheric data shows negligible effect on the correction factors to emissions because most of the bias is absorbed by correction to the boundary conditions.

### 3.4 Optimized Methane Emissions

The optimized correction factors in Figure 3.5 show patterns of increases and decreases relative to the a priori emissions in Figure 3.3. There is a large decrease in emissions from natural wetlands in northern Ontario and western Canada. There is also a broad decrease in the eastern US, particularly in Appalachia, suggesting an overestimate of emissions from coal mining and waste management. Emissions in the central US

increase, suggesting an underestimate of livestock emissions and also possibly from natural gas and oil extraction. We elaborate on source attribution below.

Table 3.1 shows US anthropogenic emission estimates from EPA, EDGAR v4.2, and this work. Optimized US anthropogenic emissions are  $32.0 \pm 1.3 \text{ Tg a}^{-1}$ , where our best estimate is from the 1000-cluster inversion and our error standard deviation is from the ensemble of inversions with different numbers of clusters in Figure 3.6 excluding the 3-cluster inversion. Our best estimate is 24% higher than EDGAR v4.2, and 13% higher than EPA (2013), within the stated EPA 95% confidence interval of 14%.

Our inversion optimizes the geographic distribution of emissions without a priori information on source type. It is of interest to determine whether the corrections can be attributed to the particular source types of Figure 3.3. To do so, we multiply the optimized emission correction factors by the a priori source estimates for each source type and grid cell. This approach assumes that the relative a priori source distribution in each grid cell is correct. It does not assume that a priori spatial distributions of sources are correct because spatial patterns will change after applying the correction factors. We estimate uncertainties on the basis of the ensemble of values for the inversions with different clusters, recognizing that they are likely underestimates as all inversions make the same assumption about correctness of the a priori source distribution.

Results in Table 3.1 show that our emission estimate for livestock is 60% higher than the EDGAR v4.2 and EPA inventories and represents the largest US source. Our gas/oil source is intermediate between EDGAR v4.2 and EPA and is only half of the livestock source. Other sources are smaller, across all inventories. Our landfills source is consistent with both EDGAR v4.2 and EPA while our coal mining source is smaller than

EDGAR v4.2 but consistent with EPA.

However, the patterns of correction factors from our inversion in Figure 3.5 reveal structure that cannot be simply explained by the EDGAR v4.2 source types. A multiple linear regression of absolute corrections on the distributions of individual EDGARv4.2 and natural a priori emissions yields an  $R^2$  of only 0.21. For example, our correction factors in Figure 3.5 indicate a large EDGAR underestimate of livestock emissions in Iowa, where hog manure is important, but a decrease in eastern North Carolina where hog manure is important too. This could reflect differences in manure management practices. Our inversion also calls for a large increase in emissions from the Permian Basin in western Texas, a major gas/oil production region, but the EDGAR v4.2 inventory is very low there. This suggests that gas/oil emissions in EDGAR are too heavily weighted by the distribution and end use sectors relative to the production sector.

### **3.5 Comparison to previous studies**

A number of previous studies have used methane observations from surface sites and aircraft as top-down constraints on methane emissions in North America. We discuss here the consistency of our results.

There has been much interest in quantifying wetland emissions from in the Hudson Bay Lowlands (HBL) of northern Ontario, as this is the second largest area of boreal wetlands in the world after western Siberia. Pickett-Heaps et al. (2011) reviewed previous studies and estimated an HBL source of  $2.3 \text{ Tg a}^{-1}$  from aircraft and surface observations. Miller et al. (2013b) estimated a source of  $2.4 \text{ Tg a}^{-1}$  using tall tower observations. We find here a consistent estimate of  $2.1 \text{ Tg a}^{-1}$ , accounting for the

seasonality given by Pickett-Heaps et al. (2011) with strong peak in June-August. This calls for downward revision of the Kaplan et al. (2002) source used as a priori in GEOS-Chem.

The CalNex aircraft campaign in May-June 2010 provided constraints on methane emissions from California through a series of boundary layer flights across the state. Inverse analyses of the CalNex data by Santoni et al. (submitted) and Wecht et al. (in prep) indicate statewide emissions of 2.4-2.8 Tg a<sup>-1</sup>, Los Angeles Basin emissions of 0.3-0.4 Tg a<sup>-1</sup>, and a factor of 2-4 underestimate of livestock emissions in the EDGAR v4.2 inventory for the Central Valley. Our inversion of the SCIAMACHY data is closely consistent with these results indicating a statewide emission of 2.1 Tg a<sup>-1</sup> in California, 0.2 Tg a<sup>-1</sup> in the Los Angeles Basin, and a factor of 2.6 underestimate in livestock emissions relative to EDGAR v4.2. The livestock underestimate is larger for California than the national underestimate of 60% reported earlier, and provides further evidence of spatial errors in emission factors in the EDGAR inventory.

Miller et al. (2013a) estimated methane emissions across the US using a network of surface and aircraft data from 2007-2008. Their optimal estimate for US anthropogenic emissions is 44.5 Tg a<sup>-1</sup>, much higher than our value of 32.0 Tg a<sup>-1</sup>. They increase emissions in the central US relative to EDGAR and decrease emissions in Appalachia, similar to the spatial patterns reported here. Their observations, however, are relatively sparse east of the Great Plains and may not adequately characterize the emissions reductions throughout Appalachia and the northeast that are required by SCIAMACHY and consistent with the INTEx-A data. Miller et al. (2013a) estimate a factor of 2.3 increase relative to EDGAR v4.2 for the northern plains (Nebraska, Iowa, Wisconsin,

Minnesota, and South Dakota), a region of high livestock density and few other sources of methane. This compares well to our factor of 2.5 increase for the region, again higher than the national average for livestock emissions.

Katzenstein et al. (2003) measured methane concentrations on a road survey across Texas, Oklahoma, and Kansas. Assuming a mean boundary layer height and a characteristic ventilation time for the region, they estimated a methane emission of 4-6  $\text{Tg a}^{-1}$  for that tri-state region. Assuming that these emissions are mainly from natural gas and oil, they concluded that EPA emission estimates are too low by a factor of 2.5. Our inversion indicates a methane emission of 9.4  $\text{Tg a}^{-1}$  for the region, greater than the Katzenstein et al. (2003) estimate and possibly reflecting their oversimplified ventilation model. In any case, their assumption that gas/oil dominate sources in the region may not be valid as the EDGAR v4.2 inventory for the region (4.0  $\text{Tg a}^{-1}$ ) assigns 52% of methane emissions to livestock and only 29% to gas/oil. Miller et al. (2013a) estimate emissions of 10.8  $\text{Tg a}^{-1}$  for the region and attribute the underestimate to both livestock and gas/oil. Most of the emission correction for the region in our inversion is from livestock.

Xiao et al. (2008) derived a US ethane emission of 2.4  $\text{Tg a}^{-1}$  from analysis of INTEX-A observations and combined this with independent estimates of ethane-to-methane emission ratios to deduce a US fossil fuel methane emission of 16  $\text{Tg a}^{-1}$ . This would include contributions from natural gas, oil, and coal mining. By comparison, EPA and EDGAR v4.2 estimate US fossil fuel emissions of 11.7 and 10.1  $\text{Tg a}^{-1}$ , respectively. Using the source-type distributions provided by EDGAR, we calculate a fossil fuel methane source of 9.6  $\text{Tg a}^{-1}$ . Uncertainty on ethane-to-methane emission ratios may have affected the Xiao et al. (2008) estimate.

Kort et al. (2008) used Lagrangian modeling of observations from the COBRA-NA aircraft campaign across North America in 2003 to evaluate US and Canada emissions. From a single linear regression of modeled vs. observed methane they estimated US anthropogenic emissions of  $41 \pm 6 \text{ Tg a}^{-1}$ , larger than our best estimate of  $32.0 \text{ Tg a}^{-1}$ . Their observations, however, are only sensitive to emissions from a relatively small fraction of the US and Canada.

Petron et al. (2012) and Karion et al. (2013) used in situ observations to estimate methane leak rates of 4% and 6-12% of total natural gas production Weld County, CO and Uintah County, UT, respectively. In contrast, the EDGAR v4.2 and EPA inventories assume a national average leak rate of 1.0-1.4%. Our inversion of the SCIAMACHY data does not indicate higher-than-expected natural gas emissions from these two counties but this would not account for post-2004 growth. Methane leakage rates can vary considerably by basin (US Government Accountability Office, 2010).

### **3.6 Conclusions**

We used SCIAMACHY satellite observations in a high-resolution continental-scale inversion of methane emissions in North America driven by the GEOS-Chem chemical transport model (CTM) and its adjoint at  $1/2^\circ \times 2/3^\circ$  horizontal resolution. The inversion focused on summer 2004, when concurrent observations from the INTEx-A aircraft observations are available to both validate the SCIAMACHY data and independently evaluate the inversion. The high density of observations available from SCIAMACHY enables higher spatial detail in constraining methane emissions on the continental scale than had been achievable before.

Removal of observational bias is essential for a successful inversion. Our validation of the SCIAMACHY observations (IMAP v5.5) with INTEx-A vertical profiles identified a systematic bias correlated with water vapor, consistent with previous studies. We found that we could successfully correct for this bias, and the residual error is consistent with the theoretical error estimate from the IMAP v5.5 retrieval.

Continental-scale inversion for methane required accurate specification of the boundary conditions in GEOS-Chem. This was accomplished by optimizing both the North American emissions and the boundary conditions as part of the inversion. We found that the information content from the SCIAMACHY data was insufficient to constrain emissions at the native  $1/2^\circ \times 2/3^\circ$  horizontal resolution of GEOS-Chem. We solved this problem by using a hierarchical clustering algorithm to identify 1000 geographical clusters for which the inversion provides optimal results. The optimized emissions obtained from the 1000-cluster inversion were independently evaluated by GEOS-Chem simulation of the INTEx-A aircraft data. This demonstrated a major improvement over the simulation driven by a priori emissions.

Our optimized methane emissions for the Canadian wetlands are lower than the a priori but consistent with recent studies. Our optimized methane emissions for the US are lower than the EDGAR v4.2 inventory for the eastern US but higher for the central US. Our best estimate of US anthropogenic emissions is  $32.0 \pm 1.3 \text{ Tg a}^{-1}$ , compared to  $25.8 \text{ Tg a}^{-1}$  and  $28.3 \text{ Tg a}^{-1}$  in the EDGAR v4.2 and EPA inventories respectively. Source attribution of our optimized methane emissions on the basis of the EDGAR patterns suggests that the above inventories underestimate livestock emissions by 60-70%, with smaller discrepancies for other sources. We find that livestock emissions in the US are

twice higher than gas/oil emissions, whereas the EPA inventory reports these two sources to be of comparable magnitude. However, we find in a regression analysis that the EDGAR patterns can account for only 21% of the variability in the source correction from the inversion. This implies large inventory errors in the geographic variability of emission factors (e.g., livestock management practices) and activity rates (e.g., gas/oil production in the West).

Our finding that US livestock emissions are underestimated in current inventories is consistent with previous regional studies. The degree of underestimate seems highly variable for different parts of the country, suggesting large variability in emission factors. Our finding that gas/oil emissions are not underestimated in current inventories is at odds with previous studies and may partly reflect assumptions in these studies and local variability in leakage rates.

Emissions of methane in North America may be rapidly changing in the future as a result of increasing gas/oil production, changes in recovery practices, hydrofracking, and climate change affecting wetlands. The GOSAT satellite observations (2009-present) may be useful to track recent trends but are relatively sparse. The TROPOMI instrument to be launched in 2015 will provide global daily coverage with  $7 \times 7 \text{ km}^2$  nadir spatial resolution and precision of 0.6% (Veefkind et al. 2012; Butz et al. 2012). This will provide a tremendous boost to monitoring methane emissions from space.

## **Acknowledgments**

This work was supported by the NASA Carbon Monitoring System (CMS), the NASA Atmospheric Composition Modeling and Analysis Program (ACMAP) and by a NASA



Earth System Science Fellowship to KJW.

## References

- Allen, D., K. Pickering, B. Duncan, and M. Damon (2010), Impact of lightning NO emissions on North American photochemistry as determined using the Global Modeling Initiative (GMI) model, *J. Geophys. Res.*, 115, D22301, doi:10.1029/2010JD014062.
- Bergamaschi, P., Frankenberg, C., Meirink, J. F., Krol, M., Den- tener, F., Wagner, T., Platt, U., Kaplan, J. O., Korner, S., Heimann, M., Dlugokencky, E. J. and Goede A.: Satellite chartography of atmospheric methane from SCIAMACHY on board ENVISAT: 2. Evaluation based on inverse model simulations, *J. Geophys. Res.*, 112, D02304, doi:10.1029/2006JD007268, 2007.
- Bergamaschi, P., Frankenberg, C., Meirink, J. F., Krol, M., Villani, M. G., Houweling, S., Dentener, F., Dlugokencky, E. J., Miller, J. B., Gatti, L. V., Engel, A. and Levin I.: Inverse modeling of global and regional CH<sub>4</sub> emissions using SCIAMACHY satellite retrievals, *J. Geophys. Res.*, 114, D22301, doi:10.1029/2009JD012287, 2009.
- Bergamaschi, P., Houweling, S., Segers, A., Krol, M., Frankenberg, C., Scheepmaker, R.A., Dlugokencky, E., Wofsy, S.C., Kort, E.A., Sweeney, C., Schuck, T., Brenninkmeijer, C., Chen, H., Beck, V., and Gerbig, C., Atmospheric CH<sub>4</sub> in the first decade of the 21st century: Inverse modeling analysis using SCIAMACHY satellite retrievals and NOAA surface measurements, *J. Geophys. Res. Atmos.*, 118, 7350–7369, doi:10.1002/jgrd.50480, 2013.
- Bocquet, M., Grid resolution dependence in the reconstruction of an atmospheric tracer source, *Nonlinear Processes Geophys.*, 12, 219-234, 2005.
- Bocquet, M., Toward optimal choices of control space representation for geophysical data assimilation, *Mon. Weather Rev.*, 137, 2331-2348, 2009.
- Bocquet, M., Wu, L., and Chevallier, F., Bayesian design of control space for optimal assimilation of observations. Part I: Consistent multiscale formalism, *Q. J. R. Meteorol. Soc.* 137: 1340-1356. DOI:10.1002/qj.837, 2011.
- Butz, A., Galli, A., Hasekamp, O., Landgraf, J., Tol, P., and Aben, I.: TROPOMI aboard Precursor Sentinel-5 Precursor: Prospective performance of CH<sub>4</sub> retrievals for aerosol and cirrus loaded atmospheres, *Remote Sens. Environ.*, 120, 267–276, doi:10.1016/j.rse.2011.05.030, 2012.
- Considine, D. B., J. A. Logan, and M. A. Olsen (2008), Evaluation of near-tropopause ozone distributions in the Global Modeling Initiative combined stratosphere/troposphere model with ozonesonde data, *Atmos. Chem. Phys.*, 8(9), 2365–2385, doi:10.5194/acp-8-2365-2008.
- Cressot, C., Chevallier, F., Bousquet, P., Crevoisier, C., Dlugokencky, E.J., Fortems-

Cheiney, A., Frankenberg, C., Parker, R., Pison, I., Scheepmaker, R.A., Montzka, A.A., Krummel, P.B., Steele, L.P., and Langenfelds, R.L., On the consistency between global and regional methane emissions inferred from SCIAMACHY, TANSO-FTS, IASI and surface measurements, *Atmos. Chem. Phys. Discuss.*, 13, 8023-8064, 2013.

Crevoisier, C., Nobileau, D., Armante, R., Crépeau, L., Machida, T., Sawa, Y., Matsueda, H., Schuck, T., Thonat, T., Pernin, J., Scott, N. A., and Chédin, A.: The 2007–2011 evolution of tropical methane in the mid-troposphere as seen from space by MetOp-A/IASI, *Atmos. Chem. Phys.*, 13, 4279–4289, doi:10.5194/acp-13-4279-2013, 2013.

Dils, B., De Mazière, M., Muller, J. F., Blumenstock, T., Buchwitz, M., de Beek, R., Demoulin, P., Duchatelet, P., Fast, H., Frankenberg, C., Gloudemans, A., Griffith, D., Jones, N., Kerzenmacher, T., Kramer, I., Mahieu, E., Mellqvist, J., Mittermeier, R. L., Notholt, J., Rinsland, C. P., Schrijver, H., Smale, D., Strandberg, A., Straume, A. G., Stremme, W., Strong, K., Susmann, R., Taylor, J., van den Broek, M., Velasco, V., Wagner, T., Warneke, T., Wiacek, A., and Wood, S.: Comparisons between SCIAMACHY and ground-based FTIR data for total columns of CO, CH<sub>4</sub>, CO<sub>2</sub> and N<sub>2</sub>O, *Atmos. Chem. Phys.*, 6, 1953–1976, doi:10.5194/acp-6-1953-2006, 2006.

European Commission, Joint Research Centre (JRC)/Netherlands Environmental Assessment Agency (PBL). Emission Database for Global Atmospheric Research (EDGAR), release version 4.0. <http://edgar.jrc.ec.europa.eu>, 2009.

Frankenberg, C., Meirink, J. F., Bergamaschi, P., Goede, A. P. H., Heimann, M., Konner, S., Platt, U., van Weele, M., and Wagner, T.: Satellite cartography of atmospheric methane from SCIAMACHY on board ENVISAT: Analysis of the years 2003 and 2004, *J. Geophys. Res.*, 111, D07303, doi:10.1029/2005JD006235, 2006.

Frankenberg, C., P. Bergamaschi, A. Butz, S. Houweling, J. F. Meirink, J. Notholt, A. K. Petersen, H. Schrijver, T. Warneke, and I. Aben, Tropical methane emissions: A revised view from SCIAMACHY onboard ENVISAT, *Geophys. Res. Lett.*, 35, L15811, doi:10.1029/2008GL034300, 2008.

Frankenberg, C., Aben, I., Bergamaschi, P., Dlugokencky, E. J., van Hees, R., Houweling, S., van der Meer, P., Snel, R. and Tol, P.: Global column-averaged methane mixing ratios from 2003 to 2009 as derived from SCIAMACHY: Trends and variability, *J. Geophys. Res.*, 116, D02304, doi:10.1029/2010JD014849, 2011.

Fung, I., John, J., Lerner, J., Matthews, E., Prather, M., Steele, L. P., and Fraser, P. J.: Three-dimensional model synthesis of the global methane cycle, *J. Geophys. Res.*, 96, 13 033–13 065, 1991.

Hartmann, D.L., Klein Tank, A.M.G., Rusticucci, M., Alexander, L., Broennimann, S., Charabi, Y.A.-R., Dentener, F., Dlugokencky, E., Easterling, D., Kaplan, A., Soden, B., Thorne, P., Wild, M., and Zhai, P., Climate Change 2013: The Physical Science Basis, Working Group I Contribution to the IPCC Fifth Assessment Report (AR5), Final Draft,

chap. Observations: Atmosphere and Surface, <http://www.ipcc.ch/report/aar5/wg1/>, 2013.

Heald, C., Jacob, D., Jones, D., Palmer, P., Logan, J., Streets, D., Sachse, G., Gille, J., Hoffman, R. and Nehrkorn, T.: Comparative inverse analysis of satellite (MOPITT) and aircraft (TRACE-P) observations to estimate Asian sources of carbon monoxide, *J Geophys Res-Atmos*, 109(D23), D23306, doi:10.1029/2004JD005185, 2004.

Henze, D. K., Hakami, A., and Seinfeld, J. H.: Development of the adjoint of GEOS-Chem, *Atmos Chem Phys*, 7, 2413-2433, 2007.

Houweling, S., Krol, M., Bergamaschi, P., Frankenberg, C., Dlugokencky, E.J., Morino, I., Notholt, J., Sherlock, V., Wunch, D., Beck, V., Gerbig, C., Chen, H., Kort, E.A., Röckmann, T., and I. Aben, I., A multi-year methane inversion using SCIAMACHY, accounting for systematic errors using TCCON measurements, *Atmos. Chem. Phys. Discuss.*, 13, 28117-28171, 2013.

Johnson, S. (1967), Hierarchical clustering schemes, *Psychometrika*, 32(3), 241–254, doi:10.1007/BF02289588.

Kaplan, J. O.: Wetlands at the Last Glacial Maximum: Distribution and methane emissions, *Geophys. Res. Lett.*, 29(6), 1079, doi:10.1029/2001GL013366, 2002.

Karion, A., Sweeney, C., Pétron, G., Frost, G., Hardesty, R.M., Kofler, J., Miller, B.R., Newberger, T., Wolter, S., Banta, R., Brewer, A., Dlugokencky, E., Lang, P., Montzka, S.A., Schnell, R., Tans, P., Trainer, M., Zamora, R., and Conley, S., Methane emissions estimate from airborne measurements over a western United States natural gas field, *Geophys. Res. Lett.*, 40, 4393–4397, doi:10.1002/grl.50811, 2013.

Katzenstein, A. S., Doezeema, L.A., Simpson, I.J., Blake D.R., and Rowland, F.S., Extensive regional atmospheric hydrocarbon pollution in the southwestern United States, *Proc. Natl. Acad. Sci. U.S.A.*, 100(21), 11,975 – 11,979, 2003.

Kort, E.A., Eluszkiewicz, J., Stephens, B.B., Miller, J.B., Gerbig, C., Nehrkorn, T., Daube, B.C., Kaplan, J.O., Houweling, S., Wofsy, S.C., Emissions of CH<sub>4</sub> and N<sub>2</sub>O over the United States and Canada based on a receptor-oriented modeling framework and COBRA-NA atmospheric observations, *Geophys. Res. Lett.*, 35, L18808, doi:10.1029/2008GL034031, 2008.

Meirink, J. F., et al., Four-dimensional variational data assimilation for inverse modeling of atmospheric methane emissions: Analysis of SCIAMACHY observations, *J. Geophys. Res.*, 113, D17301, doi:10.1029/2007JD009740, 2008.

Miller, S.M., Wofsy, S.C., Michalak, A.M., Kort, E.A., Andrews, A.E., Biraud, S.C., Dlugocencky, E.J., Eluskiewicz, J., Fisher, M.L., Janssens-Maenhout, G., Miller, B.R., Miller, J.B., Montzka, S.A., Nehrkorn, T., and Sweeney, C., Anthropogenic emissions of methane in the US, *Proc. Natl. Acad. Sci. U.S.A.*, submitted (2013a).

Miller, S.M., Worthy, D.E.J., Michalak, A.M., Wofsy, S.C., Kort, E.A., Havice, T.C., Andrews, A.E., Biraud, S.C., Dlugocencky, Levi, P.J., Kaplan, J.O., Tian, H., and Zhang, B., Observational constraints on the distribution, seasonality, and environmental predictors of North American boreal methane emissions, *Global Biogeochemical Cycles*, submitted (2013b).

Monteil, G., Houweling, S., Butz, A., Guerlet, S., Schepers, D., Hasekamp, O., Frankenberg, C., Scheepmaker, R., Aben, I., and Röckmann, T., Comparison of CH<sub>4</sub> inversions based on 15 months of GOSAT and SCIAMACHY observations, *J. Geophys. Res. Atmos.*, 118, doi:10.1002/2013JD019760, 2013.

Mu, M., J.T. Randerson, G.R. van der Werf, L. Giglio, P. Kasibhatla, D. Morton, G.J. Collatz, R.S. DeFries, E.J. Hyer, E.M. Prins, D.W.T. Griffith, D. Wunch, G.C. Toon, V. Sherlock, and P.O. Wennberg. Daily and 3-hourly variability in global fire emissions and consequences for atmospheric model predictions of carbon monoxide. *Journal of Geophysical Research-Atmospheres*. 116: D24303. doi:10.1029/2011JD016245, 2010.

Murray, L. T., Jacob, D.J., Logan, J.A., Hudman, R.C., and Koshak, W.J., Optimized regional and interannual variability of lightning in a global chemical transport model constrained by LIS/OTD satellite data, *J. Geophys. Res.*, 117, D20307, doi:10.1029/2012JD017934, 2012.

Myhre, G., Shindell, D., Breon, F.-M., Collins, B., Fuglestad, J., Huang, J., Koch, D., Lamarque, J.-F., Lee, D., Mendoza, B., Nakajima, T., Robock, A., Stephens, Graeme, Takemura, T., and Zhang, H., *Climate Change 2013: The Physical Science Basis. Working Group I Contribution to the IPCC Fifth Assessment Report (AR5), Final Draft*, chap. Anthropogenic and Natural Radiative Forcing, <http://www.ipcc.ch/report/ar5/wg1/>, 2013.

Park, R. J., Jacob, D.J., Field, B. D., Yantosca, R.M., and Chin, M., Natural and transboundary pollution influences on sulfate-nitrate-ammonium aerosols in the United States: implications for policy, *J. Geophys. Res.*, 109, D15204, 10.1029/2003JD004473, 2004.

Park, R. J., Jacob, D. J., Kumar, N., and Yantosca, R.M., Regional visibility statistics in the United States: Natural and transboundary pollution influences, and implications for the Regional Haze Rule, *Atmos. Environ.*, 40(28), 5405-5423, 2006.

Parker, R., Boesch, H., Cogan, A., Fraser, A., Feng, L., Palmer, P. I., Messerschmidt, J., Deutscher, N., Griffith, D. W., Notholt, J., Wennberg, P. O., and Wunch, D.: Methane observations from the Greenhouse Gases Observing SATellite: Comparison to ground-based TCCON data and model calculations, *Geophys. Res. Lett.*, 38, L15807, doi:10.1029/2011GL047871, 2011.

Pétron, G., Frost, G., Miller, B.R., Hirsch, A.I., Montzka, S.A., Karion, A., Trainer, M., Sweeney, C., Andrews, A.E., Miller, L., Kofler, J., Bar-Ilan, A., Dlugokencky, E.J.,

Patrick, L., Moore Jr., C.T., Ryerson, T.B., Siso, C., Kolodzey, W., Lang, P.M., Conway, T., Novelli, P., Masarie, K., Hall, B., Guenther, D., Kitzis, D., Miller, J., Welsh, D., Wolfe, D., Neff, W., and Tans, P., Hydrocarbon emissions characterization in the Colorado Front Range: A pilot study, *J. Geophys. Res.*, 117, D04304, doi:10.1029/2011JD016360, 2012.

Pickett-Heaps, C. A., Jacob, D. J., Wecht, K. J., Kort, E. A., Wofsy, S. C., Diskin, G. S., Worthy, D. E. J., Kaplan, J. O., Bey, I. and Drevet, J.: Magnitude of seasonality of wetland methane emissions from the Hudson Bay Lowlands (Canada), *Atmos Chem Phys*, 11(8), 3773-3779, 2011.

Prather, M. J., Holmes, C. D., and Hsu, J.: Reactive greenhouse gas scenarios: Systematic exploration of uncertainties and the role of atmospheric chemistry, *Geophys. Res. Lett.*, 39, L09803, doi:10.1029/2012GL051440, 2012.

Rodgers, C.D.: *Inverse Methods for Atmospheric Sounding*, World Scientific Publishing Co. Pte. Ltd, Tokyo 2000.

Santoni, G.W., Xiang, B., Kort, E.A., Daubel, B.C., Andrews, A.E., Sweeney, C., Wecht, K.J., Peischl, J., Ryerson, T.B., Angevine, W.M., Trainer, M., Nehrkorn, T., Eluszkiewicz, J., Jeong, S., Fischer, M.L., Ferrare, R.A., and Wofsy, S.C., California's methane budget derived from CalNex P-3 Aircraft Observations and a Lagrangian transport model, *J. Geophys. Res.*, submitted.

Schepers, D., Guerlet, S., Butz, A., Landgraf, J., Frankenberg, C., Hasekamp, O., Blavier, J.-F., Deutscher, N.M., Griffith, D.W.T., Hase, F., Kyro, E., Morino, I., Sherlock, V., Sussmann, R., and Aben, I., Methane retrievals from Greenhouse Gases Observing Satellite (GOSAT) shortwave infrared measurements: Performance comparison of proxy and physics retrieval algorithms, *J. Geophys. Res.*, 117, D10307, doi:10.1029/2012JD017549, 2012.

Singh, H.B., Brune, W.H., Crawford J.H., and Jacob, D.J., Overview of the summer 2004 Intercontinental Chemical Transport Experiment-North America (INTEX-A), *J. Geophys. Res.*, 111, D24S01, doi:10.1029/2006JD007905, 2006.

Turner, A.J., Jacob, D.J., Wecht, K.J., Sulprizio, M., Payne, V., Santoni, G., Wofsy, S.C., Bowman, K.W., Parker, R., Boesch, H., Optimal estimation of North American methane emissions using GOSAT data: A contribution to the NASA Carbon Monitoring System, American Geophysical Union Fall 2013 Meeting.

United States Environmental Protection Agency (EPA). *Inventory of U.S. Greenhouse Gas Emissions and Sinks: 1990-2011-Annexes*, 2013.  
<http://www.epa.gov/climatechange/Downloads/ghgemissions/US-GHG-Inventory-2013-Main-Text.pdf>

United States Government Accountability Office (GAO), *Federal Oil and Gas Leases: Opportunities exist to capture vented and flared natural gas, which would increase royalty*

payments and reduce greenhouses gases, Washington DC, 2010.

van der Werf, G. R., Randerson, J. T., Giglio, L., Collatz, G. J., Mu, M., Kasibhatla, P. S., Morton, D. C., DeFries, R. S., Jin, Y., and van Leeuwen, T. T.: Global fire emissions and the contribution of deforestation, savanna, forest, agricultural, and peat fires (1997–2009), *Atmos. Chem. Phys.*, 10, 11707–11735, doi:10.5194/acp-10-11707-2010, 2010.

Van Donkelaar, A., Martin, R.V., Pasch, A.N., Szykman, J.J., Zhang, L., Wang, Y.X., and Chen, D., Improving the Accuracy of Daily Satellite-Derived Ground-Level Fine Aerosol Concentration Estimates for North America, *Environmental Science and Technology*, 46, 21, 11971–11978, 2012.

van Vuuren, D.P., Stehfest, E., den Elzen, M.G.J., van Vliet, J., and Isaac, M., Exploring IMAGE model scenarios that keep greenhouse gas radiative forcing below 3 W/m<sup>2</sup> in 2100, *Energy Economics* 32, 1105–1120, 2010.

Veefkind, J.P., Aben, I., McMullan, K., Forster, H., de Vries, J., Otter, G., Claas, J., Eskes, H.J., de Haan, J.F., Kleipool, Q., van Weele, M., Hasekamp, O., Hoogeveen, R., Landgraf, J., Snel, R., Tol, P., Ingmann, P., Voors, R., Kruizinga, B., Vink, R., Visser, H., and Levelt, P.F., TROPOMI on the ESA Sentinel-5 Precursor: A GMES mission for global observations of the atmospheric composition for climate, air quality and ozone layer applications, *Remote Sensing of Environment* 120, 70–83, 2012.

Voulgarakis, A., Naik, V., Lamarque, J.-F., Shindell, D.T., Young, P.J., Prather, M.J., Wild, O., Field, R.D., Bergmann, D., Cameron-Smith, P., Cionni, I., Collins, W.J., Dalsoren, S.B., Doherty, R.M., Eyring, V., Faluvegi, G., Folberth, G.A., Horowitz, L.W., Josse, B., MacKenzie, I.A., Nagashima, T., Plummer, D.A., Righi, M., Rumbold, S.T., Stevenson, D.S., Strode, S.A., Sudo, K., Szopa, S., and Zeng, G., Analysis of present day and future OH and methane lifetime in the ACCMIP simulations, *Atmos. Chem. Phys.*, 13, 2563–2587, 2013.

Wang, J.S., Logan, J.L., McElroy, M.B., Duncan, B.N., Megretskaia, I.A., and Yantosca, R.M., A 3-D model analysis of the slowdown and interannual variability in the methane growth rate from 1988 to 1997, *Global Biogeochemical Cycles*, 18, GB3011, doi:10.1029/2003GB002180, 2004.

Wecht, K.J., Jacob, D.J., Wofsy, S.C., Kort, E.A., Worden, J.R., Kulawik, S.S., Henze, D.K., Kopacz, M., and Payne, V.H., Validation of TES methane with HIPPO aircraft observations: implications for inverse modeling of methane sources, *Atmos. Chem. Phys.*, 12, 1823–1832, 2012.

Wecht, K.J., Jacob, D.J., Sulprizio, M.P., Santoni, G.W., Wofsy, S.C., Parker, R., and Worden, J.R., Spatially resolving methane emissions in California: constraints from the CalNex aircraft campaign and from present (GOSAT, TES) and future (TROPOMI, GEO-CAPE) satellite observations, in prep.



Weyant, J.P., de la Chesnaye, F.C., and Blanford, G.J., Overview of EMF-21: Multigas Mitigation Climate Policy, *The Energy Journal*, Multi-Greenhouse Gas Mitigation and Climate Policy Special Issue, 2006.

Wofsy, S. C., the HIPPO Science Team and Cooperating Modelers and Satellite Teams: HIAPER Pole-to-Pole Observations (HIPPO): fine-grained, global-scale measurements of climatically important atmospheric gases and aerosols, *Philosophical Transactions of the Royal Society A: Mathematical, Physical and Engineering Sciences*, 369(1943), 2073–2086, doi:10.1098/rsta.2010.0313, 2011.

Worden, J., Kulawik, S., Frankenberg, C., Bowman, K., Payne, V., Cady-Peirara, K., Wecht, K., Lee, J-E., Noone, D., Risi, C.: Profiles of CH<sub>4</sub>, HDO, H<sub>2</sub>O, and N<sub>2</sub>O with improved lower tropospheric vertical resolution from Aura TES radiances, *Atmos. Meas. Tech. Discuss.*, 4, 6679-6721, 2012.

World Energy Outlook, International Energy Agency, 2013.

Wu, L., Bocquet, M., Lauvaux, T., Chevallier, F., Rayner, P., Davis, K., Optimal representation of source-sink fluxes for mesoscale carbon dioxide inversion with synthetic data, *J. Geophys. Res.*, 116, D21304, doi:10.1029/2011JD016198, 2011.

Xiao, Y., Logan, J.A., Jacob, D.J., Hudman, R.C., Yantosca, R., Blake, D.R., Global budget of ethane and regional constraints on U.S. sources, *J. Geophys. Res.*, 113, 2008.

Xiong, X., Barnett, C., Maddy, E., Sweeney, C., Liu, X., Zhou, L., and Goldberg, M.: Characterization and validation of methane products from the Atmospheric Infrared Sounder (AIRS), *J. Geophys. Res.*, 113, G00A01, doi:10.1029/2007JD000500, 2008.

Xiong, X., Barnett, C., Maddy, E.S., Gambacorta, A., King, T.S., and Wofsy, S.C., Mid-upper tropospheric methane retrieval from IASI and its validation, *Atmos. Meas. Tech.*, 6, 2255-2265, 2013.

Zhang, L., Jacob, D.J., Smith-Downey, N.V., Wood, D.A., Blewitt, D., Carouge, C.C., van Donkelaar, A., Jones, D.B.A., Murray, L.T., and Wang, Y., Improved estimate of the policy-relevant background ozone in the United States using the GEOS-Chem global model with 1/2°x2/3° horizontal resolution over North America, *Atmos. Environ.*, 45, 6769-6776, 2011.

Zhang, L., Jacob, D.J., Knipping, E.M., Kumar, N., Munger, J.W., Carouge, C.C., van Donkelaar, A., Wang, Y., and Chen, C., Nitrogen deposition to the United States: distribution, sources, and processes, *Atmos. Chem. Phys.*, 12, 4539-4554, 2012.

Zhang, Y., Jaegle, L., van Donkelaar, A., Martin, R.V., Holmes, C.D., Amos, H.M., Wang, Q., Talbot, R., Artz, R., Brooks, S., Luke, W., Holsen, T.M., Felton, D., Miller, E.K., Perry, K.D., Schmeltz, D., Steffen, A., Trodon, R., Weiss-Penzias, P., and Zsolway, R., Nested-grid simulation of mercury over North America, 2012.



## **Chapter 4. Spatially resolving methane emissions in California: constraints from the CalNex aircraft campaign and from present (GOSAT, TES) and future (TROPOMI, geostationary) satellite observations**

[Wecht, K.J., Jacob, D.J., Sulprizio, M., Santoni, G.W., Wofsy, S.C., Parker, R., Bösch, H., and Worden, J.R., in preparation for submission]

### **Abstract**

We apply a continental-scale inverse modeling system for North America based on the GEOS-Chem model to optimize California methane emissions at  $1/2^\circ \times 2/3^\circ$  horizontal resolution using atmospheric observations from the CalNex aircraft campaign (May-June 2010) and from satellites. Inversion of the CalNex data yields a best estimate for total California methane emissions of  $2.86 \pm 0.21 \text{ Tg a}^{-1}$ , compared with  $1.92 \text{ Tg a}^{-1}$  in the EDGAR v4.2 emission inventory used as a priori and  $1.51 \text{ Tg a}^{-1}$  in the California Air Resources Board (CARB) inventory used for state regulations of greenhouse gas emissions. These results are consistent with a previous Lagrangian inversion of the CalNex data. Our inversion provides 12 independent pieces of information to constrain the geographical distribution of emissions within California. Attribution to individual source types indicates dominant contributions to emissions from landfills/wastewater ( $1.1 \text{ Tg a}^{-1}$ ), livestock ( $0.87 \text{ Tg a}^{-1}$ ), and gas/oil ( $0.64 \text{ Tg a}^{-1}$ ). EDGAR v4.2 underestimates emissions from livestock while CARB underestimates emissions from

landfills/wastewater and gas/oil. Current satellite observations from GOSAT can constrain methane emissions in the Los Angeles Basin but are too sparse to constrain emissions quantitatively elsewhere in California (they can still be qualitatively useful to diagnose inventory biases). An observation system simulation experiment (OSSE) shows that the future TROPOMI satellite instrument (2015 launch) will be able to constrain California methane emissions at a detail comparable to the CalNex aircraft campaign. Geostationary satellite observations offer even greater potential for constraining methane emissions in the future.

#### **4.1 Introduction**

Quantifying greenhouse gas emissions at the national and state level is essential for climate policy. The state of California Assembly Bill 32 (AB32) legislates that state greenhouse gas emissions be brought down to 1990 levels by 2020. The California Air Resources Board (CARB) has identified the importance of reducing methane for complying with AB32 (CARB, 2013). It provides a statewide methane emission inventory for enforcement of AB32 (CARB, 2011). However, atmospheric observations from surface sites and aircraft suggest that this inventory may be too low by a factor of 2 or more (Wunch et al. 2009; Jeong et al. 2012; Peischl et al. 2012; Wennberg et al. 2012; Santoni et al. 2013). This is problematic in terms of designing a credible emissions control strategy.

Atmospheric observations play a critical role in measurement, reporting and verification (MRV) of greenhouse gas emission inventories (NRC, 2010). Surface measurements are limited in space, and aircraft campaigns are limited in time. Satellite

observations have the potential for continuous monitoring of emissions if their sensitivity and coverage is sufficient. In Wecht et al. (2013), we present a new capability developed under the NASA Carbon Monitoring System (CMS) to constrain methane emissions at high spatial resolution over North America by inversion of satellite observations in an Eulerian framework (GEOS-Chem chemical transport model). Here we apply this capability to estimate the fine-scale distribution of emissions in California by using observations from the CalNex aircraft campaign (May-June 2010) as well as from current and future satellite instruments.

Santoni et al. (2013) previously used the CalNex aircraft observations in a Lagrangian inversion of methane emissions for California, optimizing a total of 8 source types/regions within the state. They derived an optimized statewide emission of  $2.4 \text{ Tg a}^{-1}$ , as compared to  $1.5 \text{ Tg a}^{-1}$  in the CARB inventory, and attributed most of the underestimate to livestock emissions. Here we use the same CalNex observations as Santoni et al. (2013) but optimize emissions on the  $1/2^\circ \times 2/3^\circ$  ( $\sim 50 \times 50 \text{ km}^2$ ) grid of GEOS-Chem, without prior assumption on source types, thus providing a different perspective and a check on the use of different inversion methodologies.

We then apply our CMS framework to examine the constraints on California methane emissions achievable from satellite observations in comparison to the CalNex observations. Satellites measure methane from solar backscatter spectra in the short-wave infrared (SWIR) and terrestrial radiation spectra in the thermal infrared (TIR). A number of satellite instruments have the capability to observe methane (Table 4.1). SWIR retrievals are available from SCIAMACHY (2003-2012) and GOSAT (2009-present).

**Table 4.1:** Satellite observations of methane.

Instrument	Wavelength range	Launch	Return time [days] <sup>a</sup>	Pixel resolution [km <sup>2</sup> ] <sup>b</sup>	Precision	DOFS for California emissions <sup>c</sup>	Reference
<i>Global</i> <sup>d</sup>							
SCIAMACHY	SWIR	2002 <sup>e</sup>	6	30x60	1.5 %		Frankenberg et al. (2011)
AIRS	TIR	2002	0.5	45x45	1.5 %		Xiong et al. (2008)
TES	TIR	2004 <sup>f</sup>	16	5x8 <sup>g</sup>	1 %	~0	Worden et al. (2012)
IASI	TIR	2007	0.5	50x50	1.2 %		Xiong et al. (2013) Crevoisier et al. (2013)
GOSAT	SWIR	2009	3	~10x10 <sup>g</sup>	0.6 %	1.3	Parker et al. (2011) Schepers et al. (2012)
aTROPOMI	SWIR	2015	1	7x7	0.6 %	10.5	Veefkind et al. (2012) Butz et al. (2012)
<i>Geostationary</i>							
GEO-CAPE <sup>h</sup>	SWIR	~2020 <sup>i</sup>	Hourly	4x4	1.1 %	26.5	Fishman et al. (2012)

<sup>a</sup> Full global coverage except for TES and GOSAT (see footnotes *f* and *g*).

<sup>b</sup> For nadir view.

<sup>c</sup> The Degrees of Freedom for Signal (DOFS) measures the capability of the satellite observations for the CalNex period (1 May – 22 June 2010) to constrain the spatial distribution of emissions in California. Values are shown only for satellite instruments used in this work. Results for TROPOMI and GEO-CAPE are from Observation System Simulation Experiments (OSSEs). The CalNex aircraft observations have DOFS of 12.2. See text for details.

<sup>d</sup> From polar sun-synchronous low-elevation orbit.

<sup>e</sup> Terminated in 2012; methane retrieval quality degraded after 2005.

<sup>f</sup> TES measurements are limited to the orbit tracks. Regular global surveys were terminated at the end of 2011.

<sup>g</sup> GOSAT takes measurements at 5 across-track points separated by 100 km, each with a ground footprint diameter of 10 km.

<sup>h</sup> Continental observation over North America.

<sup>i</sup> No launch date has been selected.

TIR retrievals are available from AIRS (2002-present), TES (2004-2011), and IASI (2007-present). SWIR retrievals provide total atmospheric methane columns. TIR retrievals provide vertical profiles but have limited sensitivity to the lower troposphere due to lack of thermal contrast, and this limits their value for detecting regional sources (Wecht et al., 2012).

Our initial CMS application described in Wecht et al. (2013) focused on optimizing methane emissions on the continental scale of North America using SCIAMACHY observations for summer 2004. SCIAMACHY provided high-quality observations with high density until 2005, after which the sensitivity of the instrument degraded (Frankenberg et al., 2011). Current satellite observations are available from GOSAT and TES. As we will see, they are too sparse to usefully constrain the distribution of emissions within California. Drastic improvement in our ability to observe methane from space is expected in 2015 with the launch of the SWIR TROPOMI instrument (Veefkind et al., 2012; Butz et al., 2012). TROPOMI will provide daily global coverage with  $7 \times 7 \text{ km}^2$  nadir resolution. There are also several current proposals for geostationary SWIR observation of methane over North America, drawing on plans for the NASA GEO-CAPE mission (Fishman et al., 2012). Here we will evaluate the potential of these future instruments to constrain the spatial distribution of emissions at the state level by using observation system simulation experiments (OSSEs) for California anchored by our CalNex results.

#### **4.2 GEOS-Chem inverse modeling system for methane emissions**

#### 4.2.1 Forward model and optimization procedure

We use the GEOS-Chem chemical transport model (CTM) with  $1/2^\circ \times 2/3^\circ$  horizontal resolution as forward model in the inversion to optimize methane emissions on the basis of observed atmospheric concentrations. The inversion seeks an optimal solution for the spatial distribution of methane emissions consistent with both atmospheric observations and a priori knowledge. The a priori is from existing emission inventories. The forward model  $F$  relates emissions to methane concentrations. Optimization is done by minimizing the Bayesian least-squares cost function,  $J$ :

$$J(\mathbf{x}) = (\mathbf{F}(\mathbf{x}) - \mathbf{y})^T \mathbf{S}_O^{-1} (\mathbf{F}(\mathbf{x}) - \mathbf{y}) + (\mathbf{x} - \mathbf{x}_A)^T \mathbf{S}_A^{-1} (\mathbf{x} - \mathbf{x}_A) \quad (4.1)$$

Here  $\mathbf{y}$  is the ensemble of observations arranged in a vector,  $\mathbf{S}_O$  is the error covariance matrix of the observation system,  $\mathbf{S}_A$  is the error covariance matrix of the a priori emissions,  $\mathbf{x}$  is a vector of emission scale factors on the  $1/2^\circ \times 2/3^\circ$  GEOS-Chem grid, and  $\mathbf{x}_A$  is the corresponding a priori.  $\mathbf{x}$  has as elements  $x_i = E_i / E_{A,i}$ , where  $E_i$  and  $E_{A,i}$  are respectively the true and a priori methane emissions for grid square  $i$ .

Analytical solution of (4.1) yields the following expression for the optimal estimate  $\hat{\mathbf{x}}$ , its associated error covariance matrix  $\hat{\mathbf{S}}$ , and the averaging kernel matrix  $\mathbf{A}$  that describes the sensitivity of the retrieved emissions to true emissions (Rodgers, 2000):

$$\hat{\mathbf{x}} = \mathbf{x}_A + \mathbf{S}_A \mathbf{K}^T (\mathbf{K} \mathbf{S}_A \mathbf{K}^T + \mathbf{S}_O)^{-1} (\mathbf{y} - \mathbf{K} \mathbf{x}_A) \quad (4.2)$$

$$\hat{\mathbf{S}}^{-1} = \mathbf{K}^T \mathbf{S}_O^{-1} \mathbf{K} + \mathbf{S}_A^{-1} \quad (4.3)$$

$$\mathbf{A} = \mathbf{I}_n - \hat{\mathbf{S}} \mathbf{S}_A^{-1} \quad (4.4)$$

Here  $\mathbf{K}$  is the Jacobian matrix for the sensitivity of concentrations to emissions calculated with GEOS-Chem,  $\mathbf{I}_n$  is the identity matrix, and  $n$  is the dimension of  $\mathbf{x}$ .

We use GEOS-Chem version 9-01-02

(<http://acmg.seas.harvard.edu/geos/index.html>), driven by GEOS-5 meteorological data from the NASA Global Modeling and Assimilation Office (GMAO). The GEOS-5 data have  $1/2^\circ \times 2/3^\circ$  horizontal resolution, 72 vertical levels (including 14 in the lowest 2 km), and 6-h temporal resolution (3-h for surface variables and mixing depths). The simulations are for a nested version of GEOS-Chem with native  $1/2^\circ \times 2/3^\circ$  resolution for western North America and the adjacent Pacific ( $26\text{--}70^\circ\text{N}$ ,  $110\text{--}140^\circ\text{W}$ ) and 3-h dynamic boundary conditions from a global simulation with  $4^\circ \times 5^\circ$  resolution. The transport time step is 10 minutes. In our previous inverse analysis of SCIAMACHY observations for North America (Wecht et al., 2013), we used a larger nested domain ( $10\text{--}70^\circ\text{N}$ ,  $40\text{--}140^\circ\text{W}$ ). Simulations using the two domains show negligible differences over California. The trimmed domain used here makes it computationally feasible to construct the Jacobian matrix  $\mathbf{K}$  and from there to obtain the analytical solution (4.2)-(4.4) with full characterization of error statistics, unlike the numerical solution relying on the GEOS-Chem adjoint as implemented by Wecht et al. (2013). Boundary conditions are treated here by correcting the free tropospheric background to match the CalNex aircraft observations as described in section 3.

The main sink for atmospheric methane is oxidation by OH in the troposphere, and this is computed using a 3-D archive of monthly average OH concentrations from a GEOS-Chem simulation of tropospheric chemistry (Park et al. 2004). Additional minor sinks in GEOS-Chem include soil absorption (Fung et al. 1991) and stratospheric oxidation computed with archived loss frequencies from the NASA Global Modeling Initiative (GMI) Combo CTM (Considine et al. 2008, Allen et al. 2010). Tropospheric loss of methane is inconsequential here since ventilation from the western US window

domain is fast in comparison. Stratospheric loss provides a realistic stratospheric profile of methane and Wecht et al. (2012) pointed out that this is important for the inversion of satellite observations.

#### **4.2.2 A priori emissions for the inversion**

A priori anthropogenic emissions in GEOS-Chem are from the EDGAR v4.2 global inventory at  $0.1^\circ \times 0.1^\circ$  resolution for 2008, the most recent year available (EC-JRC/PBL 2009). CARB only reports statewide totals. A gridded version of the CARB inventory is available from the California Greenhouse Gas Emissions Measurement (CalGEM) Project, described by Zhao et al. (2009) and Jeong et al. (2012). The EDGAR v4.2 inventory on the scale of the US agrees well with the US Environmental Protection Agency (EPA, 2013) national inventory (Wecht et al., 2013). EDGAR emissions are aseasonal but we apply seasonality to California rice emissions following McMillan et al. (2007) with emissions in the growing season (June-September) six times higher than in the rest of the year. Natural emissions include open fires from GFED-3 with daily resolution (van der Werf et al. 2010; Mu et al. 2010) and wetlands with dependence on local temperature and soil moisture (Kaplan et al. 2002; Pickett-Heaps et al. 2011). They account for only 3% of total a priori methane emissions in California.

Table 4.2 shows the statewide emissions in the EDGAR and CARB inventories, with the contributions from different sources. EDGAR emissions are  $1.92 \text{ Tg a}^{-1}$ , 27% higher than CARB emissions of  $1.51 \text{ Tg a}^{-1}$ . There are larger discrepancies in contributions from different source types. EDGAR landfills/wastewater and gas/oil



**Table 4.2:** Methane emissions in California<sup>a</sup>

	CARB	EDGAR v4.2 <sup>b</sup>	Santoni et al. (2013) <sup>c</sup>	This study <sup>d</sup>	Other Studies <sup>e</sup>
State Total	1.51	1.92	2.37±0.27	2.86±0.21	
Landfills/ Wastewater <sup>f</sup>	0.39	0.82	0.42 <sup>g</sup>	1.05	
Gas/oil	0.18	0.51	<i>footnote c</i>	0.64	
Livestock	0.86	0.46	1.29	0.87	
Rice	0.027	0.033	0.069	0.08	0.078-0.093 <sup>h</sup>
Other <sup>i</sup>	0.05	0.10	<i>footnote c</i>	0.13	
Natural <sup>j</sup>				0.08	
Los Angeles Basin		0.54	0.28-0.39	0.42±0.08 0.31±0.08 <sup>k</sup>	0.6±0.1 <sup>l</sup> 0.38±0.1 <sup>m</sup> 0.44±0.15 <sup>n</sup> 0.41±0.04 <sup>o</sup>

<sup>a</sup> Units are Tg a<sup>-1</sup>. Estimates from the CARB and EDGAR v4.2 inventories are compared to inversion results from this work and other studies. Values are for 2010 unless otherwise noted.

<sup>b</sup> For 2008, the latest year available.

<sup>c</sup> Lagrangian inversion using CalNex observations and resolving 8 source types/regions. They give a total emission estimate of 0.59 Tg a<sup>-1</sup> from the sum of wastewater, gas/oil, and other sources without a further source breakdown.

<sup>d</sup> Inversion at 1/2°x2/3° resolution using CalNex observations unless otherwise indicated; source type attribution is inferred by mapping optimized emissions to the EDGAR source type distributions.

<sup>e</sup> Estimates constrained by atmospheric observations from surface or aircraft

<sup>f</sup> These two sources are combined here because of the similarity of their geographical distributions in EDGAR v4.2. Landfills account for 80% of this combined source according to both CARB and EDGAR v4.2.

<sup>g</sup> Landfills only.

<sup>h</sup> McMillan et al. (2007), Peischl et al. (2012).

<sup>i</sup> Including biofuels and other minor sources.

<sup>j</sup> Including wetlands, termites, and open fires.

<sup>k</sup> From inversion of GOSAT observations during CalNex.

<sup>l</sup> Wunch et al. (2009) estimate for 2007-2008.

<sup>m</sup> Hsu et al. (2010) estimate for 2007-2008.

<sup>n</sup> Wennberg et al. (2012) estimate for both 2008 and 2010.

<sup>o</sup> Peischl et al. (2013).

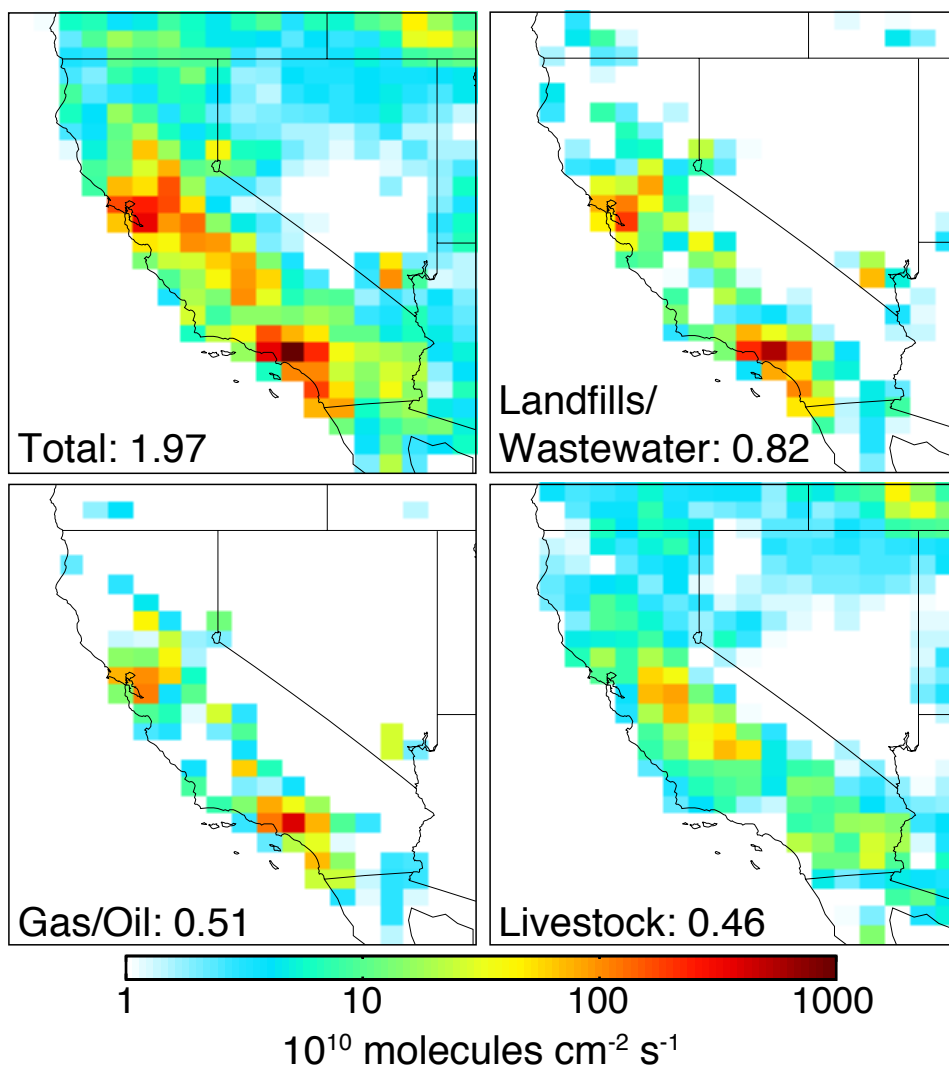
emissions are higher than CARB by more than a factor of 2. EDGAR livestock emissions, on the other hand, are lower than CARB by a factor of 2. The CalNex observations can arbitrate on these discrepancies as will be discussed in section 3.3.

Figure 4.1 shows the distribution of EDGARv4.2 emissions across California. Landfill/wastewater and gas/oil emissions closely follow population distribution. Landfill/wastewater includes landfills (79%) and wastewater treatment (21%) with similar spatial patterns in EDGAR. The gas/oil source is dominated by natural gas emissions (94%) and the correlation with population in EDGAR suggests that it is mostly from distribution rather than extraction, which is concentrated in the southwestern end of the Central Valley. Livestock emissions are mostly in the Central Valley and include both enteric fermentation and manure management.

### **4.3. Inversion of CalNex Observations**

#### **4.3.1 Observations and error characterization**

Santoni et al. (2013) measured methane concentrations aboard the CalNex aircraft with a Quantum Cascade Laser Spectrometer (QCLS) (Kort et al. 2012), and derived methane emissions from these observations with an inversion using the Stochastic Time-Inverted Lagrangian Transport (STILT) model. Methane was also measured aboard the CalNex aircraft with a Cavity Ring-Down Spectrometer (CRDS) (Peischl et al. 2012), and Santoni et al. (2013) used these observations to fill gaps in the QCLS record after correcting for bias between the two instruments. They used observations between 2-4 km



**Figure 4.1:** EDGAR v4.2 methane emissions for 2008 used as a priori for our inversion. Panels show total emissions and contributions from the three major source types. California totals in  $\text{Tg a}^{-1}$  are inset. Values are averaged over the  $1/2^\circ \times 2/3^\circ$  GEOS-Chem grid.

for each flight to constrain the free tropospheric background, and the observations below 2 km to constrain California emissions. We follow the same approach here, correcting the GEOS-Chem concentrations for the observed free tropospheric background on individual days. This effectively accounts for boundary conditions. Data selection criteria are described by Santoni et al. (2013).

Figure 4.2 (left) shows the mean observed methane concentrations below 2 km from the 11 daytime CalNex flights used by Santoni et al. (2013) in their inversion. Values are highest over the Central Valley and the Los Angeles Basin. We use the same observations for our inversion after averaging horizontally, vertically, and temporally over the GEOS-Chem grid. The resulting observation vector  $\mathbf{y}$  has 1993 elements. We use it to optimize emissions (state vector  $\mathbf{x}$ ) from the  $157 \frac{1}{2}^\circ \times 2\frac{1}{3}^\circ$  model grid squares that comprise California. The middle panel of Figure 4.2 shows the GEOS-Chem simulation with a priori EDGAR emissions and after correcting for the free tropospheric background. There is a general underestimate and discrepancies in patterns that point to errors in the EDGAR emissions.

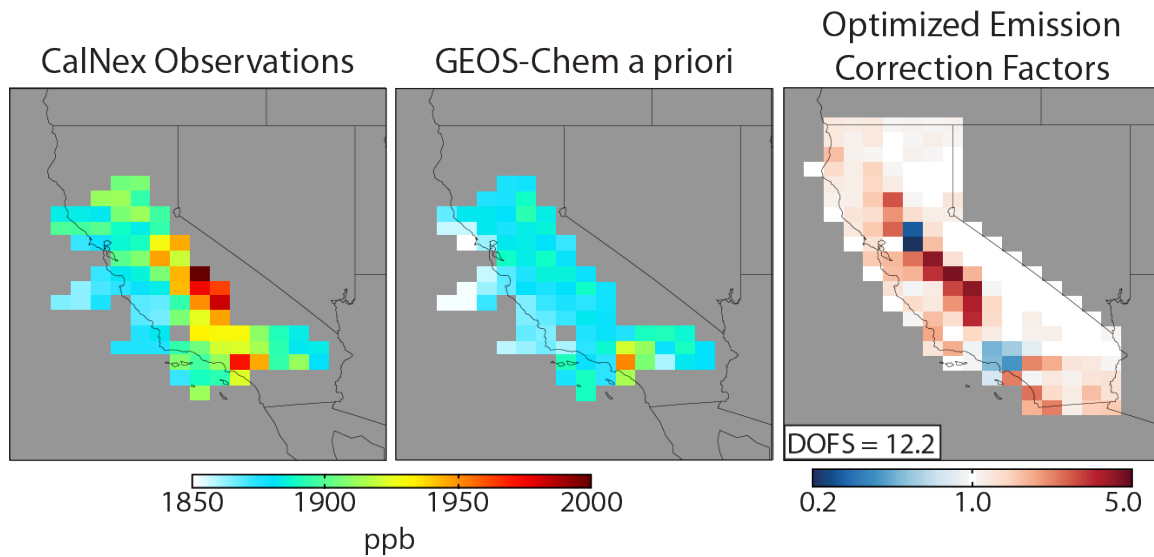


**Figure 4.2:** Mean methane concentrations below 2 km altitude during CalNex (May-June 2010). Aircraft observations averaged on the  $1\frac{1}{2}^\circ \times 2\frac{1}{3}^\circ$  GEOS-Chem grid (left) are compared to the GEOS-Chem simulation using EDGAR v4.2 a priori emissions (Figure 4.1) and adjusted free tropospheric background (see text). The optimized correction factors to the EDGAR v4.2 emissions from inversion of the CalNex observations are shown on the right. DOFS from the inversion is inset Gray grid squares in the right panel are excluded from the optimization.

We use the residual error method of Heald et al. (2004) to estimate the observational error variances (diagonal elements of  $\mathbf{S}_O$ ). This involves partitioning of the observation vector into coherent subsets within which the error statistics can be assumed homogeneous. The subsets are defined here by altitude and geographical region: Central Valley, Los Angeles Basin, San Francisco Bay Area, rest of California, and Pacific Ocean. For each subset we assume that the mean difference between observations and the model with a priori sources is caused by error on the a priori sources. The residual standard deviation (RSD) is then assumed to represent the standard deviation of the observational error. RSD is largest (50-70 ppb) in the lowest 1 km over the Central Valley and the Los Angeles Basin, reflecting small-scale transport and spatial variability in emissions not resolved by the model. RSD below 1 km in other regions is typically 20-40 ppb. RSD in all regions decreases with altitude to 15-20 ppb at 2 km. For each element of  $\mathbf{y}$  in the subset we populate the diagonal of  $\mathbf{S}_O$  with the observational error variance,  $\text{RSD}^2$ . Variograms show no significant temporal or horizontal error correlations between observations on the GEOS-Chem grid. We therefore take  $\mathbf{S}_O$  to be diagonal.

The a priori error covariance matrix,  $\mathbf{S}_A$ , is constructed by assuming a uniform 75% uncertainty on a priori emissions from every grid square. This magnitude of uncertainty is consistent with the discrepancies between CARB and EDGAR and with the results of Santoni et al. (2013). We assume no error correlations so that  $\mathbf{S}_A$  is diagonal. Sensitivity of the inversion results to specification of  $\mathbf{S}_A$  is examined in section 3.3.

Care is required to account for model errors in planetary boundary layer (PBL) height. High Spectral Resolution Lidar (HSRL) aircraft observations during CalNex indicated mean midday PBL heights of 1.0 km in the Central Valley and the Los Angeles

Basin (Fast et al. 2012). The GEOS-5 meteorological data used in GEOS-Chem are biased high by 0.3 km in both regions. This would be of no consequence if the 0-2 km column was evenly sampled by the observations, but most of the observations are in fact below 1 km altitude and the PBL bias would cause a model underestimate unrelated to emissions. To address this we weigh the individual CalNex observations in the inversion to enforce even sampling of the 0-2 km column.

#### 4.3.2 Inversion Results

Figure 4.2 (right) shows optimized correction factors to the EDGAR v4.2 a priori emissions from the inversion and Figure 4.3 shows the optimized emissions. The optimized state total emission in California is  $2.86 \pm 0.21 \text{ Tg a}^{-1}$ , compared with  $1.92 \text{ Tg a}^{-1}$  for EDGAR and  $1.51 \text{ Tg a}^{-1}$  for CARB. The uncertainty on the optimized estimate is provided by the error covariance matrix  $\hat{S}$  computed from (3). Emissions increase relative to EDGAR v4.2 primarily over the Central Valley, by up to a factor of 4.5. The increase largely follows the pattern of livestock emissions. Emissions decrease over the Los Angeles Basin and the area around Sacramento. Source type allocation is further discussed in section 3.3.

Table 4.2 compares the statewide emissions calculated here and by Santoni et al. (2013). Our state total is larger than their  $2.37 \pm 0.27 \text{ Tg a}^{-1}$  but this appears to reflect their use of a lower a priori inventory. When they use the EDGAR v4.2 inventory as a priori in a sensitivity inversion they obtain an optimized emission of  $2.8 \text{ Tg a}^{-1}$ , consistent with ours. We conducted sensitivity inversions assuming 50% and 100% uncertainties in the EDGAR v4.2 a priori emissions for individual grid squares (instead of 75% in the

standard inversion) and found optimized statewide emissions of 2.59 and 3.10  $\text{Tg a}^{-1}$ , respectively. This illustrates the sensitivity of the optimization to the choice of a priori, although the result that the a priori is too low is robust.

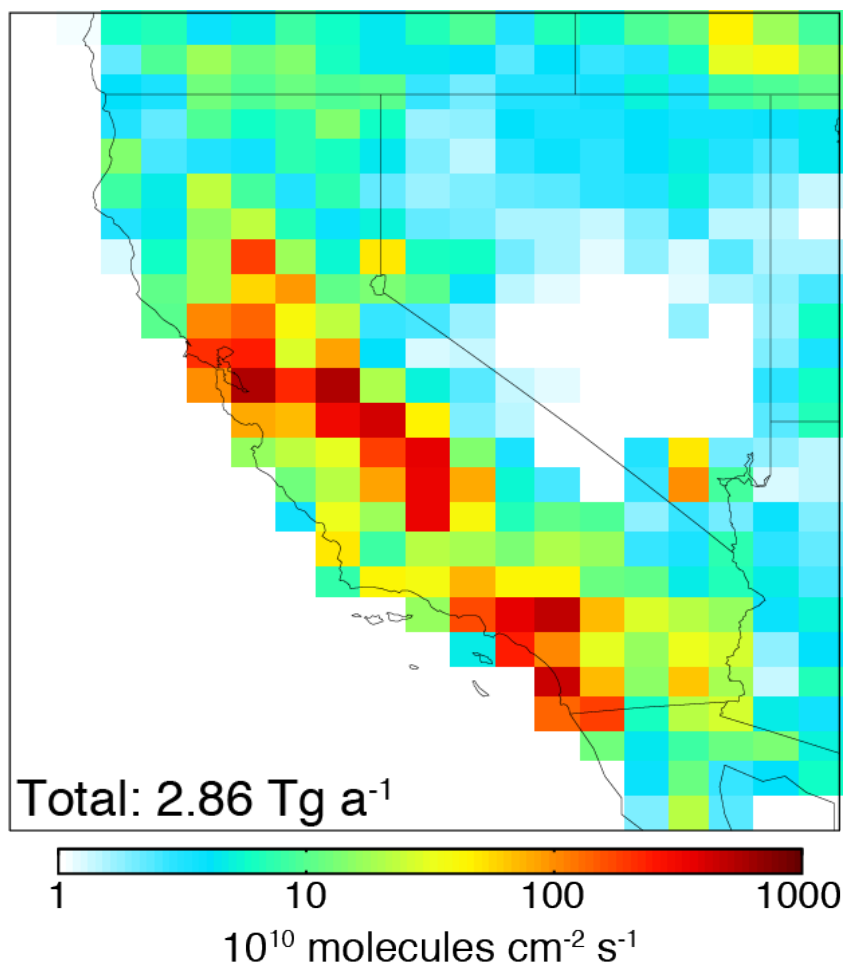


**Figure 4.3:** Optimized methane emissions from our inversion using CalNex observations. Total California emissions are inset. See Table 4.2 for source type attribution.

A number of previous studies have used atmospheric observations to estimate methane emissions in the Los Angeles Basin and find values in the range 0.38-0.6  $\text{Tg a}^{-1}$  (Table 4.2). Santoni et al. (2013) estimate a range of 0.29-0.38  $\text{Tg a}^{-1}$ . Our inversion yields an optimized estimate of  $0.42 \pm 0.08 \text{ Tg a}^{-1}$  for the Los Angeles Basin, in the range of these previous studies.

The extent to which the inversion can constrain the spatial distribution of emissions in California can be measured by the degrees of freedom for signal (DOFS), calculated as the trace of the averaging kernel matrix  $\mathbf{A}$  (Rodgers, 2000). DOFS is a measure of the number of independent elements in the retrieved emission field. Higher DOFS means that more information is available to constrain the spatial distribution of emissions. In an ideal inversion where all  $n$  state vector elements (emissions in individual grid squares) are fully constrained by the observations,  $\mathbf{A}$  would be the identity matrix and we would have  $\text{DOFS} = n$ .

Figure 4.4 (top left) shows a map of the diagonal elements of  $\mathbf{A}$  in each grid square for the CalNex inversion. Values represent the degrees of freedom associated with each grid square. i.e., the ability of the observations to constrain emissions in that grid square (1 = fully, 0 = not at all), or in other words the relative contributions of the observations and the a priori in constraining the inverse solution. We find values approaching 1 in the Los Angeles Basin and the San Francisco Bay area, and typically 0.2-0.8 in the Central Valley. Low values are associated with areas that were either not adequately covered by the CalNex aircraft (Figure 4.2) or have low emissions (Figure 4.1) and thus little influence on the inversion. Overall our inversion has a total DOFS for California of 12.2, indicating that we can constrain 12 independent pieces of information.

### **4.3.3 Attribution to Source Types**

Our inversion optimizes methane emissions on a geographical grid without a priori consideration of source type. This can be contrasted to the Santoni et al. (2013) inversion, which optimized emissions by source type assuming that the a priori pattern



## Inversion Degrees of Freedom per Grid Square

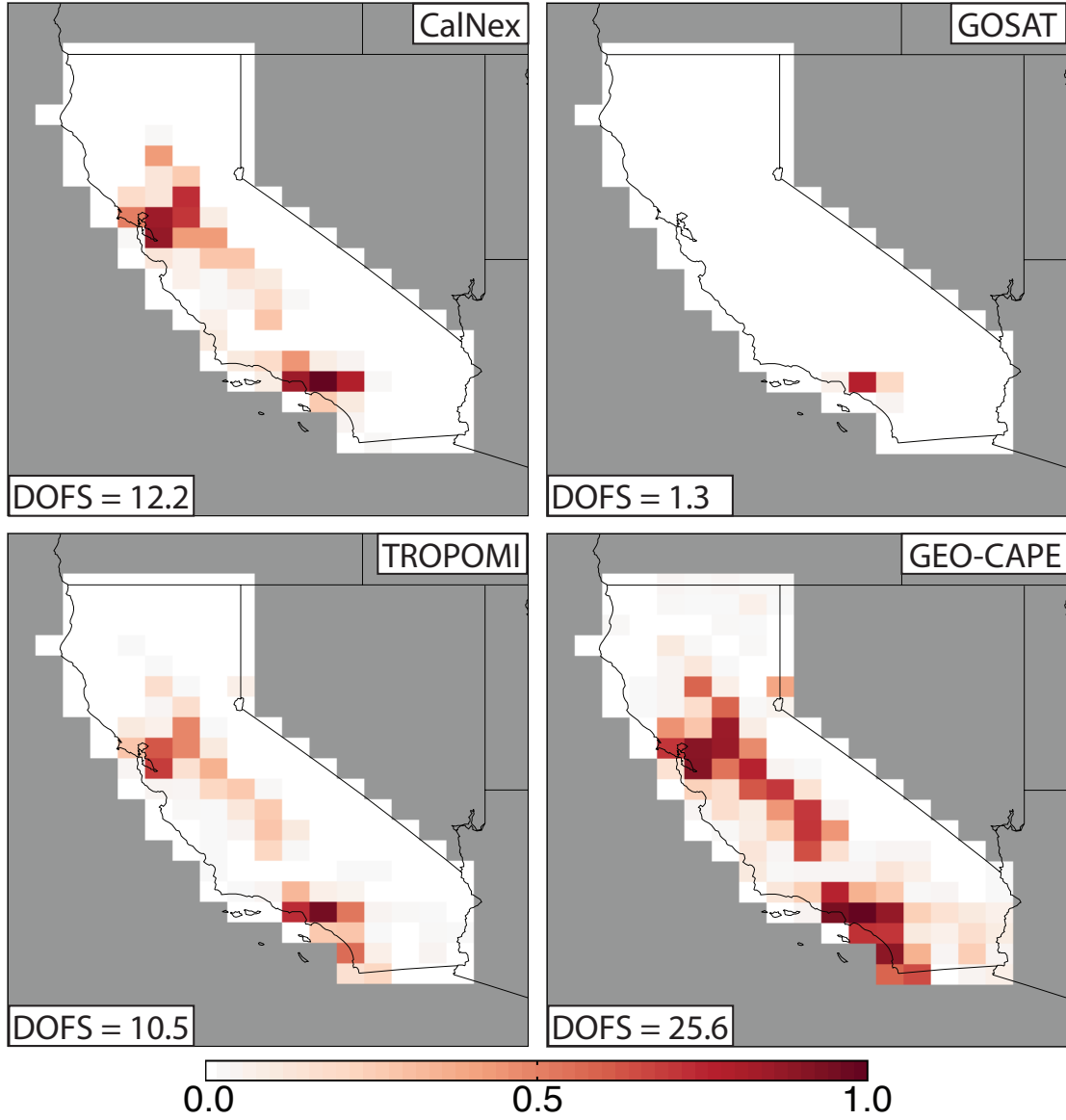


**Figure 4.4:** Degrees of freedom in each grid square from our inversions using CalNex (top, left) and GOSAT (top, right) observations and from our OSSEs using TROPOMI (bottom, left) and geostationary (bottom, right) synthetic observations. Values are the diagonal elements of the averaging kernel matrix for the inversion and represent the ability of the observations to constrain local emissions (see text). The sum of these degrees of freedom (trace of the average kernel matrix) represents the degrees of freedom for signal (DOFS) of the inversions, inset. Gray grid squares are excluded from the optimization.

for each source type was correct. Ultimately, our spatial correction factors need to be related to source types in order to guide the improvement of inventories. This can be done by mapping the results onto the a priori source patterns of Figure 4.1, with the caveat that the patterns may not be correct.

We conducted the mapping of our optimized emissions to source types by applying the optimized total emissions for each grid square (right panel of Figure 4.2) to the relative contributions from each major source type in that grid square, as given by the EDGAR v4.2 inventory and plotted in Figure 4.1. This method assumes that EDGAR correctly identifies the relative contributions of each source type to the total emissions in a given grid square. Results in Table 4.2 show that livestock emissions increase statewide by 92% relative to EDGAR, landfill/wastewater by 28%, and gas/oil by 26%.

To examine the degree to which our inversion results can be explained by the patterns in the EDGAR a priori inventory, we performed a multiple linear regression (MLR) to fit the inversion corrections in each California grid square of Figure 4.3 ( $n = 157$ ) to the a priori spatial patterns from each source type (landfill/wastewater, gas/oil, livestock, other anthropogenic, rice, wetlands, and biofuel;  $n = 7$ ). The MLR best fit has an  $R^2$  of 0.54, indicating that the a priori source patterns can explain about half of the correction. These patterns are too spatially correlated (e.g., landfill/wastewater and gas/oil in Figure 4.1) for the MLR coefficients to provide meaningful attribution to individual source types. The residual not explained by the MLR points to spatial variability in activity rates and emissions factors not accounted for in EDGAR.

We pointed out above the large discrepancies between CARB and EDGAR for different source types (Table 4.2). Our livestock estimate is much higher than EDGAR but agrees

with CARB, in contrast to Santoni et al. (2013) who concluded that livestock emissions in CARB are 50% too low. On the other hand, our emissions from landfills/wastewater and gas/oil are higher than CARB by factors of 2.7 and 3.6, respectively, and are in closer agreement with EDGAR. Rice emissions, although small, are underestimated by a factor of 2-3 in the CARB and EDGAR inventories, consistent with the previous findings of McMillan et al. (2007) and Peischl et al. (2012).

#### 4.4 Utility of Current Satellites (GOSAT, TES) for Constraining California Emissions

Satellite observations of atmospheric methane from GOSAT and TES were operational during CalNex and we examine their combined value for constraining emissions from California over that period. GOSAT is in a sun-synchronous polar orbit with an equator overpass local time of ~10:00. It retrieves methane from nadir SWIR spectra near 1.6  $\mu\text{m}$ . Measurements consist of five across-track points separated by ~100 km, with footprint diameters of 10.5 km. Observations are limited to daytime and land. We use the University of Leicester GOSAT Proxy XCH<sub>4</sub> v3.2 data described by Parker et al. (2011) (available from <http://www.leos.le.ac.uk/GHG/data/>) to populate our observation vector  $\mathbf{y}$ . These data are for methane column mixing ratios  $X_{CH_4}$  [v/v] retrieved by the CO<sub>2</sub> proxy method:

$$X_{CH_4} = \frac{X_{CO_2}}{\Omega_{CO_2}} (\Omega_A + \mathbf{a}^T (\boldsymbol{\omega} - \boldsymbol{\omega}_A)) \quad (4.5)$$

where  $\boldsymbol{\omega}$  is the true vertical profile of methane consisting of 20 partial columns,  $\boldsymbol{\omega}_A$  is the a priori profile provided by the TM3 chemical transport model,  $\Omega_A$  is the corresponding a priori column concentration of methane [molecules cm<sup>-2</sup>],  $\mathbf{a}$  is an averaging kernel vector

that describes the sensitivity as a function of altitude,  $\Omega_{\text{CO}_2}$  is the vertical column concentration of  $\text{CO}_2$ , and  $X_{\text{CO}_2}$  is a modeled column mixing ratio of  $\text{CO}_2$ . The sensitivity characterized by  $\mathbf{a}$  is nearly uniform in the troposphere and decreases with altitude in the stratosphere. The normalization by  $\text{CO}_2$  corrects for aerosol and partial cloud effects as described by Frankenberg et al. (2006).

TES is in a sun-synchronous polar orbit with an equator overpass local time of  $\sim 13:45$ . It retrieves methane from nadir TIR spectra at  $7.58 - 8.55 \mu\text{m}$ . It makes nadir observations with a pixel resolution of  $5.3 \times 8.3 \text{ km}^2$  every 182 km along the orbit track. Successive orbit tracks are separated by about  $22^\circ$  longitude. We use the most recent V005 Lite product (Worden et al., 2012; <http://tes.jpl.nasa.gov/data/>). Vertical methane profiles are retrieved as:

$$\ln \hat{\mathbf{z}} = \ln \mathbf{z}_A + \mathbf{A}'(\ln \mathbf{z} - \ln \mathbf{z}_A) \quad (4.6)$$

where  $\hat{\mathbf{z}}$  is the retrieved vertical profile vector consisting of mixing ratios on a fixed pressure grid,  $\mathbf{A}'$  is the averaging kernel matrix that represents the sensitivity of the retrieved profile to the true profile  $\mathbf{z}$ , and  $\mathbf{z}_A$  is an a priori profile from the MOZART CTM. TES is mostly sensitive to the middle-upper troposphere and insensitive to the boundary layer. We use it to characterize the free tropospheric background against which the boundary layer enhancements detected by GOSAT can be measured.

We use GOSAT and TES observations for the CalNex period, 1 May to 22 June 2010, and for the domain ( $32^\circ$ - $42^\circ$  N,  $125^\circ$ - $114^\circ$  W), as shown in Figure 4.5. There are 257 and 133 GOSAT and TES observations on the GEOS-Chem grid. We subtract biases from GOSAT (-7.5 ppb) and TES (28 ppb) based on validations of Parker et al. (2011) and Wecht et al. (2012), respectively. We subtract a mean bias of 1.5 ppb from GEOS-

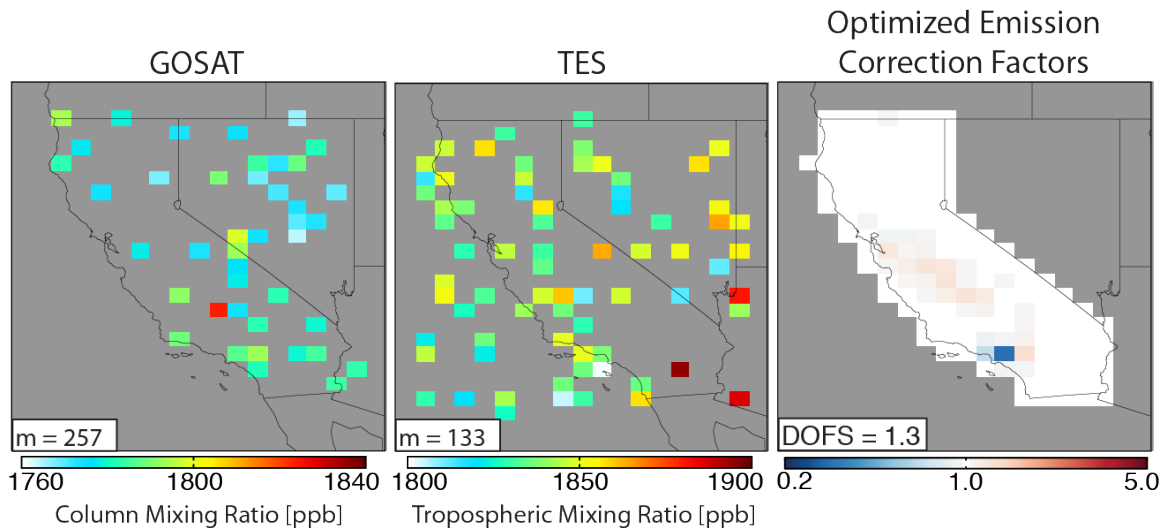


**Figure 4.5:** Mean methane mixing ratios measured by GOSAT (left) and TES (center) for the CalNex period of 1 May – 22 June 2010, and optimized correction factors (right) to the a priori EDGAR v4.2 methane emissions from the GOSAT inversion. Observations are plotted on the GEOS-Chem grid. The total number  $m$  of observations is inset. The TES data are vertical averages of tropospheric levels, while the GOSAT data are average column mixing ratios including the stratosphere, which explains the lower values. DOFS from the GOSAT inversion is inset in the right panel. Gray grid squares in the right panel are excluded from the optimization.

Chem based on comparison with TES as measure of the tropospheric background.

Figure 4.5 (right) shows the optimized correction factors to the a priori EDGAR v4.2 emissions for an inversion using the GOSAT observations. Observational errors for the inversion are determined using the residual error method described above and indicate RSD values in the range 10-12 ppb. The inversion has 1.3 DOFS, compared to 12.2 DOFS for the inversion using the CalNex observations. The correction factors have a pattern similar to those from the CalNex inversion, showing that the constraints from GOSAT on methane emissions are qualitatively consistent with CalNex. However, Central Valley correction factors are driven by just three observations located at the southern end of the Valley, apparent in Figure 4.5. Overall, correction factors are much

weaker than in the CalNex inversion, reflecting the low DOFS. A map of the degrees of freedom associated with each grid square is shown in Figure 4.4 (top, right). 1.1 of the DOFS from GOSAT are for the Los Angeles Basin and the optimization of emissions there should be quantitative: we find  $0.31 \pm 0.08 \text{ Tg a}^{-1}$ , at the lower end of values in Table 4.2. Outside of the Los Angeles Basin the DOFS sum to just 0.2.

#### **4.5 Potential of future satellites (TROPOMI, geostationary)**

The TROPOMI satellite instrument (2015 launch) will measure atmospheric methane with far greater coverage than either GOSAT or TES (Table 4.1). There are in addition several proposals to measure methane from geostationary orbit and the GEO-CAPE instrument described by Fishman et al. (2012) presents such a possibility. We conducted OSSEs to evaluate the potential of these future satellite instruments for constraining California methane emissions. For this purpose, we take the CalNex optimized emissions in Figure 4.3 as the “true” emissions to be retrieved by the inversion, and use these emissions in GEOS-Chem to generate a “true” atmosphere. We sample this “true” atmosphere with the observation frequency of TROPOMI and GEO-CAPE, apply the corresponding averaging kernels for the instruments, and add random Gaussian noise of the expected magnitude. Instrument specifications are in Table 4.1. We then conduct an inversion of these synthetic observations exactly as described above, using the a priori emissions described in section 2.2 and shown in Figure 4.1, and diagnose the potential value of the satellite instruments by their ability to constrain a priori sources as measured by the DOFS. A caveat is that the OSSE uses the same forward model to generate synthetic observations and to invert these observations, and this may lead to

overoptimistic inversion results.

We perform OSSEs for the CalNex period of 1 May – 22 June 2010 and using synthetic observations for the land domain ( $32^{\circ}$ - $42^{\circ}$  N,  $125^{\circ}$ - $114^{\circ}$  W) in the same way as for GOSAT. TROPOMI observations provide complete coverage daily and GEO-CAPE hourly. Both TROPOMI and GEO-CAPE are SWIR instruments and we use a single averaging kernel from GOSAT to generate synthetic observations for both; this is of little consequence as the averaging kernel for SWIR observations is near unity in the troposphere in any case. We randomly remove 80% of synthetic observations to simulate the effect of cloud cover. Each element of the observation vector  $\mathbf{y}$  represents the average methane column mixing ratio observed over a GEOS-Chem grid square. When multiple synthetic observations exist in the same  $0.5^{\circ} \times 0.67^{\circ}$  GEOS-Chem grid square, we average them into one single observation with square root decrease of the measurement error following the central limit theorem.

Observational error for the OSSE is estimated as the sum of measurement and model error, since the measurements are dense enough that representation error can be neglected. We specify the model error standard deviation to be 12 ppb, a conservative estimate based on the observational error for GOSAT. Measurement error (Table 4.1) and model error are added in quadrature to populate the diagonal of  $\mathbf{S}_0$  and off-diagonal terms are ignored. Model error dominates measurement error because of the averaging of the measurements over GEOS-Chem grid squares described above. The a priori error covariance matrix is populated in the same way as above. We assume no background bias in the model or observations as this could be corrected through other observations such as a TIR instrument (e.g., TES for GOSAT) or by iterative adjustment of emissions and

boundary conditions in the inversion (Wecht et al., 2013).

Figure 4.4 (bottom) summarizes the OSSE results. The TROPOMI inversion has 10.5 DOFS (Figure 4.4, bottom, left), comparable to the CalNex inversion (12.2 DOFS), and it accurately captures the spatial pattern of a priori emission errors. Optimized statewide emissions are  $2.60 \text{ Tg a}^{-1}$ , compared with  $2.86 \text{ Tg a}^{-1}$  from the “true” emissions. We conclude that TROPOMI may perform just as well as a dedicated aircraft campaign (CalNex), and is thus superbly positioned to constrain emissions at the state level. The GEO-CAPE inversion has 26.5 DOFS (Figure 4.4, bottom, right), much higher than CalNex and TROPOMI, reflecting the greater density of observations. Optimized statewide emissions are  $2.79 \text{ Tg a}^{-1}$ , close to the “true” emissions of  $2.86 \text{ Tg a}^{-1}$ . This reveals the considerable potential of geostationary observations for monitoring methane emissions on fine scales.

## 4.6 Conclusions

We applied an inverse modeling system based on the GEOS-Chem Eulerian chemical transport model (CTM) to optimize methane emissions from California with  $1/2^\circ \times 2/3^\circ$  horizontal resolution using observations from the May-June 2010 CalNex aircraft campaign. The system is designed to optimize emissions on the continental scale using satellite observations (Wecht et al., in prep) and here we evaluated its potential to constrain the spatial distribution of emissions at the state level. We compared the constraints achievable with the CalNex aircraft observations to those achievable from current (GOSAT, TES) and future (TROPOMI, geostationary) satellite observations of methane. We also compared the Eulerian GEOS-Chem inversion of CalNex observations



to a Lagrangian (STILT) inversion of methane emissions using exactly the same observations (Santoni et al., 2013), thus providing a perspective on the use of different inversion methodologies. Because the inversion was conducted over a limited spatial domain, we could obtain analytical solutions with full error characterization to compare the different observing systems.

Our inversion of CalNex observations yields a best estimate of  $2.86 \pm 0.21 \text{ Tg a}^{-1}$  for total California emissions, compared to  $1.92 \text{ Tg a}^{-1}$  in the EDGAR v4.2 inventory used as a priori for the inversion,  $1.51 \text{ Tg a}^{-1}$  in the California Air Resources Board (CARB) inventory used as basis to regulate greenhouse gas emissions in California, and  $2.37 \pm 0.27 \text{ Tg a}^{-1}$  in the Santoni et al. (2013) inversion. Our results are consistent with Santoni et al. (2013) considering that they used a lower a priori emission estimate for their inversion. An important distinction between the two inversions is that we optimize emissions geographically in 157 grid squares whereas they optimize emissions for 8 source types. Error statistics on our inversion indicates that it provides 12 independent pieces of information (measured by degrees of freedom for signal or DOFS). We have particularly strong constraints on emissions in the Los Angeles Basin where our emission estimate ( $0.42 \pm 0.08 \text{ Tg a}^{-1}$ ) is consistent with previous studies.

The CARB and EDGAR v4.2 emission inventories show factor of 2 differences between each other in their state total estimates of emissions from livestock, landfills/wastewater, and gas/oil. Our results provide guidance for resolving these discrepancies. Mapping our optimized estimate of the spatial distribution of California methane emissions onto individual source types indicates a state total livestock emission of  $0.87 \text{ Tg a}^{-1}$ , in close agreement with CARB but much higher than EDGAR and lower

than the  $1.29 \text{ Tg a}^{-1}$  estimate of Santoni et al. (2013). On the other hand, our best estimate of emissions from landfills/wastewater ( $1.05 \text{ Tg a}^{-1}$ ) and gas/oil ( $0.64 \text{ Tg a}^{-1}$ ) is 20% higher than EDGAR but much higher than CARB or Santoni et al. (2013). Our results suggest that the CARB inventory should correct its landfills/wastewater and gas/oil emission estimates by upward correction to the EDGAR v4.2 values. About half of our correction to emissions cannot be mapped onto a priori source types, implying inventory errors in the geographic variability of emission factors (e.g. livestock and manure management practices) and activity rates (e.g. landfill locations and gas/oil production).

We find that current satellite observations of methane from GOSAT and TES are too sparse to quantitatively constrain California emissions. TES is only useful for constraining the free tropospheric background. GOSAT provides quantitative constraints on emissions in the Los Angeles Basin but not elsewhere. However, the qualitative corrections to a priori emissions from the GOSAT observations across the state are consistent with those from the CalNex observations. They consistently point to a large underestimate of livestock emissions in the EDGAR v4.2 inventory. In the absence of a dedicated aircraft study such as CalNex, GOSAT can be useful as a qualitative indicator of biases in methane emission inventories.

The TROPOMI satellite instrument to be launched in 2015 has considerable potential for improving our capability to monitor methane emissions from space. TROPOMI will provide global daily coverage of methane columns with  $7 \times 7 \text{ km}^2$  nadir resolution. We find in an observation system simulation experiment (OSSE) that the observing power of TROPOMI for constraining methane emissions in California will be comparable to that of the CalNex aircraft campaign. Geostationary observations of

methane proposed for the coming decade have even more potential for constraining methane emissions. These satellite measurements will provide monitoring, reporting, and verification (MRV) for the development of methane emission control strategies in the context of climate policy. This will be particularly important in a world of rapidly changing methane emissions from natural gas exploitation, hydrofracking, and agricultural management practices.

### **Acknowledgments**

This work was supported by the NASA Carbon Monitoring System (CMS), the NASA Atmospheric Composition Modeling and Analysis Program (ACMAP) and by a NASA Earth System Science Fellowship to KJW.

## References

- Allen, D., K. Pickering, B. Duncan, and M. Damon (2010), Impact of lightning NO emissions on North American photochemistry as determined using the Global Modeling Initiative (GMI) model, *J. Geophys. Res.*, 115, D22301, doi:10.1029/2010JD014062.
- Butz, A., Galli, A., Hasekamp, O., Landgraf, J., Tol, P., and Aben, I.: TROPOMI aboard Precursor Sentinel-5 Precursor: Prospective performance of CH<sub>4</sub> retrievals for aerosol and cirrus loaded atmospheres, *Remote Sens. Environ.*, 120, 267–276, doi:10.1016/j.rse.2011.05.030, 2012.
- California Air Resources Board, California Greenhouse Gas Emission Inventory: 2000-2009, [http://www.arb.ca.gov/cc/inventory/pubs/reports/ghg\\_inventory\\_00-09\\_report.pdf](http://www.arb.ca.gov/cc/inventory/pubs/reports/ghg_inventory_00-09_report.pdf), 2011.
- California Air Resources Board, Climate Change Scoping Plan First Update: Discussion Draft for Public Review and Comment, [http://www.arb.ca.gov/cc/scopingplan/2013\\_update/discussion\\_draft.pdf](http://www.arb.ca.gov/cc/scopingplan/2013_update/discussion_draft.pdf), 2013.
- Committee on Methods for Estimating Greenhouse Gas Emissions, Verifying greenhouse gas emissions: methods to support international climate agreements, National Research Council, Natl. Acad. Press, 2010.
- Considine, D. B., J. A. Logan, and M. A. Olsen (2008), Evaluation of near-tropopause ozone distributions in the Global Modeling Initiative combined stratosphere/troposphere model with ozonesonde data, *Atmos. Chem. Phys.*, 8(9), 2365–2385, doi:10.5194/acp-8-2365-2008.
- Crevoisier, C., Nobileau, D., Armante, R., Crépeau, L., Machida, T., Sawa, Y., Matsueda, H., Schuck, T., Thonat, T., Pernin, J., Scott, N. A., and Chédin, A.: The 2007–2011 evolution of tropical methane in the mid-troposphere as seen from space by MetOp-A/IASI, *Atmos. Chem. Phys.*, 13, 4279–4289, doi:10.5194/acp-13-4279-2013, 2013.
- European Commission, Joint Research Centre (JRC)/Netherlands Environmental Assessment Agency (PBL). Emission Database for Global Atmospheric Research (EDGAR), release version 4.0. <http://edgar.jrc.ec.europa.eu>, 2009.
- Fast, J.D., Gustafson Jr., W.I., Berg, L.K., Shaw, W.J., Pekour, M., Shrivastava, M., Barnard, J.C., Ferrare, R.A., Hostetler, C.A., Hair, J.A., Erickson, M., Jobson, B.T., Flowers, B., Dubney, M.K., Springston, S., Pierce, R.B., Dolislager, L., Pederson, J., and Zaveri, R.A., Transport and mixing patterns of Central California during the carbonaceous aerosol and radiative effects study (CARES), *Atm. Chem. Phys.*, 12, 1759–1783, 2012.
- Fishman, J., Iraci, L.T., Al-Saadi, J., Chance, K., Chavez, F., Chin, M., Coble, P., Davis, C., DiGiacomo, P.M., Edwards, D., Eldering, A., Goes, J., Herman, J., Hu, C., Jacob,

D.J., Jordan, C., Kawa, S.R., Key, R., Liu, X., Lohrenz, S., Mannino, A., Natraj, V., Neil, D., Neu, J., Newchurch, M., Pickering, K., Salisbury, J., Sosik, H., Subramaniam, A., Tzortziou, M., Wang, J., and Wang, M., The United States' next generation of atmospheric composition and coastal ecosystem measurements: NASA's geostationary coastal and air pollution events (GEO-CAPE) mission. *Bulletin of the American Meteorological Society* 93, 1547-1566.

Frankenberg, C., Meirink, J. F., Bergamaschi, P., Goede, A. P. H., Heimann, M., Koenig, S., Platt, U., van Weele, M., and Wagner, T.: Satellite cartography of atmospheric methane from SCIAMACHY on board ENVISAT: Analysis of the years 2003 and 2004, *J. Geophys. Res.*, 111, D07303, doi:10.1029/2005JD006235, 2006.

Frankenberg, C., Aben, I., Bergamaschi, P., Dlugokencky, E. J., van Hees, R., Houweling, S., van der Meer, P., Snel, R. and Tol, P.: Global column-averaged methane mixing ratios from 2003 to 2009 as derived from SCIAMACHY: Trends and variability, *J. Geophys. Res.*, 116, D02304, doi:10.1029/2010JD014849, 2011.

Fung, I., John, J., Lerner, J., Matthews, E., Prather, M., Steele, L. P., and Fraser, P. J.: Three-dimensional model synthesis of the global methane cycle, *J. Geophys. Res.*, 96, 13 033–13 065, 1991.

Heald, C., Jacob, D., Jones, D., Palmer, P., Logan, J., Streets, D., Sachse, G., Gille, J., Hoffman, R. and Nehrke, T.: Comparative inverse analysis of satellite (MOPITT) and aircraft (TRACE-P) observations to estimate Asian sources of carbon monoxide, *J. Geophys. Res.-Atmos.*, 109(D23), D23306, doi:10.1029/2004JD005185, 2004.

Hsu, Y.-K., VanCuren, T., Park, S., Jakober, C., Herner, J., FitzGibbon, M., Blake, D.R., and Parrish, D.D., Methane emission inventory verification in southern California, *Atmos. Environ.*, 44, 1-7, 2010.

Jeong, S., Zhao, C., Andrews, A.E., Bianco, L., Wilczak, J.M., and Fischer, M.L., Seasonal variation of CH<sub>4</sub> emissions from central California, *J. Geophys. Res.*, 117, D11306, doi:10.1029/2011JD016896, 2012.

Kaplan, J. O.: Wetlands at the Last Glacial Maximum: Distribution and methane emissions, *Geophys. Res. Lett.*, 29(6), 1079, doi:10.1029/2001GL013366, 2002.

Kort, E.A., Wofsy, S.C., Daube, B.C., Diao, M., Elkins, J.W., Gao, R.S., Hintsa, E.J., Hurst, D.F., Jimenez, R., Moore, F.L., Spackman, J.R., Zondlo, M.A., Atmospheric Observations of Arctic Ocean methane emissions up to 82° north, *Nature Geosciences*, 5, doi:10.1038/NGEO1452, 2012.

McMillan, A. M. S., Goulden, M. L., and Tyler S.C., Stoichiometry of CH<sub>4</sub> and CO<sub>2</sub> flux in a California rice paddy, *J. Geophys. Res.*, 112, G01008, doi:10.1029/2006JG000198, 2007.

Mu, M., J.T. Randerson, G.R. van der Werf, L. Giglio, P. Kasibhatla, D. Morton, G.J.

Collatz, R.S. DeFries, E.J. Hyer, E.M. Prins, D.W.T. Griffith, D. Wunch, G.C. Toon, V. Sherlock, and P.O. Wennberg. Daily and 3-hourly variability in global fire emissions and consequences for atmospheric model predictions of carbon monoxide. *Journal of Geophysical Research-Atmospheres*. 116: D24303. doi:10.1029/2011JD016245, 2010.

Park, R. J., Jacob, D.J., Field, B. D., Yantosca, R.M., and Chin, M., Natural and transboundary pollution influences on sulfate-nitrate-ammonium aerosols in the United States: implications for policy, *J. Geophys. Res.*, 109, D15204, 10.1029/2003JD004473, 2004.

Parker, R., Boesch, H., Cogan, A., Fraser, A., Feng, L., Palmer, P. I., Messerschmidt, J., Deutscher, N., Griffith, D. W., Notholt, J., Wennberg, P. O., and Wunch, D.: Methane observations from the Greenhouse Gases Observing SATellite: Comparison to ground-based TCCON data and model calculations, *Geophys. Res. Lett.*, 38, L15807, doi:10.1029/2011GL047871, 2011.

Peischl, J., Ryerson, T.B., Holloway, J.S., Trainer, M., Andrews, A.E., Atlas, E.L., Blake, D.R., Daube, B.C., Dlugokencky, E.J., Fischer, M.L., Goldstein, A.H., Guha, A., Karl, T., Kofler, J., Kosciuch, E., Misztal, P.K., Perring, A.E., Pollack, I.B., Santoni, G.W., Schwarz, J.P., Spackman, J.R., Wofsy, S.C., and Parrish, D.D., Airborne observations of methane emissions from rice cultivation in the Sacramento Valley of California, *J. Geophys. Res.*, 117, D00V25, doi: 10.1029/2012JD017994, 2012.

Peischl, J., Ryerson, T.B., Brioude, J., Aikin, K.C., Andrews, A.E., Atlas, E.L., Blake, D.R., Daube, B.C., de Gouw, J.A., Dlugokencky, E.J., Frost, G.J., Gentner, D.R., Gilman, J.B., Goldstein, A.H., Harley, R.A., Holloway, J.S., Kofler, J., Kuster, W.C., Lang, P.M., Novelli, P.C., Santoni, G.W., Trainer, M., Wofsy, S.C., and Parrish, D.D., Quantifying sources of methane using light alkanes in the Los Angeles basin, California, *J. Geophys. Res. Atmos.*, 118, 4974-4990, doi:10.1002/jrgd.50413.

Rodgers, C.D.: *Inverse Methods for Atmospheric Sounding*, World Scientific Publishing Co. Pte. Ltd, Tokyo 2000.

Santoni, G.W., Xiang, B., Kort, E.A., Daubel, B.C., Andrews, A.E., Sweeney, C., Wecht, K.J., Peischl, J., Ryerson, T.B., Angevine, W.M., Trainer, M., Nehr Korn, T., Eluszkiewicz, J., Jeong, S., Fischer, M.L., Ferrare, R.A., and Wofsy, S.C., California's methane budget derived from CalNex P-3 Aircraft Observations and a Lagrangian transport model, *J. Geophys. Res.*, submitted.

Schepers, D., et al. (2012), Methane retrievals from Greenhouse Gases Observing Satellite (GOSAT) shortwave infrared measurements: Performance comparison of proxy and physics retrieval algorithms, *J. Geophys. Res.*, 117, D10307, doi:10.1029/2012JD017549.

Singh, H.B., Brune, W.H., Crawford J.H., and Jacob, D.J., Overview of the summer 2004 Intercontinental Chemical Transport Experiment-North America (INTEX-A), *J. Geophys. Res.*, 111, D24S01, doi:10.1029/2006JD007905, 2006.

United States Environmental Protection Agency (EPA), Inventory of U.S. Greenhouse Gas Emissions and Sinks: 1990-2011-Annexes, 2013.  
<http://www.epa.gov/climatechange/Downloads/ghgemissions/US-GHG-Inventory-2013-Main-Text.pdf>

van der Werf, G. R., Randerson, J. T., Giglio, L., Collatz, G. J., Mu, M., Kasibhatla, P. S., Morton, D. C., DeFries, R. S., Jin, Y., and van Leeuwen, T. T.: Global fire emissions and the contribution of deforestation, savanna, forest, agricultural, and peat fires (1997–2009), *Atmos. Chem. Phys.*, 10, 11707–11735, doi:10.5194/acp-10-11707-2010, 2010.

Veefkind, J.P., Aben, I., McMullan, K., Forster, H., de Vries, J., Otter, G., Claas, J., Eskes, H.J., de Haan, J.F., Kleipool, Q., van Weele, M., Hasekamp, O., Hoogeveen, R., Landgraf, J., Snel, R., Tol, P., Ingmann, P., Voors, R., Kruizinga, B., Vink, R., Visser, H., and Levelt, P.F., TROPOMI on the ESA Sentinel-5 Precursor: A GMES mission for global observations of the atmospheric composition for climate, air quality and ozone layer applications, *Remote Sensing of Environment* 120, 70-83, 2012.

Wecht, K.J., Jacob, D.J., Wofsy, S.C., Kort, E.A., Worden, J.R., Kulawik, S.S., Henze, D.K., Kopacz, M., and Payne, V.H., Validation of TES methane with HIPPO aircraft observations: implications for inverse modeling of methane sources, *Atmos. Chem. Phys.*, 12, 1823–1832, 2012.

Wecht, K.J., Jacob, D.J., Frankenberg, C., Blake, D.R., and Jiang, Z., Mapping of North American methane emissions with high spatial resolution by inversion of SCIAMACHY satellite data, in prep.

Wennberg, P.O., Mui, W., Wunch, D., Kort, E.A., Blake, D.R., Atlas, E.L., Santoni, G.W., Wofsy, S.C., Diskin, G.S., Jeong, S., and Fischer, M.L., On the sources of methane to the Los Angeles atmosphere, *Environ. Sci. Tech.*, 46, 9282-9289, 2012.

Worden, J.R., Jiang, Z., Jones, D.B.A., Alvarado, M., Bowman, K., Frankenberg, C., Kort, E.A., Kulawik, S.S., Lee, M., Liu, J., Payne, V., Wecht, K., and Worden, H., El Niño, the 2006 Indonesian peat fires, and the distribution of atmospheric methane, *Geophys. Res. Lett.*, 40, 4938-4943, doi:10.1002/grl.50937, 2008.

Worden, J., Kulawik, S., Frankenberg, C., Bowman, K., Payne, V., Cady-Peirara, K., Wecht, K., Lee, J-E., Noone, D., Risi, C.: Profiles of CH<sub>4</sub>, HDO, H<sub>2</sub>O, and N<sub>2</sub>O with improved lower tropospheric vertical resolution from Aura TES radiances, *Atmos. Meas. Tech. Discuss.*, 4, 6679-6721, 2012.

Wunch, D., Wennberg, P. O., Toon, G.C., Keppel-Aleks, G., and Yavin, Y.G., Emissions of greenhouse gases from a North American megacity, *Geophys. Res. Lett.*, 36, L15810, doi:10.1029/2009GL039825, 2009.

Xiong, X., Barnet, C. D., Maddy, E., Sweeney, C., Liu, X., Zhou, L., and Goldberg, M.:

Characterization and Validation of Methane Products from the Atmospheric Infrared Sounder (AIRS), *J. Geo-phys. Res.*, 113, G00A01, doi:10.1029/2007JG000500, 2008.

Xiong, X., Barnet, C., Maddy, E.S., Gambacorta, A., King, T.S., and Wofsy, S.C., Mid-upper tropospheric methane retrieval from IASI and its validation, *Atmos. Meas. Tech.*, 6, 2255-2265, 2013.

Zhao, C., Andrews, A.E., Bianco, L., Eluszkiewicz, J., Hirsch, A., MacDonald, C., Nehrkorn, T., and Fischer, M.L., Atmospheric inverse estimates of methane emissions from Central California, *J. Geophys. Res.*, 114, D16302, doi:10.1029/2008JD011671, 2009.